
Thermal Conduction in Hot Gas of Galaxy Clusters

Sergey Komarov



München 2016

Thermal Conduction in Hot Gas of Galaxy Clusters

Sergey Komarov

Dissertation
an der Fakultät für Physik
der Ludwig-Maximilians-Universität
München

vorgelegt von
Sergey Komarov
aus Khabarovsk, Russland

München, den 9. September 2016

Erstgutachter: Prof. Dr. Rashid Sunyaev

Zweitgutachter: PD Dr. Klaus Dolag

Tag der mündlichen Prüfung: 31. Mai 2016

Contents

Zusammenfassung	xi
Summary	xiv
1 Introduction	1
1.1 Galaxy clusters in a cosmological context	1
1.2 Physics of the intracluster medium	2
1.2.1 Multi-wavelength perspective	2
1.2.2 Turbulence	4
1.2.3 Magnetic fields	6
1.3 Thermal conduction in the intracluster medium	21
1.3.1 Spitzer thermal conductivity	21
1.3.2 Braginskii thermal conductivity	23
1.3.3 Conduction in tangled magnetic fields	24
1.4 Structure of the thesis	26
2 Suppression of local heat flux in the ICM	31
2.1 Introduction	32
2.2 Qualitative discussion	33
2.2.1 Illustrative example: conduction between converging layers of magnetised plasma	33
2.2.2 Astrophysical example: model of a cold front	35
2.2.3 Local correlation between the magnetic-field strength and the heat flux	35
2.2.4 Numerical example: a random 2D velocity field	37
2.3 Heat conduction in a stochastic velocity field	38
2.3.1 Relaxation of temperature fluctuations	38
2.3.2 Kazantsev-Kraichnan model	38
2.3.3 Relation between magnetic-field amplification and suppression of conduction for the white-in-time velocity field	41
2.3.4 Finite-time-correlated velocity field	42
2.3.5 Statistics of the heat flux	44
2.4 Limitations of our theory and a numerical test	47

2.4.1	Spatial scales	47
2.4.2	Incompressibility	48
2.4.3	Stratification	48
2.4.4	Thermal conduction	49
2.4.5	Dynamics of the magnetic field	49
2.4.6	Local versus global conduction	50
2.4.7	Comparison with global cluster simulations	50
2.5	Conclusions	54
2.6	Appendix: statistical calculation of the joint PDF of μ , G and B	55
3	Suppression of thermal conduction in a mirror-unstable plasma	61
3.1	Introduction	61
3.2	A model for parallel electron diffusion in a static magnetic field	64
3.3	Electron diffusion in a magnetic mirror field	66
3.3.1	Properties of the mirror field	66
3.3.2	Electron diffusivity in the limit $\lambda/l_B \gg 1$	68
3.3.3	Electron thermal conductivity in the limit $\lambda/l_B \gg 1$	74
3.4	Electron transport in MHD turbulence	76
3.4.1	Electron transport in a system of stochastic magnetic mirrors	76
3.4.2	Electron transport in a saturated magnetic field produced by MHD dynamo.	77
3.5	Discussion	80
3.6	Appendix: transport of a passive scalar	82
4	Polarization of thermal bremsstrahlung due to electron anisotropy	89
4.1	Introduction	90
4.2	Theoretical framework	91
4.2.1	Generation of pressure anisotropies in a weakly collisional plasma	91
4.2.2	Polarization of bremsstrahlung by electron anisotropy	93
4.3	Application to cold fronts and shocks in the ICM	98
4.3.1	Qualitative estimates	98
4.3.2	Analytical model of magnetic-field-line draping	99
4.3.3	MHD simulations of cold fronts	102
4.4	Discussion	108
4.5	Conclusions	109
4.6	Appendix A: ion anisotropy	110
4.7	Appendix B: differential cross sections for relativistic bremsstrahlung	110
5	Conclusions	117
	Acknowledgements	119

List of Figures

1.1	The Coma cluster in different wavelengths	3
1.2	X-ray image of the Perseus cluster	5
1.3	RM map of Hydra A	9
1.4	Fluctuation dynamo	11
1.5	Mechanism of the firehose instability	15
1.6	Mechanism of the mirror instability	17
1.7	Coulomb collisions	22
1.8	Diffusion in a tangled magnetic field	25
2.1	Evolution of the temperature gradients and the magnetic-field lines in the case of a converging incompressible flow	34
2.2	Suppression of the heat flux in a converging flow	34
2.3	Alignment of the field lines perpendicular to the temperature gradient for the velocity field characteristic of a cold front	36
2.4	Alignment of the field lines perpendicular to the temperature gradient for a stochastic velocity field	39
2.5	The mean square heat flux $\langle G^2 \mu^2 \rangle$ for the time-correlated velocity field	43
2.6	Evolution of the joint PDF of μ and G	46
2.7	Evolution of the joint PDF of $G\mu$ and G	46
2.8	Central 500-kpc region of the simulation box of ZuHone et al. (2013)	51
2.9	Evolution of the joint PDF of μ and G in a global MHD cluster simulation-with no thermal conduction and cooling	52
2.10	Comparison of the joint PDF of μ and G in a global MHD cluster simulation without and with thermal conduction and cooling	53
3.1	Spectrum of the fluctuations of magnetic-field strength in the ICM	63
3.2	Spatial structure of the mirror instability	67
3.3	Magnetic mirror fluctuations along a field line	68
3.4	PDFs of the magnetic mirror fluctuations	69
3.5	Suppression factor of the electron diffusivity in the mirror field	70
3.6	Equivalent representation of the mirror fluctuations in the case $\lambda/l_B \gg 1$	72
3.7	The parallel velocity autocorrelation function in the mirror field	73
3.8	Snapshots of a dynamo-generated magnetic-field and velocity magnitudes	78

3.9	Variation of a turbulent-dynamo-produced magnetic field along a field line	79
3.10	3D PDF of a turbulent-dynamo-produced magnetic field	79
3.11	The suppression factor of the electron diffusivity by turbulent-dynamo-produced magnetic fields	80
4.1	The degree of bremsstrahlung polarization from a beam of electrons	94
4.2	Geometry for the problem of the polarization of bremsstrahlung emission from a cloud of electrons	96
4.3	The degree of bremsstrahlung polarization from a cloud of electrons with a bi-Maxwellian distribution	97
4.4	Generation of pressure anisotropy and thermal bremsstrahlung polarization during kinematic draping of magnetic-field lines around a spherical body .	101
4.5	A simulation of a cold front with a homogeneous initial magnetic field . . .	105
4.6	A simulation of a cold front with a random Gaussian initial magnetic field	107
4.7	Ion anisotropy	111

List of Tables

1.1 ICM parameters 7

Zusammenfassung

Galaxienhaufen sind die größten durch Gravitation gebundenen Strukturen im Universum, die aus den seltenen Maxima der primordialen Dichtefluktuationen durch die hierarchische Strukturbildung entstanden sind. Sie bestehen hauptsächlich aus dunkler Materie (80% der Masse), die tiefe Gravitations-Potentialtöpfe erzeugt. Die baryonische Komponente wird von einem heißen ($T \sim 10$ keV), dünnen ($n \sim 10^{-3} \text{ cm}^{-3}$) und Röntgenstrahlung emittierendem Plasma dominiert (15 % der Masse), welches das Gravitationspotential ausfüllt. Dagegen machen Sterne nur einige wenige Prozent der totalen Masse aus. Galaxienhaufen erlauben es, verschiedenste physikalische Theorien in einer extrem großen Bandbreite an astrophysikalischen Skalen zu testen. Auf großen Skalen lassen Galaxienhaufen kosmologische Messungen zu und können benutzt werden, kosmologische Parameter einzugrenzen. Auf sehr kleinen Skalen, die mehr als zehn Größenordnungen kleiner sind als die Haufen selbst, finden komplexe Prozesse des Plasmas statt. Diese können trotz des Skalenunterschieds großräumige Eigenschaften der Haufen beeinflussen, wie zum Beispiel die effektive Wärmeleitfähigkeit und Viskosität. Der Nutzen, die Transportprozesse im Intracluster-Medium (ICM) zu studieren, ist zweifältig. Auf der einen Seite kann dies helfen, einige rätselhafte beobachtete Merkmale von Galaxienhaufen zu erklären. Diese sind die Bildung von globalen Profilen der Gas-Temperatur, die Stabilität von kalten Kernen, extrem schmale Kaltfronten und Substrukturen, die in Untersuchungen der Röntgeneigenschaften und des Sunyaev-Zel'dovich-Effekts gefunden werden. Auf der anderen Seite kann der Vergleich zwischen Beobachtungen und theoretischen Resultaten Einsicht in die komplexe Physik der Plasmakinetik geben.

Es ist allgemein akzeptiert, dass das Plasma des ICM magnetisiert ist, was durch Radio-Beobachtungen (insbesondere durch Messungen der Faraday-Rotation und Synchrotron-Strahlung) und theoretische Beweise bestätigt wurde. Der Gyrationradius geladener Teilchen um die Feldlinien des ICM, der Larmor-Radius, ist äußerst klein verglichen mit ihrer durchschnittlichen freien Weglänge gegeben durch die Coulomb - Wechselwirkung. Dies führt zu einer Anisotropie der Wärmeleitung und Viskosität, da die Plasmateilchen sich hauptsächlich entlang von Magnetfeldlinien bewegen. Darüber hinaus ist das ICM wahrscheinlich turbulent und zufällige Bewegung führen zu einer Verwirrung des Magnetfelds. Die volle Problematik der Wärmeleitung in einem turbulenten Plasma mit verworrenem Magnetfeld ist enorm kompliziert. In dieser Doktorarbeit spalten wir das Problem in kleinere Teile auf, um einige davon zu untersuchen.

Der erste Teil dieser Arbeit (Kapitel 2) untersucht einen Korrelationseffekt zwischen

den Temperatur-Gradienten und magnetischen Feldern im Verlauf ihrer Entwicklung in dem turbulenten Geschwindigkeitsfeld des ICM. Dieser Effekt führt eventuell zu einer lokalen Unterdrückung der Wärmeleitung auf Skalen von turbulenten Wirbeln, wird jedoch auf größeren Skalen unwichtig. Er könnte die langlebigen Unterstrukturen der Temperatur erklären, die von *Chandra* im Großteil des ICM beobachtet werden (Markteich et al. 2003). Durch analytische Methoden wird gezeigt, dass zufällige Geschwindigkeitsfelder statistisch dazu neigen, dass sich Temperatur-Gradienten senkrecht zu Magnetfeldlinien ausrichten. Dies unterdrückt den Wärmefluss entlang des Gradienten, obwohl diese verstärkt werden. Dies geschieht, da die Magnetfeldlinien im Gas eingefroren werden und sich die Temperatur in der Anwesenheit von Unterschallbewegungen ($M \sim 0.1$) wie ein passiver Skalar verhält (bei Vernachlässigung der Schichtung und Wärmeleitung selbst). Obwohl die Annahmen in dem analytischen Modell sehr einschränkend sind, zeigt ein Vergleich mit MHD Simulationen, in denen Gasbewegungen in Galaxienhaufen mit anisotroper Wärmeleitung (ZuHone et al., 2013) simuliert werden, dasselbe qualitative Verhalten von Temperatur-Gradienten und Magnetfeld.

Der zweite Teil der Arbeit (Kapitel 3) untersucht den Unterdrückungseffekt paralleler Wärmeleitung durch magnetische Spiegel. Diese entstehen auf großen und mikroskopischen Skalen. Auf den mikroskopischen Skalen des Larmor-Radius entstehen sie durch Veränderungen der Feldstärke im Bereich $\delta B/B \sim 1$, der für magnetische Spiegelungen relevant ist. Die Spiegel-Instabilität im ICM resultiert aus der Druck-Anisotropie, die wiederum durch turbulente Bewegungen mittels Erhaltung adiabatischer Invarianten hervorgerufen wird. Da die Spiegelschwankungen räumlich nicht aufgelöst werden können, werden die Ergebnisse neuester, numerischer Simulationen von Kunz et al. (2014) verwendet, um die typischen Eigenschaften des Magnetfelds zu bestimmen. Durch die Kombination aus Monte-Carlo-Simulationen und analytischen Methoden wird die effektive Wärmeleitfähigkeit in solch einem Magnetfeld berechnet. Der Unterdrückungsfaktor beträgt $S_\kappa \sim 1/5$, unabhängig von großräumigen Eigenschaften des ICM. Ausserdem wird die Wärmeleitung in magnetischen Spiegeln, die durch turbulente Bewegungen des Gases verursacht werden, untersucht. Diese Veränderungen der magnetischen Feldstärke resultieren aus dem 'turbulenten Dynamo'. Dennoch zeigen wir, dass sie keine merkliche Unterdrückung der Wärmeleitfähigkeit verursachen, da sie auf Skalen auftreten, die hinreichend kleiner sind als die mittlere freie Weglänge der Elektronen. Magnetische Spiegelungen werden auf diesen Skalen wirkungslos.

Im letzten Teil der Arbeit wird ein mögliches Beobachtungsmerkmal der Anisotropie des Elektronendrucks im ICM untersucht, das sich durch Polarisation der thermischen Bremsstrahlung zeigt (Kapitel 4). Die Anisotropie wird durch Streckung der Magnetfeldlinien erzeugt, die wiederum durch Wärme- und Plasmaflüsse mittels Erhaltung adiabatischer Invarianten angetrieben wird. Die Stärke der Anisotropie wird durch die Kollisionsrate der Elektronen gesteuert. Berücksichtigt wird eine grossräumige kohärente Strömung, die eine regelmäßige Struktur im Magnetfeld erzeugt, wodurch die Polarisation sich nicht durch Integration entlang von Sichtlinien aufhebt. Der Grad der Polarisation in kalten Fronten und entlang von Schocks im ICM wird auf $\sim 0.1\%$ geschätzt, mit Energien $\gtrsim kT$. Dieser Wert ist zu niedrig für die zukünftige Generation von Röntgenpolarimetern, jedoch könnte

er wichtig für die Prozesse auf extrem kleinen Skalen sein, die nicht räumlich aufgelöst werden können. Zum Beispiel steht der Polarisationsgrad in direktem Bezug zur Kollisionsrate der Elektronen, die durch kinetische Instabilitäten des Plasmas auf sehr kleinen Skalen erhöht werden kann. Die Ergebnisse deuten ausserdem darauf hin, dass dieser Effekt nicht ausschließt, dass Galaxienhaufen als (unpolarisierte) Eichungsquellen für zukünftige Röntgenpolarimeter (z.B. XIPE, IXPE, PRAXyS) dienen können.

Summary

Clusters of galaxies are the largest gravitationally bound structures in the Universe formed from the rare high peaks in the primordial density perturbations by hierarchical clustering. They mostly consist of dark matter ($\sim 80\%$ of the mass) that forms deep gravitational potential wells. The baryonic component of clusters is dominated ($\sim 15\%$ of the mass) by an X-ray emitting hot ($T \sim 10$ keV) tenuous ($n \sim 10^{-3}$ cm $^{-3}$) plasma that fills the cluster potential, while stars comprise only a few percent of the total mass. Clusters of galaxies make possible to test various physical theories in an extremely broad range of astrophysical scales. On large scales, clusters act as cosmological probes and provide independent constraints on the cosmological parameters. On microscales, more than ten orders of magnitude smaller than the size of clusters, intricate plasma processes occur that, despite their scale, are able to affect large-scale properties of clusters, e.g., the effective thermal conductivity and viscosity. The benefit of studying transport processes in the intracluster medium (ICM) is twofold. On the one hand, this may help to understand some of the puzzling observed features of galaxy clusters: formation of global gas temperature profiles, stability of cool cores, extremely narrow cold fronts, and substructure found in X-ray and Sunyaev-Zel'dovich effect data. On the other hand, confronting observations with theoretical results can give an insight into the complicated physics of plasma kinetics.

It is broadly accepted that the ICM plasma is magnetized, which has been confirmed both by radio observations (Faraday rotation and synchrotron emission measurements) and theoretical arguments. The radius of gyration of the charged particles around the intracluster magnetic-field lines, the Larmor radius, is extremely small compared to their Coulomb collisional mean free path. This renders thermal conduction and viscosity anisotropic, as the plasma particles mostly travel along the magnetic-field lines. Moreover, the ICM is likely to be turbulent, and random motions of the gas tangle the magnetic field. The full problem of thermal conduction in a turbulent plasma with a tangled magnetic field is enormously complicated. In this work, we break it down into smaller parts to study some of them separately.

In the first part of the work, we study the correlation between the temperature gradients and magnetic fields over the course of their evolution in the turbulent velocity field of the ICM (Chapter 2). This effect may lead to local suppression of thermal conduction at the scale of turbulent eddies, while becomes unimportant at larger scales. It can potentially explain the apparently long-lived temperature substructures seen by the *Chandra* X-ray observatory in the bulk of the ICM (Markevitch et al., 2003). By applying ana-

lytical methods, we demonstrate that a random velocity field statistically tends to orient the temperature gradients perpendicular to the magnetic-field lines, suppressing the heat flux in the direction of the gradient, even though the gradients are amplified. It happens because the magnetic-field lines are frozen into the gas, and temperature in the presence of essentially subsonic ($M \sim 0.1$) motions behaves as a passive scalar (ignoring stratification and thermal conduction itself). Although the assumptions made in the analytical model appear quite restrictive, comparison with MHD simulations of gas sloshing in galaxy clusters with anisotropic conduction (ZuHone et al., 2013) testify to the same qualitative behavior of the temperature gradients and magnetic field.

In the second part, we study the effect of suppression of parallel thermal conduction by magnetic mirrors (Chapter 3). Magnetic mirrors arise both at large and microscopic scales. At the microscale of the ion Larmor radius, these are produced by the mirror instability that generates variations of the field strength of order unity $\delta B/B \sim 1$, relevant for magnetic mirroring. The mirror instability in the ICM is a result of pressure anisotropy driven by turbulent motions via the conservation of adiabatic invariants. Because the mirror fluctuations are impossible to resolve spatially in observations, we use the results of the recent numerical simulations by Kunz et al. (2014) to obtain the typical magnetic-field properties. We calculate the effective thermal conductivity in such a field using Monte Carlo simulations and analytical methods combined. The resulting suppression factor is $S_\kappa \sim 1/5$, and appears to be independent of large-scale properties of the ICM. We also study thermal conduction in magnetic mirrors produced by turbulent motions of the gas. These variations of the magnetic-field strength are an outcome of the turbulent dynamo. However, we argue that they do not cause a sizable suppression of conductivity, because they occur at scales sufficiently larger than the electron mean free path, and magnetic mirroring in this regime becomes inefficient.

In the last part of the work, we investigate a possible observational imprint of electron pressure anisotropy in the ICM in the form of polarization of thermal bremsstrahlung emission (Chapter 4). The anisotropy is driven by stretching of the magnetic-field lines by a plasma flow via adiabatic invariance and by heat fluxes. The level of the anisotropy is controlled by electron collisionality. We consider the case of a large scale coherent flow that produces an ordered magnetic-field configuration, and, therefore, for which the polarization does not cancel out after integrating along the line of sight. Our estimate of the degree of polarization in cold fronts and along shocks featured in the ICM is $\sim 0.1\%$ at energies $\gtrsim kT$. While this value is too low for the forthcoming generation of X-ray polarimeters, it is potentially an important proxy for the processes taking place at extremely small scales, which are impossible to resolve spatially. For example, the polarization degree is directly related to electron collisionality, which can be effectively increased by microscale kinetic plasma instabilities. Our result also implies that this effect does not preclude the use of clusters as (unpolarized) calibration sources for the future X-ray polarimeters (e.g., XIPE, IXPE, PRAXyS) at this level of accuracy.

Chapter 1

Introduction

1.1 Galaxy clusters in a cosmological context

Galaxy clusters are the most massive (with a mass of $\sim 10^{15} M_{\odot}$) gravitationally bound objects in the present Universe. Similarly to all objects in the Universe, they were formed from tiny perturbations of density produced during the Universe's inflation (e.g., Peebles, 1993; Peacock, 1999; Mukhanov, 2005). The formation time of virialized objects depends only on the initial perturbation amplitude, because linear perturbations grow at the same rate on all scales. The primordial perturbations have a power spectrum close (with a spectral index slightly smaller than 1) to the scale-invariant Harrison-Zeldovich spectrum, for which larger (more massive) objects have a lower amplitude and, therefore, are formed at later times. Clusters are the largest virialized structures that have formed to date, and they remain so because of the accelerated expansion of the Universe with dark energy that slows down and eventually reverses the linear perturbation growth rate. A strong dependence of cluster properties on the cosmological model makes them a unique tool in imposing stringent constraints on the dark energy characteristics (e.g., Vikhlinin et al., 2009). The amplitude of the cluster mass function is exponentially sensitive to the linear amplitude of matter density perturbations at a given redshift, which allows precision measurements of their power spectrum and the geometry of the Universe.

The cluster mass is dominated by dark matter ($\sim 80\%$). The deep gravitational well of a cluster heats up the infalling gas to very high temperatures of order $10^7 - 10^8$ K, which makes galaxy clusters powerful sources of X-ray emission. The hot gas comprises $\sim 15\%$ of the cluster mass, and the processes involving the intracluster gas primarily determine the evolutionary physics and observational appearance of clusters. Cluster galaxies are embedded into the intracluster medium (ICM), but represent only a few percent of the baryonic mass, and play a lesser role in the cluster dynamics.

Even though galaxy clusters are in virial equilibrium, they are far from being static. Various violent phenomena, such as cluster mergers, gas sloshing, and active galactic nuclei (AGN) activity, are all characteristic of the intracluster gas. Among the physical processes that define the state of the ICM are turbulence, shocks, thermal conduction, radiative cool-

ing, particle acceleration and plasma instabilities, some of which can be observed directly or indirectly.

1.2 Physics of the intracluster medium

1.2.1 Multi-wavelength perspective

Galaxy clusters are observed across a wide range of wavelengths. First, because the ICM is a hot tenuous plasma, it emits X-rays, which was first discovered in rocket experiments in the 60s (Byram et al., 1966; Bradt et al., 1967) and later in the 70s by the *UHURU* X-ray observatory (Kellogg et al., 1972; Forman et al., 1972). The main components of the X-ray emission are thermal bremsstrahlung, recombination continuum, and emission lines excited by electron collisions. The upper left panel of Fig. 1.1 shows an X-ray map of the Coma cluster. X-ray observations allow one to measure the distribution of density and temperature in the ICM, both global radial profiles and local fluctuations at current level of precision. This is a powerful instrument to probe the gravitational potential and the mass distribution within a cluster. X-ray astronomy also reveals the violent nature of the ICM exhibited by AGN activity, bubbles of relativistic plasma, cold fronts, shocks and turbulence. Studying the fluctuations of X-ray surface brightness makes possible putting constraints on the amount of turbulence and even estimate the velocity power spectrum (Churazov et al., 2012; Zhuravleva et al., 2014). Future X-ray observatories, such as *Hitomi* (*ASTRO-H*) and *Athena*, will possess a much higher energy resolution, which will allow more precise measurements of cluster turbulence by estimating the shift and broadening of X-ray lines.

The Sunyaev-Zeldovich effect leads to a decrement in the intensity of the Cosmic Microwave Background Radiation in the direction of galaxy clusters (Sunyaev & Zeldovich, 1972). Because of that, clusters are seen as cold spots in the microwave band below 218 GHz. An image of the Sunyaev-Zeldovich decrement (with the opposite sign) in the Coma cluster is shown in the bottom right panel of Fig. 1.1. The observed decrement does not depend on redshift, and, in combination with thermal X-ray emission measurements, provides an independent method of estimating the Hubble constant (Gunn, 1978; Silk & White, 1978; Birkinshaw, 1979; Cavaliere et al., 1979).

Galaxy clusters are also seen in the radio band (e.g., Govoni & Feretti, 2004). The first diffuse radio source detected in a cluster of galaxies is the giant halo in the Coma cluster (Large et al., 1959; Willson, 1970). In contrast with obvious radio sources associated with galaxies, diffuse extended radio sources associated with the ICM are much more puzzling. These are a clear evidence that the thermal ICM plasma coexists with non-thermal components, which are produced by synchrotron emission from a population of relativistic electrons gyrating in large-scale magnetic fields. The existence of magnetic fields in clusters has also been supported by Faraday rotation measurements (pioneered by the Cygnus A observations by Dreher et al. 1987; see also, e.g., Taylor & Perley 1993; Feretti et al. 1999; Govoni et al. 2001). The energy density of the relativistic plasma is only $\lesssim 1\%$

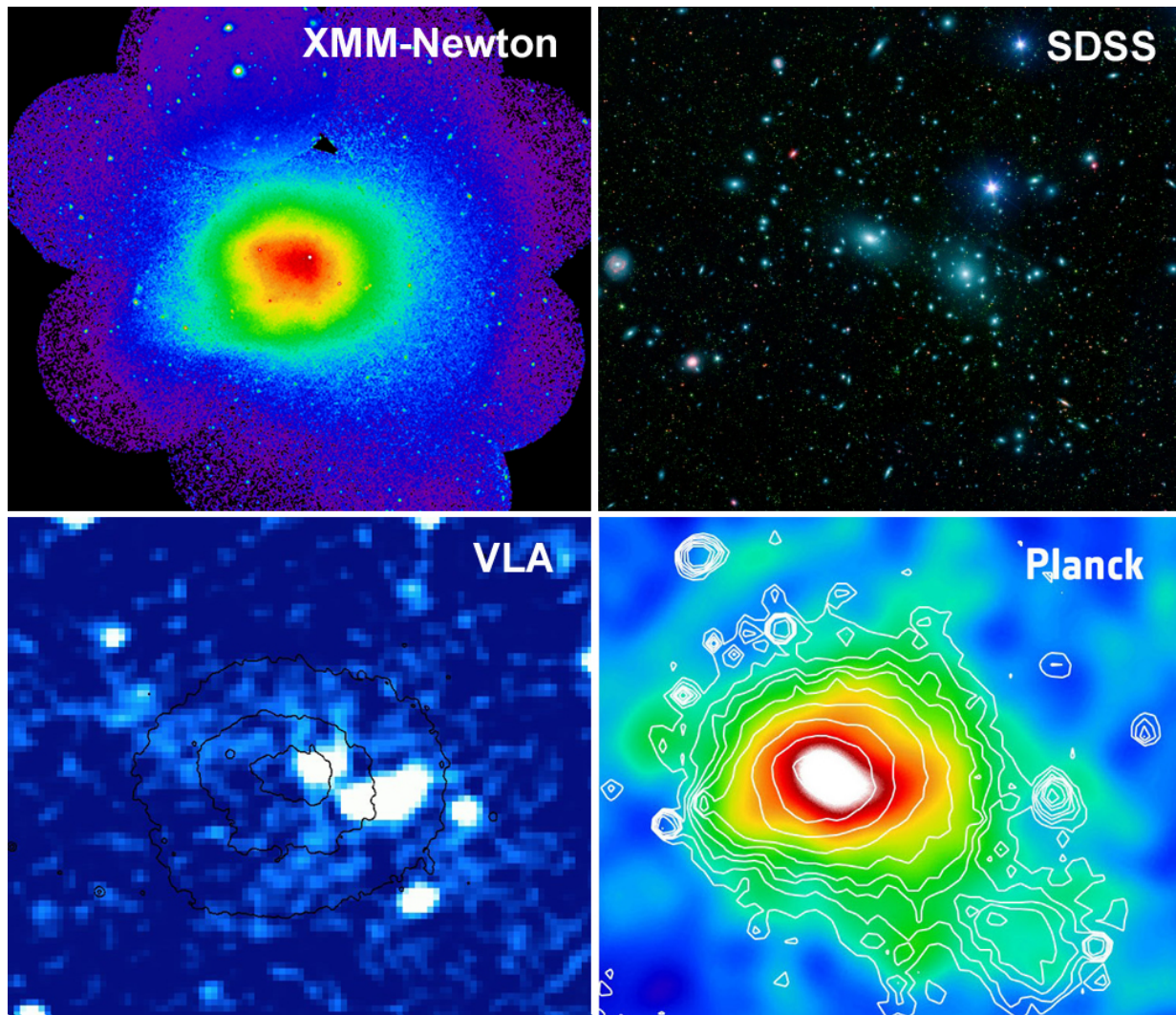


Figure 1.1: The Coma cluster in different wavelengths as observed by *XMM-Newton* in the X-ray (*upper left*), *SDSS* in optical (*upper right*), *VLA* in radio (*bottom left*), and *Planck* in microwave bands (*bottom right*). Credit: NASA/JPL-Caltech/GSFC/SDSS, ESA/HFI and LFI consortia.

relative to the ICM thermal energy density (Prokhorov & Churazov, 2014; Ackermann et al., 2014), but the relativistic particles can, nevertheless, play an important role in the evolution of the large-scale structure in the Universe, provide additional pressure, and undergo acceleration processes. Magnetic fields cause even more profound changes in the ICM physics through the modification of particle transport and even the gas dynamics. The mechanism of re-acceleration of the synchrotron-emitting particles in diffuse extended radio sources still remains an open question, with shocks and turbulence among the probable candidates (e.g., Ensslin et al., 1998; Brunetti & Lazarian, 2007). The diffuse radio emission from the Coma cluster is shown in the bottom left panel of Fig. 1.1.

1.2.2 Turbulence

At large scales, the ICM is disturbed, for instance, by infalling galaxies and cluster mergers. It is natural to expect that the kinetic energy of these events cascades down to small dissipative scales. In cluster cores, turbulence is excited by the rising of bubbles of relativistic plasma during AGN activity. A striking example of the turmoil produced by an AGN is an X-ray image of the core of the Perseus cluster (Fig. 1.2). The inflated bubbles of relativistic plasma (e.g., Boehringer et al., 1993; Churazov et al., 2000; Fabian et al., 2000), surrounding gravity waves and weak shocks are clearly seen as ripples in the X-ray brightness. The internal waves generated by the bubbles are likely to be partly transformed into gas turbulence.

One way to measure cluster turbulence is by analyzing X-ray surface brightness fluctuations. Apart from the velocity-field perturbations, turbulent motions also lead to small density and pressure fluctuations that can be measured by X-ray telescopes. This method was first attempted by Schuecker et al. (2004) to estimate the pressure fluctuations in the Coma cluster from *XMM-Newton* observations. Later, a similar approach, but using high-resolution *Chandra* data, was applied by Churazov et al. (2012) to estimate the relative density fluctuations in the Coma cluster. They found 5–10% fluctuations generated at large scales by the perturbations of the gravitational potential by massive cD galaxies and infalling cold gas, and, likely, turbulence at smaller scales. Recently, the same technique was also applied to the Perseus cluster by Zhuravleva et al. (2015). They reported density fluctuations at a $\sim 10\%$ level and gas velocities $\sim 100 \text{ km s}^{-1}$ with a power spectrum in broad agreement with Kolmogorov turbulence.

The most direct way to measure turbulence in clusters is to measure the broadening of X-ray spectral lines due to the Doppler shifts produced by the motion of the line-emitting ions. The broadening is caused both by the thermal motion and turbulence. For sufficiently heavy ions (iron being the most relevant one), the turbulent broadening becomes of the order of the thermal broadening or larger, and can be detected, provided that the detector has sufficient energy resolution.

Measurements of line broadening have been a difficult task due to insufficient energy resolution of the currently active X-ray observatories. The situation is expected to change drastically with the recent launch of *Hitomi (ASTRO-H)* carrying an X-ray microcalorimeter on board. The calorimeter will provide about 6-eV spectral resolution that opens a

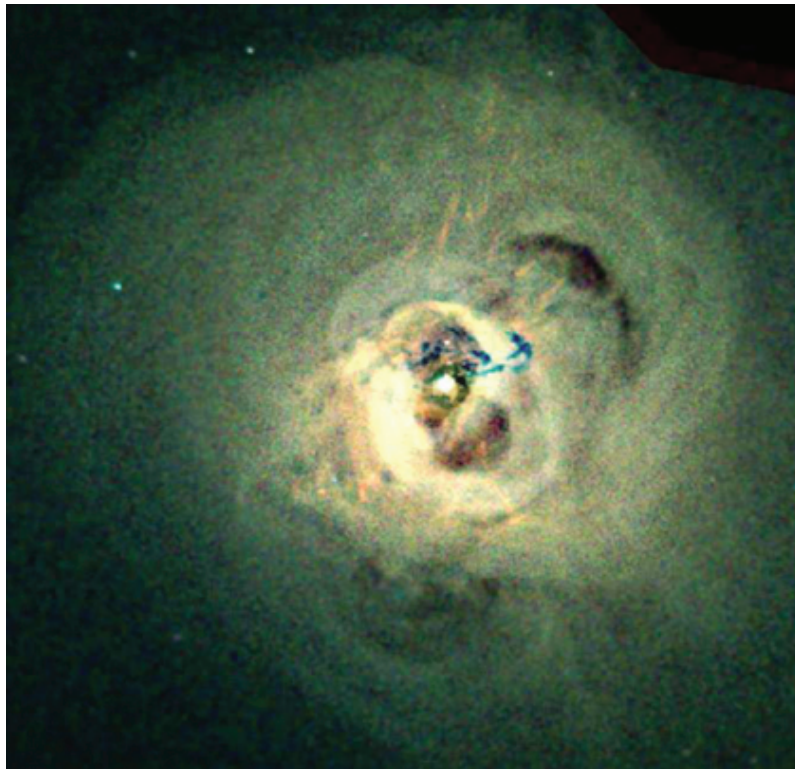


Figure 1.2: *Chandra* X-ray image of the central 100-kpc region of the Perseus cluster (Fabian et al., 2011).

possibility to measure turbulent broadening down to 50–100 km s⁻¹.

Another method of measuring cluster turbulence is based on the resonant scattering of line-emitted photons (Gilfanov et al., 1987). Despite the ICM plasma is optically thin in continuum, a few of the strongest resonance lines have an optical depth of order unity. Photons emitted in these lines can be scattered several times before they escape the ICM. This causes an apparent dimming of a line in the direction of the cluster center due to the fact that resonant photons are scattered out of the line of sight. The optical depth of the scattered line depends on the ratio of the turbulent to thermal energy densities of the gas (Zhuravleva et al., 2011).

Available observational data, along with numerical simulations of cluster formation (Norman & Bryan, 1999; Sunyaev et al., 2003; Ricker & Sarazin, 2001) and of the buoyant radio bubbles inflated by AGNs (Churazov et al., 2001; Fujita, 2005), appear to converge in an estimate of the rms velocities of turbulent flows $U \sim$ a few 10^2 km s⁻¹ at the outer scales $L \sim 10^2$ kpc. By assuming a Kolmogorov-type cascade below L and estimating viscosity simply as $\mu_{ICM} \sim \lambda_{\text{mfp}} v_{\text{th},i}$, where λ_{mfp} is the particle mean free path, $v_{\text{th},i}$ the ion thermal speed, one gets fairly low Reynolds numbers $\text{Re} \sim LU/\mu_{ICM}$: ~ 100 in cluster cores and only a few in the bulk. To better systemize different cluster properties, some of which will arise later in this chapter, in the range of conditions present in the ICM, I organize them in two sets of fiducial parameters: one characteristic of cluster cool cores, and another characteristic of the bulk of the hot ICM (Table 1.1).

1.2.3 Magnetic fields

Faraday rotation observations

Increasingly detailed radio observations of galaxy clusters made possible a quantitative study of the ICM magnetic fields. Faraday rotation measurements provide the most detailed information about the cluster magnetic fields. A magnetic field in a plasma sets a preferential direction for the gyration of electrons, leading to a difference in the refraction index between left and right circularly polarized radiation. This means that as linearly polarized light propagates through a magnetized plasma, its polarization plane experiences rotation, $\Delta\chi = \text{RM}\lambda^2$, where $\Delta\chi$ is the change in the position angle of polarization, λ is the wavelength of the radiation, and RM is the Faraday rotation measure. The rotation measure is a function of the electron density n_e and the component of the magnetic field along the line of sight B_{\parallel} as follows

$$\text{RM} = 812 \int_0^L n_e B_{\parallel} dl \text{ radians m}^{-2}, \quad (1.1)$$

where the integration is carried out along the line of sight, B_{\parallel} is measured in μG , n_e in cm^{-3} , and l in kpc.

Synchrotron emission from charged particles gyrating in a magnetic field with randomly distributed pitch angles is known to be linearly polarized. If an astrophysical radio source (typically, a central radio galaxy) is embedded into the ICM, it can act as a

Table 1.1: Fiducial ICM parameters (adapted with changes from Schekochihin & Cowley 2006).

Name	Notation	Expression	Cool cores ^a	Hot ICM
temperature	T	observed	3×10^7 K	10^8 K
particle density	n	observed	6×10^{-2} cm ⁻³	10^{-3} cm ⁻³
ion thermal speed	$v_{\text{th},i}$	$(2T/m_i)^{1/2}$	700 km s ⁻¹	1300 km s ⁻¹
ion-ion coll. frequency	ν_{ii}	$1.5nT^{-3/2}$ ^b	5×10^{-13} s ⁻¹	2×10^{-15} s ⁻¹
mean free path	λ_{mfp}	$v_{\text{th},i}/\nu_{ii}$	0.05 kpc	30 kpc
parallel kin. viscosity	μ_{\parallel}	$v_{\text{th},i}\lambda_{\text{mfp}}$	10^{28} cm ² s ⁻¹	10^{31} cm ² s ⁻¹
resistivity	η	$3 \times 10^{13} T^{-3/2}$ ^b	200 cm ² s ⁻¹	30 cm ² s ⁻¹
rms velocity at outer scale	U	inferred	250 km s ⁻¹	300 km s ⁻¹
outer scale	L	inferred	10 kpc	200 kpc
turnover time at outer scale	L/U	inferred	4×10^7 yr	7×10^8 yr
hydrodynamic Reynolds num.	Re	UL/μ_{\parallel}	70	2
magnetic Reynolds num.	Rm	UL/η	4×10^{27}	6×10^{29}
viscous scale	l_{visc}	$L\text{Re}^{-3/4}$	0.4 kpc	100 kpc
resistive scale	l_{res}	$L\text{Rm}^{-1/2}$	5000 km	8000 km
ion Larmor frequency	Ω_i	eB_{rms}/cm_i	0.3 s ⁻¹	0.04 s ⁻¹
ion Larmor radius	ρ_i	$v_{\text{th},i}/\Omega_i$	3000 km	30,000 km
rms magnetic field	B_{rms}	observed	20 μG	2 μG
plasma beta	β	$8\pi nT/B_{\text{rms}}^2$	20	100
magnetic-field corr. length	l_B	observed	2 kpc	10 kpc

^aBased on the Hydra A cluster parameters given in Enßlin & Vogt (2006).^bIn these expressions, n is in cm⁻³, T is in degrees Kelvin.

background source of linearly polarized radiation that “backlights” the gas. The X-ray emitting cluster atmosphere then behaves as a Faraday screen, where most of the rotation measure is produced. While the RM could also be produced by thermal gas mixed with the radio-emitting plasma, this possibility was ruled out by the absence of depolarization and precisely quadratical behavior of the observed position angles with wavelength (it was first demonstrated for Cyg A, Dreher et al. 1987). Employing the simple quadratical dependence, RM maps can be obtained by multiwavelength polarization measurements.

Extensive measurements of Faraday rotation of the synchrotron emission from intracluster radio sources with the Very Large Array (VLA) made possible to estimate the magnetic field and its spatial structure in a large number of clusters (e.g., Carilli & Taylor, 2002; Govoni & Feretti, 2004; Laing et al., 2008; Kuchar & Enßlin, 2011). These data revealed magnetic fields with the rms strength of order $B_{\text{rms}} \sim 1 - 10 \mu\text{G}$, randomly tangled at scales $l_B \sim 1 - 10 \text{ kpc}$. A RM map of the Hydra A cluster is shown in Fig. 1.3 as an example. The evident patchiness of the RM distribution in the map is a direct indicator of the stochastic topology of the magnetic fields. Furthermore, high-resolution RM measurements of the radio lobes in the cool core of Hydra A opened a possibility to estimate the power spectrum of the magnetic fluctuations (Vogt & Enßlin, 2005; Kuchar & Enßlin, 2011). The obtained spectrum is consistent with $k^{-5/3}$ down to the resolution limit $k \approx 10 \text{ kpc}^{-1}$. The presence of a large-scale cut-off at $k \approx 0.5 \text{ kpc}^{-1}$ was found in Vogt & Enßlin (2005), but, nevertheless, not confirmed in Kuchar & Enßlin (2011).

Radio relics

Another source of information about cluster magnetic fields is polarized diffuse synchrotron emission in the form of radio relics. Contrary to radio halos, relics are found on the outskirts of clusters and are strongly polarized ($\sim 20 - 30\%$). They allow one to probe the component of the magnetic field perpendicular to the line of sight in the bulk of the ICM. Relics are assumed to be associated with merger shocks, at which relativistic particles are accelerated. Although in elongated relics, the magnetic field is predominantly oriented parallel to the relic due to the amplification of the tangential component of the field at the shock, in some “roundish” relics, a more complicated field structure is seen (e.g., in Abell 2256, Clarke & Enßlin 2006). This may provide an insight into off-center cluster magnetic fields, while Faraday rotation observations only probe cluster cores.

Magnetohydrodynamic description

The simplest description of the ICM on scales much larger than the collisional mean free path of the particles λ_{mfp} is ideal (no viscosity) hydrodynamic. However, using the fiducial parameters in Table 1.1, it is readily seen that cluster magnetic fields can be dynamically important. The parameter that quantifies the dynamical importance of magnetic fields is the plasma β , the ratio of the thermal to magnetic energy densities. For the bulk of the ICM, $\beta \sim 100$. For subsonic turbulent motions at Mach numbers $M \sim 0.1 - 0.2$, it results in the magnetic-energy density of order the kinetic-energy density of the gas. Therefore, for

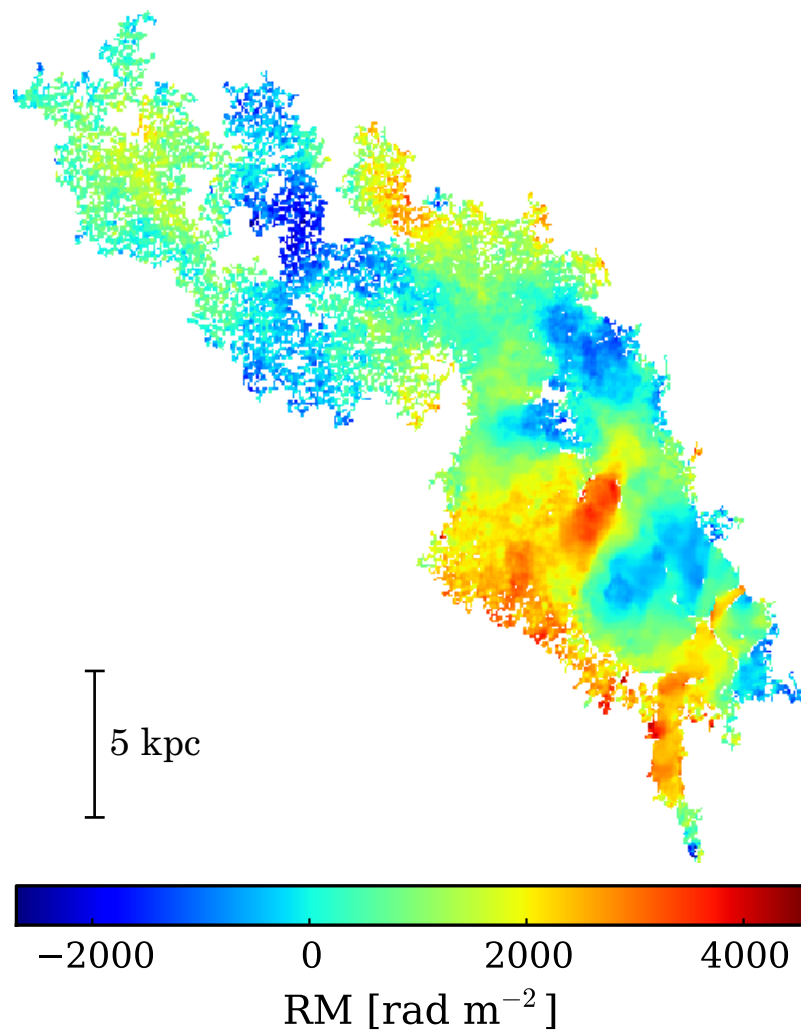


Figure 1.3: Faraday rotation measure map of the northern lobe of the Hydra A cluster (Taylor & Perley, 1993).

proper physical modelling of the ICM, at the very least, the ideal MHD equations should be used instead. MHD dynamics is determined by the following equations:

$$\rho \frac{d\mathbf{v}}{dt} = \frac{1}{4\pi}(\mathbf{B} \cdot \nabla)\mathbf{B} - \nabla \left(p + \frac{B^2}{8\pi} \right), \quad (1.2)$$

$$\frac{\partial \mathbf{B}}{\partial t} = \nabla \times (\mathbf{v} \times \mathbf{B}), \quad (1.3)$$

where $d/dt = \partial/\partial t + \mathbf{v} \cdot \nabla$, ρ is the mass density, \mathbf{v} the gas velocity, and p the thermal pressure. Here I have neglected the resistive term due to the tiny value of the ICM resistivity η (see Table 1.1). I have also omitted the gravitational acceleration \mathbf{g} on the right-hand side of equation (1.2) for brevity. The inclusion of the magnetic pressure $B^2/(8\pi)$ and the magnetic tension $\frac{1}{4\pi}(\mathbf{B} \cdot \nabla)\mathbf{B}$ on the right-hand side of equation (1.2) leads to three additional wave modes: the fast and slow compressional magnetosonic waves and the shear Alfvénic wave. Equation (1.3) is the induction equation, which is linked to an important property of the ideal MHD magnetic field, magnetic flux freezing. Flux freezing means that the magnetic-field lines move strictly with the gas, i.e., they are frozen into the plasma.

One should be mindful that using equations (1.2) and (1.3) in numerical modelling implies setting $\text{Re} \sim \text{Rm}$ (Re is the hydrodynamic, Rm magnetic Reynolds numbers), because the hydrodynamic and magnetic numerical viscosities are of the same order. For the typical cluster properties, however, $\text{Rm} \gg \text{Re}$, and there is an extremely large scale separation between the size of a turbulent eddy and the resistive scale. While, qualitatively, a plasma with $\text{Re} \sim \text{Rm} \gg 1$ may behave similarly to the case $\text{Rm}/\text{Re} \gg 1$, as shown in numerical simulations by Schekochihin et al. (2004), cluster turbulence most likely has fairly low $\text{Re} \sim 1 - 100$, for which it might be difficult to reach magnetic-energy density close to the energy density of the turbulent motions.

Fluctuation dynamo

Cluster magnetic fields must have undergone amplification from the seed fields ($B_{\text{seed}} \sim 10^{-21} - 10^{-9}$ G), present in the Universe before structure formation (Gnedin et al., 2000; Grasso & Rubinstein, 2001), to the currently observed values. The random motions of the ICM may be capable of accomplishing this task over a time shorter than the typical age of clusters (a few Gyr). While other mechanisms of generation of μG -strong magnetic fields in galaxy clusters have been proposed, [for instance, compression of cosmological plasma into a cluster (e.g., Dolag et al., 2005) or injection of AGN-generated fields into the ICM (e.g. Kronberg et al., 2001)], amplification by turbulence is a favorable candidate, intuitively supported by the observational fact that the magnetic-field-energy density is close to the kinetic-energy density of the plasma motions.

The magnetic field is amplified by the ICM turbulence via the mechanism of the fluctuation (or small-scale) dynamo. The fluctuation dynamo is a series of random stretching and folding of the magnetic-field lines that leads on average to an exponential growth of the field (Batchelor, 1950; Zel'dovich et al., 1984; Zeldovich et al., 1990). Let me rewrite

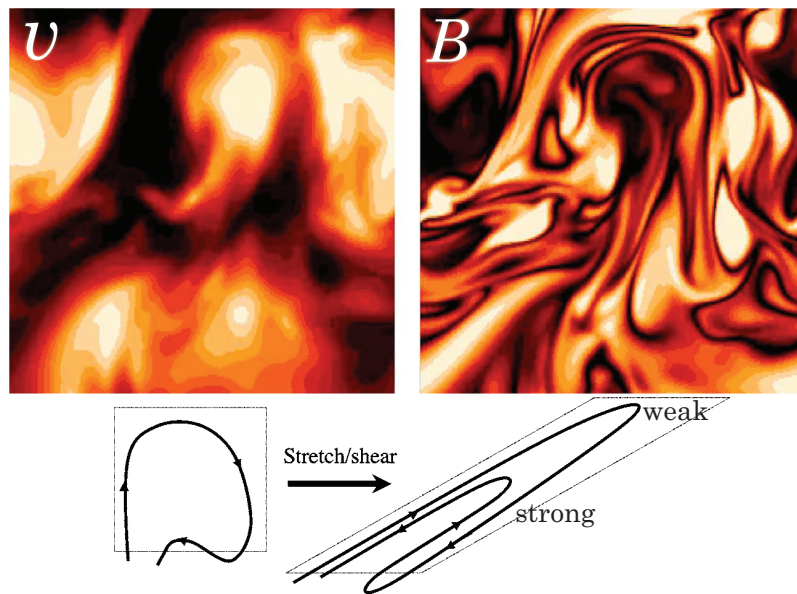


Figure 1.4: *Bottom panel:* the physical mechanism of the fluctuation dynamo; a random linear shear stretches a parcel of plasma in one direction and compresses it in the perpendicular direction, forming a characteristic fold. *Upper panels:* cross sections of the velocity amplitude $|\mathbf{v}|$ (left) and the magnetic-field strength $|\mathbf{B}|$ (right) in the saturated state of a 3D numerical simulation of the turbulent dynamo with $\text{Re}=100$, $\text{Rm}=1000$ (adapted from Schekochihin & Cowley 2006).

the induction equation (1.3) for an incompressible plasma (valid in the case of subsonic turbulence) as

$$\frac{1}{B} \frac{dB}{dt} = \mathbf{bb} : \nabla \mathbf{v} \sim \frac{U}{L} \text{Re}^{1/2}, \quad (1.4)$$

where \mathbf{b} is the unit vector in the direction of the magnetic field, L the injection scale of the cluster turbulence, U the turbulent velocity at the injection scale. The term $\mathbf{bb} : \nabla \mathbf{v}$ is the rate of strain (or the stretching rate or shear) of the random flow at the scale of the viscous eddies. The rate of strain changes stochastically in time, providing a net exponential growth of the magnetic-energy density (I will demonstrate this mathematically in Chapter 2). The physics of the fluctuation dynamo is illustrated in the bottom panel of Fig. 1.4: a random linear shear produces folds of the field lines, along which the field is amplified, while at the field reversals, it becomes weaker. At some point, the magnetic field stops growing exponentially and saturates, when the magnetic-energy density becomes comparable with the kinetic energy of the random motions. However, the folded structure of the field survives even in the saturated state, as shown in numerical simulations by Schekochihin et al. (2004). The structure of the saturated field produced by a turbulent velocity field with $\text{Re} = 100$ and $\text{Rm} = 1000$ is shown in the upper right panel of Fig. 1.4. The parallel scale of the folded flux sheets l_{\parallel} is similar to the scale of the velocity that does the stretching L , while the field reversal scale l_{\perp} in the direction perpendicular to itself is the resistive scale $l_{\text{res}} = L\text{Rm}^{-1/2}$.

From the view of the folded structure of the field, it is clear that the magnetic-field power spectrum should peak at the reversal scale $l_{\perp} \sim l_{\text{res}}$. However, because the ICM resistivity η is extremely small, and the corresponding magnetic Reynolds number $\text{Rm} = UL/\eta \sim 10^{30}$ is extremely large (see Table 1.1), the resistive scale $l_{\text{res}} = L\text{Rm}^{-1/2} \sim 10000$ km is tiny. Therefore, there is a clear contradiction between the observed value of l_B (the correlation length of the magnetic field inferred from the position of the peak in the observed power spectrum) and the prediction of the fluctuation dynamo theory. While $l_B \sim 1 - 10$ kpc is much smaller than the outer scale $L \sim 10 - 100$ kpc, it is certainly far from being as small as the resistive scale.

However, as it turns out, the purely magnetohydrodynamic description of the ICM is not well justified, because the ICM plasma particles collide far less frequently than their rate of gyration in the cluster magnetic field. This feature of the plasma has a profound effect on the ICM physics.

Pressure anisotropies

A key property of the ICM as plasma is that it is only weakly collisional and magnetized, which means that the collisional mean free path of the plasma particles $\lambda_{\text{mfp}} \sim 10$ kpc is much larger than the ion Larmor radius $\rho_i \sim 10^4$ km. This property leads to conservation of adiabatic invariants for charged particles moving in a magnetic field. The first adiabatic invariant is the magnetic moment of a particle $\mu = v_{\perp}^2/(2B)$, where v_{\perp} is the component of the particle's velocity perpendicular to the field line. Summing up the first adiabatic invariants of all particles, one gets $p_{\perp}/B = \text{const}$, where p_{\perp} is the perpendicular pressure.

Thus, the magnetic-field-strength changes are correlated with changes in the perpendicular pressure, giving rise to pressure anisotropy.

When the plasma pressure is anisotropic, the dynamics equation (1.2) should be replaced by the following equation:

$$\rho \frac{d\mathbf{v}}{dt} = -\nabla \left(p_{\perp} + \frac{B^2}{8\pi} \right) + \nabla \cdot \left[\mathbf{b}\mathbf{b} \left(p_{\perp} - p_{\parallel} + \frac{B^2}{4\pi} \right) \right], \quad (1.5)$$

which is valid at time scales $\gg \Omega_i^{-1}$ ($\Omega_i = eB/m_i c$ is the ion Larmor frequency) and spatial scales $\gg \rho_i = v_{\text{th},i}/\Omega_i$. The evolution of p_{\perp} can be calculated by differentiating the condition $p_{\perp}/B = \text{const}$ and allowing rare collisions to isotropize the pressure:

$$\frac{1}{p_{\perp}} \frac{dp_{\perp}}{dt} \sim \frac{1}{B} \frac{dB}{dt} - \nu_{ii} \frac{p_{\perp} - p_{\parallel}}{p_{\perp}}, \quad (1.6)$$

where the second term on the right-hand side represents the relaxation of the pressure anisotropy at the ion collision rate $\nu_{ii} \sim v_{\text{th},i}/\lambda_{\text{mfp}}$ ¹. Using the induction equation (1.4) for an incompressible plasma and assuming a steady state $dp_{\perp}/dt \sim 0$, one gets

$$\Delta \equiv \frac{p_{\perp} - p_{\parallel}}{p_{\perp}} \sim \frac{S}{\nu_{ii}}, \quad (1.7)$$

where I have denoted the velocity rate of strain (shear) $S \equiv \mathbf{b}\mathbf{b} : \nabla \mathbf{v} \sim (U/L)\text{Re}^{1/2}$. Equation (1.7) directly demonstrates how pressure anisotropy Δ emerges during the magnetic-field evolution in a velocity field. The energy conservation law that follows from equations (1.5) and (1.4) is

$$\frac{d}{dt} \left(\frac{\langle v^2 \rangle}{2} + \frac{\langle B^2 \rangle}{8\pi} \right) = -\mu_{\parallel} \langle |\mathbf{b}\mathbf{b} : \nabla \mathbf{v}|^2 \rangle = -\mu_{\parallel} \left\langle \left(\frac{1}{B} \frac{dB}{dt} \right)^2 \right\rangle, \quad (1.8)$$

where $\mu_{\parallel} \sim p_{\perp}/\nu_{ii} \sim v_{\text{th},i}\lambda_{\text{mfp}}$ is the ‘‘parallel’’ Braginskii viscosity (Braginskii, 1965). The role of μ_{\parallel} is to only damp such motions that change the strength of the magnetic field, while motions that do not affect B are allowed at subviscous scales. These motions could be a cascade of transverse Alfvénic perturbations. However, even equation (1.5) is ill-posed when $|p_{\perp} - p_{\parallel}| \gtrsim B^2$ because of the development of microscale kinetic instabilities, whose growth rates happen to peak at the ion Larmor radius scale.

¹In all that follows in this chapter, we only consider ion pressure anisotropies, because electron anisotropies are typically very weak due to the fact that the electron collision frequency ν_e is $(m_i/m_e)^{1/2} \approx 40$ times larger than ν_{ii} [see equation (1.7)].

Microscale instabilities

Firehose instability

Assume first that a parcel of plasma is subjected to a negative linear shear $S \equiv \mathbf{b}\mathbf{b} : \nabla\mathbf{v}$, and the local magnetic-field strength B is decreasing:

$$\frac{1}{B} \frac{dB}{dt} = S < 0. \quad (1.9)$$

Then from equation (1.7), the anisotropy Δ is negative. Let me now introduce a small transverse (Alfvénic) perturbation to the magnetic field \mathbf{B} (see Fig. 1.5). The plasma particles² moving along the bend of the field line with curvature radius R at parallel thermal velocity $v_{\text{th}\parallel}$ exert a centrifugal force $F_R = m_i n v_{\text{th}\parallel}^2 / R$ on the field line. The centrifugal force is directed outward and tends to bend the field line further. It is resisted by the force of the perpendicular pressure $F_{p\perp} = p_{\perp} / R$ and the magnetic stress of the field line $F_B = B^2 / (4\pi R)$. The equilibrium condition is

$$\frac{m_i n v_{\text{th}\parallel}^2}{R} = \frac{p_{\perp}}{R} + \frac{B^2}{4\pi R}. \quad (1.10)$$

Using $p_{\parallel} = n m_i v_{\text{th}\parallel}^2$ and notations $\beta_{\perp} = 8\pi p_{\perp} / B^2$, $\beta_{\parallel} = 8\pi p_{\parallel} / B^2$, one arrives at the condition for the firehose instability:

$$\beta_{\perp} + 2 < \beta_{\parallel}. \quad (1.11)$$

For small anisotropy, $\beta_{\perp} \approx \beta_{\parallel} \approx \beta$, the condition is

$$\Delta < -\frac{2}{\beta}. \quad (1.12)$$

For the typical hot ICM parameters taken from Table 1.1, one can estimate $|\Delta| \sim U / (v_{ii} L) \sim 0.01$, while $\beta \sim 100$. It is clear that the cluster plasma can indeed be firehose unstable in the presence of a random local turbulent shear, despite the anisotropy is small.

The dispersion relation for small Alfvén-wave-polarized perturbations in an anisotropic plasma can be derived by linearizing equation (1.5). It reads

$$\omega = \pm k_{\parallel} \left(p_{\perp} - p_{\parallel} + \frac{B^2}{4\pi} \right)^{1/2}, \quad (1.13)$$

where ω is the circular frequency, k_{\parallel} the parallel wavenumber of the perturbation. When $p_{\perp} - p_{\parallel} + B^2 / (4\pi) < 0$, ω is imaginary, and an instability develops. The growth rate of the instability is $\propto k_{\parallel}$, so the fastest-growing perturbations are at scales far below the

²We assume them to be ions for simplicity. The firehose and mirror instability conditions depend on both ion and electron pressure anisotropies. However, the electron anisotropy is normally much smaller because of the large electron collisionality [see equation (1.7)].

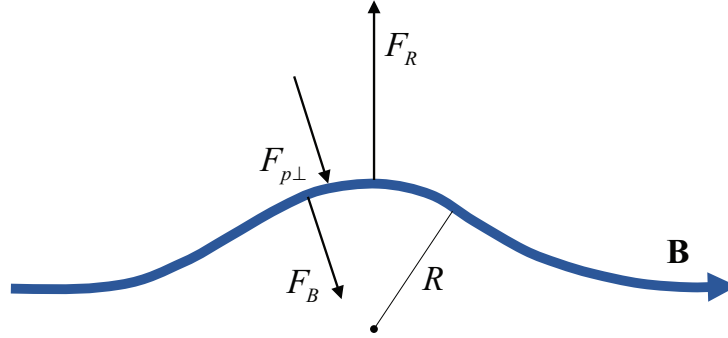


Figure 1.5: Mechanism of the firehose instability.

mean free path. Therefore, the description of the ICM based on equation (1.5) is ill posed whenever the instability condition (1.12) is satisfied, and a kinetic description must be adopted instead. A kinetic treatment of the instability shows that the growth rate peaks at the ion gyroscale, $k_{\parallel}\rho_i \sim 1$.

Thus, large-scale random motions change the magnetic field and drive pressure anisotropy, which, in turn, triggers the firehose instability. The instability is stabilized when the magnetic-field becomes strong enough to compensate for the energy of pressure anisotropy, $B^2/(4\pi) > |p_{\perp} - p_{\parallel}|$, and the firehose fluctuations transform into Alfvén waves, which can cascade all the way down to the ion gyroscale without being affected by collisions.

Mirror instability

In regions where the magnetic-field strength is increasing, and positive anisotropy $p_{\perp} > p_{\parallel}$ is produced, the mirror instability occurs. The mirror instability is purely kinetic, and cannot be derived properly from fluid equations.

Let me first study the motion of a charged particle in a static periodic magnetic field, whose field strength varies between B_{\min} and B_{\max} along a field line as $B = B(\ell)$, where ℓ is the field-line coordinate. The magnetic field does not change the particle’s energy. If the field strength changes are smooth (compared with the Larmor radius), the particle also conserves its magnetic moment (first adiabatic invariant),

$$\mu = \frac{v_{\perp}^2}{2B} \propto \frac{1 - \xi^2}{B} = \text{const}, \quad (1.14)$$

as it moves along the field line. Here $\xi = \cos\theta$, θ is the pitch angle of the particle, so $v_{\parallel} = v\xi$. Then, as the particle travels from location ℓ_0 to ℓ_1 , $(1 - \xi_0^2)/B_0 = (1 - \xi_1^2)/B_1$, where the subscripts correspond to the values at different locations. For ξ_1 , one gets

$$\xi_1^2 = 1 - \frac{B_1}{B_0}(1 - \xi_0^2). \quad (1.15)$$

When the right-hand side of this equation equals zero, the parallel velocity of the particle changes its sign, and the particle is reflected (“mirrored”) from a region of stronger field

$B_1 > B_0$ and becomes trapped between neighboring regions with $B = B_1$. This effect is called magnetic trapping. The condition for a particle to be trapped is

$$\xi_0 < \xi_{\text{crit}} = (1 - B_0/B_{\text{max}})^{1/2}. \quad (1.16)$$

The value of ξ_{crit} determines the so-called loss cone for the particles. Particles that travel in the loss cone with $\xi_0 > \xi_{\text{crit}}$ are “passing”. They propagate freely through the field structure, only changing their parallel velocities in order to conserve the magnetic moment. Particle outside the loss cone ($\xi_0 < \xi_{\text{crit}}$) inevitably become trapped between regions of strong enough field. For both groups of particles, their parallel motion can be described in terms of an effective “mirror” force, which can be obtained from the conservation of magnetic moment expressed as $d\mu/dl = 0$:

$$\dot{\xi} = -\frac{1 - \xi^2}{2B} \frac{dB}{dl}, \quad (1.17)$$

where the dot denotes the Lagrangian time derivative. Equation (1.17) demonstrates explicitly that particles are expelled from regions of large magnetic-field strength. This fact plays a key role in the physics of the mirror instability.

Now, consider a plasma with a bi-Maxwellian distribution function F ,

$$F(\mathbf{v}) = n \left(\frac{m_i}{2\pi T_{\perp}} \right) \left(\frac{m_i}{2\pi T_{\parallel}} \right)^{1/2} \exp \left[- \left(\frac{W_{\perp}}{T_{\perp}} + \frac{W_{\parallel}}{T_{\parallel}} \right) \right], \quad (1.18)$$

where $W_{\perp} = m_i v_{\perp}^2/2$, $W_{\parallel} = m_i v_{\parallel}^2/2$ are the perpendicular and parallel particle’s energy, and the corresponding temperatures are defined as

$$T_{\perp} = \frac{1}{n} \int d^3\mathbf{v} W_{\perp} F, \quad (1.19)$$

$$T_{\parallel} = \frac{1}{n} \int d^3\mathbf{v} 2W_{\parallel} F, \quad (1.20)$$

where $d^3\mathbf{v} = 2\pi v_{\perp} dv_{\perp} dv_{\parallel}$. Consider also a small slowly changing (compared to the ion Larmor frequency) perturbation of magnetic-field strength along a field line,

$$\delta B \propto \exp(ik_{\parallel}l + \gamma t), \quad (1.21)$$

where $\gamma \ll \Omega_i$. Let me first describe the behavior of particles with $v_{\parallel} > \gamma/k_{\parallel}$. These particles traverse regions of different B faster than the magnetic field changes in time, so for them, the field is essentially static. They represent the majority of the plasma particles, because the field changes are slow, and, therefore, we will call them the bulk particles (following Southwood & Kivelson 1993). The bulk particles almost do not change their energy $W = W_{\parallel} + W_{\perp}$, and it is simply exchanged between perpendicular and parallel degrees of freedom to conserve the magnetic moment. Hence, the changes in W_{\perp} and W_{\parallel} of such particles, as they travel along the field, can be expressed as

$$\delta W_{\perp} = \mu \delta B, \quad (1.22)$$

$$\delta W_{\parallel} = \delta W - \mu \delta B, \quad (1.23)$$

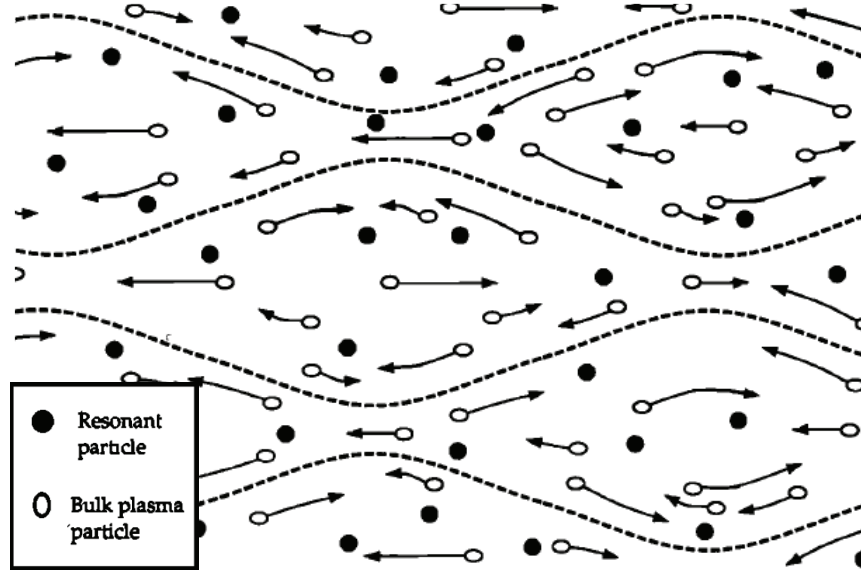


Figure 1.6: Mechanism of the mirror instability. The white particles represent the bulk of the plasma: they travel through the field structure as the instability develops. The bulk particles experience both increasing and decreasing field, while their energy does not change significantly but shifts back and forth between parallel and perpendicular degrees of freedom. If there is a positive temperature anisotropy, the bulk particles' pressure responds in antiphase to the magnetic perturbation [equation (1.24)]. The black particles are resonant. They have close to zero parallel velocities, move little along the field, and “feel” the local temporal changes of the magnetic-field strength: they heat in the regions of growing field, and cool in the regions of decreasing field by adjusting their perpendicular velocities to the field strength as to conserve the magnetic moment (betatron heating/cooling). Their pressure changes in phase with the magnetic perturbation.

where for the bulk particles, $\delta W \rightarrow 0$. The value of the distribution function F for any particle remains constant as the particle moves (the Liouville theorem). Then one can use this fact to find the change in the distribution function of the bulk particles associated with the spatial variations of the field strength that the particle encounters on its way:

$$\delta F_b = -\delta W_{\parallel} \frac{\partial F_b}{\partial W_{\parallel}} - \delta W_{\perp} \frac{\partial F_b}{\partial W_{\perp}} = \frac{\mu \delta B}{T_{\perp}} \left(1 - \frac{T_{\perp}}{T_{\parallel}} \right) F_b. \quad (1.24)$$

Here δ denotes the Lagrangian variation along the particle's trajectory. This equation showcases a peculiar behavior of the bulk particles: their distribution function (and the corresponding pressure) responds in antiphase to a change in the magnetic field if the anisotropy of the particles is positive ($T_{\perp} > T_{\parallel}$). This fact eventually leads to an instability, because in regions of the increasing field strength, the bulk particles' pressure is dropping.

Now let me study a small fraction of particles with low parallel velocities $v_{\parallel} < \gamma/k_{\parallel}$ (pitch angles close to 90°). These particles “feel” the local temporal change in the magnetic-field strength. Therefore, they increase/decrease their perpendicular (and total) energy

and heat/cool in regions where the field strength is rising/dropping via betatron heating/cooling, in radical contrast with the bulk particles (see Fig. 1.6). For this reason, we will call them resonant. The energy of a resonant particle, $W = W_{\perp} + W_{\parallel}$, changes in phase with the magnetic perturbation in order to conserve the particle's magnetic moment:

$$\frac{dW}{dt} = \mu \frac{\partial B}{\partial t}, \quad (1.25)$$

where d/dt is the Lagrangian time derivative. Then, integrating (1.25) for a harmonic perturbation of the field strength [equation (1.21)], I get

$$\delta W = \frac{\gamma}{\gamma + ik_{\parallel}v_{\parallel}} \mu \delta B. \quad (1.26)$$

The corresponding variation of the distribution function of the resonant particles is

$$\delta F_{\text{res}} = -\frac{\partial F_{\text{res}}}{\partial W} \delta W = -\frac{\partial F_{\text{res}}}{\partial W_{\parallel}} \delta W = \frac{\mu \delta B}{T_{\parallel}} \frac{\gamma}{\gamma + ik_{\parallel}v_{\parallel}} F_{\text{res}} \quad (1.27)$$

We can now calculate the total change in the distribution function δF taking account of both types of particles by combining equations (1.24) and (1.27):

$$\delta F = -\delta W_{\parallel} \frac{\partial F}{\partial W_{\parallel}} - \delta W_{\perp} \frac{\partial F}{\partial W_{\perp}} = \left[\frac{\mu \delta B}{T_{\perp}} \left(1 - \frac{T_{\perp}}{T_{\parallel}} \right) + \left(\frac{\mu \delta B}{T_{\parallel}} \frac{\gamma}{\gamma + ik_{\parallel}v_{\parallel}} \right) \right] F. \quad (1.28)$$

Taking the second moment of δF and imposing the pressure balance condition yields

$$\frac{B \delta B}{4\pi} + 2p_{\perp} \left(1 - \frac{T_{\perp}}{T_{\parallel}} \right) \frac{\delta B}{B} + 2 \left(\int dv_{\parallel} \frac{\gamma^2}{\gamma^2 + k_{\parallel}^2 v_{\parallel}^2} F_{\parallel} \right) \frac{T_{\perp}^2}{T_{\parallel}} \frac{\delta B}{B} = 0, \quad (1.29)$$

where F_{\parallel} is the distribution of parallel velocities after integration over the perpendicular velocities. In equation (1.29), the second term corresponds to the pressure deficit/surplus of the bulk particles with a positive anisotropy in regions where the field strength is increasing/decreasing [see equation (1.24)]. The first term is the magnetic pressure that resists compression in regions where the field increases and the bulk particles cause a deficit of pressure. Lastly, the third term describes the contribution of the resonant particles to the total pressure: their pressure responds in phase with the magnetic perturbation, in great contrast with the bulk particles. Thus, the antiphase response of the bulk particles is balanced by the magnetic pressure and the resonant pressure. Using equation (1.29) in the limit $\gamma \rightarrow 0$, one arrives at the mirror instability growth rate

$$\gamma = -k_{\parallel} \frac{B^2/(8\pi) + T_{\parallel} - T_{\perp}}{\pi(T_{\perp}^2/T_{\parallel})F_{\text{res}\parallel}}, \quad (1.30)$$

where $F_{\text{res}\parallel} = F_{\parallel}(0)$. A peculiar feature of the mirror instability is that its growth rate is inversely proportional to the number of resonant particles, unlike for other resonant

instabilities. Using $F_{\parallel}(0) = (m_i/2\pi T_{\parallel})^{1/2}$, $v_{\text{th}\parallel} = (T_{\parallel}/m_i)^{1/2}$ (parallel thermal velocity), I can rewrite equation (1.30) as

$$\gamma = \left(\frac{2}{\pi}\right)^{1/2} \frac{\beta_{\parallel}}{\beta_{\perp}^2} \left[\beta_{\perp} \left(\frac{\beta_{\perp}}{\beta_{\parallel}}\right) - 1 \right] k_{\parallel} v_{\text{th}\parallel}. \quad (1.31)$$

For small anisotropy typical for the ICM ($\Delta \sim 0.01$), $\beta_{\perp} \approx \beta_{\parallel} \approx \beta$, and equation (1.31) becomes considerably simplified

$$\gamma = \left(\frac{2}{\pi}\right)^{1/2} \left[\Delta - \frac{1}{\beta} \right] k_{\parallel} v_{\text{th}\parallel}. \quad (1.32)$$

The growth rate is positive when

$$\Delta > \frac{1}{\beta}, \quad (1.33)$$

which is the mirror instability condition. For the typical cluster parameters ($\Delta \sim 0.01$, $\beta \sim 100$), it is likely to be triggered by turbulent stretching of the magnetic-field lines virtually everywhere in the ICM. This conjecture is based on the fact that the fluctuation dynamo predicts the folded structure of the field lines. In this structure, field reversals, where the field strength is decreasing and the firehose instability develops, occupy only a small fraction of the volume, while field-line stretching occurs in most of the plasma.

The mirror instability is saturated in two phases (Kivelson & Southwood, 1996; Schekochihin et al., 2008; Kunz et al., 2014). After the initial exponential growth, the magnetic field becomes strong enough to drive the plasma to the marginal state $\Delta \rightarrow 1/\beta$. Magnetically trapped particles play a crucial role in the saturation mechanism. Their relative fraction is $\sim (\delta B/B)^{1/2}$ [recall that trapped particles are outside of the loss cone, $\xi < \xi_{\text{crit}} = (1 - B/B_{\text{max}})^{1/2} \sim (\delta B/B)^{1/2}$, see equation (1.16)]. The magnetic field can be decomposed into two components:

$$\mathbf{B} = \langle \mathbf{B} \rangle + \delta \mathbf{B}. \quad (1.34)$$

The first component is the mean field amplified by a positive macroscopic linear shear S , $d \ln |\langle \mathbf{B} \rangle| / dt = S$. The second is the growing mirror perturbations. Passing particles only detect the mean growth, while for trapped particles in magnetic wells, the mean growth is compensated by the deepening of the wells. Therefore, the average amplification of the magnetic field is compensated by the decreasing field in regions sampled by trapped particles:

$$-\frac{d \overline{|\delta \mathbf{B}|}}{dt} \sim \frac{d |\delta \mathbf{B}|^{3/2}}{dt} \sim \frac{d \ln |\langle \mathbf{B} \rangle|}{dt} = S, \quad (1.35)$$

where the overbar denotes averaging along particle trajectories (i.e., bounce-averaging for trapped particles). This leads to a secular growth of the mirror perturbations, $\langle \delta B^2 \rangle \sim (St)^{4/3}$. During this phase, particles mostly conserve their magnetic moments, i.e., there is no anomalous particle scattering off magnetic perturbations. The second phase, the final

saturation, is caused by particle scattering off sharp bends in the magnetic field, which occur at the boundaries of the magnetic mirrors. This behavior was recently confirmed in numerical simulations by Kunz et al. (2014).

The role of instabilities

The main role of the two instabilities is to hold the plasma anisotropy between the two margins: $-2/\beta < \Delta < 1/\beta$ (see, e.g., Melville et al., 2015, and references therein). Recalling equation (1.7),

$$\frac{|S|}{\nu_{ii}} \lesssim 1/\beta. \quad (1.36)$$

This means that in order to hold the plasma in the marginal state, either the rate of strain S or the scattering rate ν_{ii} has to be modified by the instabilities (e.g., Mogavero & Schekochihin, 2014). Both scenarios affect the generation of magnetic field by the fluctuation dynamo (Section 1.2.3).

In the first case, the growth rate of the magnetic field is suppressed, and for a simplified model, Mogavero & Schekochihin (2014) demonstrated that the fluctuating dynamo is incapable of amplifying the magnetic field from the seed values of $10^{-21} - 10^{-9} \mu\text{G}$ to the currently observed strength of $\sim 1 - 10 \mu\text{G}$. In the second case, the effective scattering rate is enhanced (possibly by anomalous particle scattering off Larmor-scale magnetic perturbations), so the Reynolds number grows larger in equation (1.4). As shown by Schekochihin & Cowley (2006), this scenario leads to an explosive growth of the magnetic field, and dynamo is, in fact, self-accelerating. In this case, the fluctuation dynamo is well capable of bringing the field to the currently observed values in a cosmologically short time. This result might be important in view of the concerns that the cluster lifetime may not be sufficient for the unmodified fluctuation dynamo to amplify the magnetic field at low Reynolds numbers in the bulk of the ICM.

Another potential consequence of the enhanced-collisionality scenario is that in the regions of magnetic-field reversals, where the field is weak, the firehose instability can amplify the field, thus increasing the scale of the field reversals to $\sim 0.1 - 1 \text{ kpc}$ (Schekochihin & Cowley, 2006). This could reconcile the fluctuation dynamo theory, which originally predicts reversals at the resistive scale, with Faraday rotation observations. Below the reversal scale, a cascade of Alfvén waves might be set up. Such fluctuations would have a $k^{-5/3}$ spectrum, as shown by Goldreich & Sridhar (1995), based on the conjecture that at each scale, the Alfvén frequency is equal to the turbulent decorrelation time. A $k^{-5/3}$ spectrum in the Faraday rotation observations of Hydra A (Kuchar & Enßlin, 2011; Vogt & Enßlin, 2005) could be associated with these fluctuations.

More importantly for my work, magnetic perturbations generated by the mirror instability may dramatically affect transport processes. One could reasonably assume that the mirror instability occurs in most of the ICM volume, based on the fluctuation dynamo arguments given above. Then magnetic mirrors formed by the instability can potentially inhibit thermal conduction by trapping of the heat-conducting electrons. I study this effect in detail in Chapter 3.

1.3 Thermal conduction in the intracluster medium

Current active research areas in the physics of galaxy clusters include, but are not limited to, non-thermal particles, AGN feedback and formation of large-scale structure. Proper modeling of these phenomena requires a good understanding of the underlying physics of the intracluster gas. An important ingredient to this understanding is particle transport. While transport processes cannot be self-consistently modeled in large-scale cluster simulations, they may effect the large-scale properties of clusters, such as temperature profiles. It is therefore desirable to implement a certain subgrid model that would contain the microscale physics of particle transport in a handful of numerical parameters. Besides, galaxy clusters might be unique laboratories to study turbulent high- β plasmas, which are difficult to produce in ground-based experiments. In this work, I mainly study thermal conduction in the ICM.

1.3.1 Spitzer thermal conductivity

The ICM is a fully ionized hot tenuous plasma. In such a plasma, the mean free paths of the particles are determined by Coulomb collisions. It can be shown by a simple calculation of the small-angle scattering of an electron in the electric field of an ion that the electron-ion collision frequency $\nu_{ei} \propto n/T^{3/2}$. Let me briefly recap this calculation. Consider an electron at speed v with impact parameter b scattered by an ion with charge Z (Fig. 1.7). The electron is scattered at small angle θ , so that its absolute velocity almost does not change. The electron's velocity vector is deflected by the component of the Coulomb force perpendicular to the electron's motion, $F_{\perp} = b/r \times Ze^2/r^2$, which acts over time $\Delta t \sim b/v$. The change in the perpendicular velocity of the electron is $v_{\perp} = F_{\perp} \Delta t / m_e = Ze^2 b^2 / (m_e v r^3) \sim Ze^2 / (m_e b v)$. Then the parallel electron's velocity changes by

$$\Delta v_{\parallel} = v(1 - \cos \theta) \sim v \frac{\theta^2}{2} \sim \frac{\Delta v_{\perp}^2}{2v} \sim \frac{Z^2 e^4}{m_e^2 b^2 v^3}. \quad (1.37)$$

Integrating over impact parameters b , one can obtain the change in the parallel momentum ΔP_{\parallel} over time Δt of an electron beam of density n as it is scattered by the ion:

$$\frac{\Delta P_{\parallel}}{\Delta t} = \int_{b_{\min}}^{b_{\max}} db 2\pi b m_e n v \Delta v_{\parallel} = \frac{Z^2 e^4}{m_e v^2} \ln \frac{b_{\max}}{b_{\min}}. \quad (1.38)$$

Here $\ln(b_{\max}/b_{\min}) \equiv \ln \Lambda$ is the Coulomb logarithm, which is a weak function of the plasma parameters. For the typical cluster densities and temperatures, $\ln \Lambda \sim 40$. The collision frequency can be defined as the rate of loss of the parallel beam's momentum, $\nu_{ei} \equiv -P_{\parallel}^{-1} \Delta P_{\parallel} / \Delta t$. Finally, I get

$$\nu_{ei} \sim \frac{Z^2 e^4 n}{m_e^2 v^3} \ln \Lambda. \quad (1.39)$$

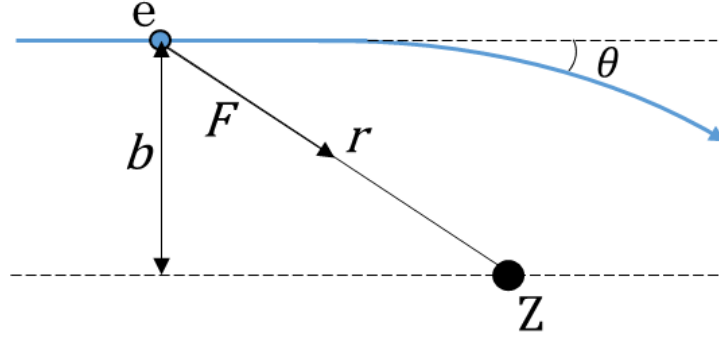


Figure 1.7: A sketch of a small-angle Coulomb collision.

The cluster plasma is dominated by hydrogen, therefore, $Z \sim 1$. For collisions between thermal particles to within a factor of order unity

$$\nu_{ei} \sim \nu_{ee} \sim \frac{ne^4}{m_e^{1/2} T^{3/2}} \ln \Lambda. \quad (1.40)$$

To obtain the electron-electron collision frequency ν_{ee} from the electron-ion one, it is only necessary to replace the electron mass m_e by the reduced mass $m_e/2$, so $\nu_{ee} = \sqrt{2}\nu_{ei}$. The collisional mean free path is, therefore,

$$\lambda_{\text{mfp}} \sim \frac{T^2}{ne^4 \ln \Lambda}. \quad (1.41)$$

The electron and ion mean free paths are equal if both species are at the same temperature T . A rigorous derivation was performed by Spitzer (1956), whose result is

$$\lambda_{\text{mfp}} = \frac{3^{3/2} T^2}{4\pi^{1/2} ne^4 \ln \Lambda}. \quad (1.42)$$

Numerically,

$$\lambda_{\text{mfp}} \approx 23 \text{ kpc} \left(\frac{T}{10^8 \text{ K}} \right)^2 \left(\frac{n}{10^{-3} \text{ cm}^{-3}} \right)^{-1}. \quad (1.43)$$

Let me now discuss thermal conduction. Because electrons are much faster than ions, heat is primarily transported by electrons. If one assumes a non-magnetized plasma with an electron temperature gradient first, then heat is conducted down the gradient. If the scale length of the temperature gradient is much longer than the mean free path, the heat flux is

$$\mathbf{q} = -\kappa \nabla T. \quad (1.44)$$

Spitzer (1956) calculated the thermal conductivity κ in a hydrogen plasma taking into account the effects of the electric field induced by the flow of conducting electrons. His expression is

$$\kappa_{\text{Sp}} = 0.76 n \lambda_{\text{mfp}} v_{\text{th},e} \approx 4.6 \times 10^{13} \left(\frac{T}{10^8 \text{ K}} \right)^{5/2} \left(\frac{\ln \Lambda}{40} \right)^{-1} \text{ ergs s}^{-1} \text{ cm}^{-1} \text{ K}^{-1}. \quad (1.45)$$

A very strong dependence of the Spitzer thermal conductivity on temperature is evident. One can estimate the conduction timescale characteristic of clusters:

$$t_{\text{cond}} \sim n l_T^2 / \kappa_{\text{Sp}} \sim 10^7 \frac{n}{10^{-3} \text{ cm}^{-3}} \left(\frac{l_T}{100 \text{ kpc}} \right)^2 \left(\frac{T}{10^8 \text{ K}} \right)^{-5/2} \text{ yr}, \quad (1.46)$$

where l_T is the length scale of the temperature gradient. It is a rather short time compared with the typical dynamic time scales of the ICM. This means, had thermal conduction been so efficient, various temperature substructures observed in clusters [cold fronts (e.g., Markevitch & Vikhlinin, 2007), filaments (e.g., Fabian et al., 2011), etc.], would not have survived during cluster evolution.

1.3.2 Braginskii thermal conductivity

At the ICM temperature and density, even a very small dynamically unimportant magnetic field is capable of completely magnetizing the plasma. Indeed, the electron ion Larmor radius

$$\rho_e \approx 10^{-13} \text{ kpc} \left(\frac{T}{10^8 \text{ K}} \right)^{1/2} \left(\frac{B}{1 \text{ } \mu\text{G}} \right)^{-1} \quad (1.47)$$

is extremely small compared to almost any other characteristic length scale in clusters. In such a plasma, heat flux inevitably becomes strongly anisotropic. A full kinetic calculation of anisotropic transport coefficients in a magnetized plasma was first carried out by Braginskii (1965). It is clear, however, that the electron conductivity perpendicular to the magnetic-field lines κ_{\perp} is negligible, because $\kappa_{\perp} \sim n \rho_e^2 \nu_e \sim n (\rho_e / \lambda_{\text{mfp}})^2 \kappa_{\text{Sp}} \ll \kappa_{\text{Sp}}$, where ν_e is the electron collision frequency. This is because an electron moves only a perpendicular distance ρ_e in each scattering. Then the ICM electrons transfer heat predominantly along the field lines with parallel thermal conductivity κ_{\parallel} , which is equal to the Spitzer conductivity [equation (1.45)] if it is not suppressed by any additional physics. The heat flux in the presence of a magnetic field can be written as

$$\mathbf{q} = \kappa_{\parallel} \mathbf{b} \mathbf{b} \cdot \nabla T, \quad (1.48)$$

where \mathbf{b} is the unit vector in the direction of the local magnetic field. This expression shows that only the component of the temperature gradient parallel to the magnetic field is effective in driving a heat flux. At the same time, only the component of the resulting heat flux $q_{\nabla T}$ parallel to the temperature gradient transports any net energy,

$$q_{\nabla T} = \cos^2 \theta \kappa_{\parallel} \nabla T, \quad (1.49)$$

where θ is the angle between the magnetic field and the temperature gradient. Thus, the effective heat flux along the gradient is suppressed by the factor $\cos^2 \theta$.

Nevertheless, the ICM is turbulent, while its magnetic field is frozen into the plasma because of a very small resistivity. Consequently, it is natural to expect that the topology of the field lines in the ICM is stochastic. This can also be seen in RM maps (e.g.,

in the Hydra A cluster core in Fig. 1.3). Thermal conduction in a tangled magnetic field is a complicated problem on its own, but it is even more aggravated by the temporal evolution of the field and temperature gradients, which might be important locally (Chapter 2). Moreover, it is not known if the parallel conductivity actually has the Spitzer value, because various mechanisms of its suppression potentially exist. For instance, magnetic mirrors at the scale below the mean free path could reduce it (Chapter 3), or scattering off magnetic perturbations at the electron Larmor scales, presumably produced by electron kinetic instabilities (Riquelme et al., 2016).

1.3.3 Conduction in tangled magnetic fields

Particle transport in tangled magnetic fields was originally studied as applied to cosmic rays (Skilling et al., 1974) and Tokamak plasma (Rechester & Rosenbluth, 1978). Here I briefly describe the Rechester-Rosenbluth theory of conduction in a tangled magnetic field, based mainly on the work by Chandran & Cowley (1998).

Assume first for simplicity that a stochastic magnetic field has a single scale l_B , so that each field line can be treated as a random-walk path of step length l_B . Let me also consider the field to be static, neglecting all fluid motions. The net displacement of an electron that has traveled distance l along a field line is $\delta r \sim (D_B l)^{1/2}$, where D_B is called the “magnetic diffusion coefficient”. Because the step of the field-line random walk is l_B , $D_B \sim l_B$. An electron diffuses along a field line with parallel diffusivity D_{\parallel} , so its parallel displacement is $l \sim (D_{\parallel} t)^{1/2}$. If the electron always stays on the same field line, its parallel diffusive motion is superimposed on the spatial diffusion of the field line, giving the net displacement $\delta r \sim t^{1/4}$, and there is no spatial diffusion. However, it was demonstrated by Rechester & Rosenbluth (1978) that small motions perpendicular to field lines can restore the diffusive behavior of electrons due to the exponential divergence of neighboring field lines. In a chaotic field, the separation d between two nearby field lines increases on average with distance l along either field line as

$$d(l) \sim d(0)e^{l/L_K}, \quad (1.50)$$

where L_K is the Kolmogorov-Lyapunov length (Rechester & Rosenbluth, 1978). In general, L_K depends on the magnetic-field spectrum, but since in our case the field is characterized by only one scale l_B , $L_K \sim l_B$.

Suppose a particle is moving from point P toward point Q (see Fig. 1.8) along a field line (the solid curve). Each time it travels a distance l_B , it drifts a distance $\sim \rho_e$ perpendicular to the magnetic field due to the field-line curvature and field strength gradients. Assume, for the moment, that the electron drifts a distance ρ_e onto a neighboring line only once. It then continues its motion along the neighboring line (the dotted curve), which diverges exponentially from the initial field line. The electron’s perpendicular distance from the original field line becomes $\sim l_B$ after it has traveled distance L_{RR} along the new line (point R),

$$L_{RR} \sim l_B \ln \frac{l_B}{\rho_e}. \quad (1.51)$$

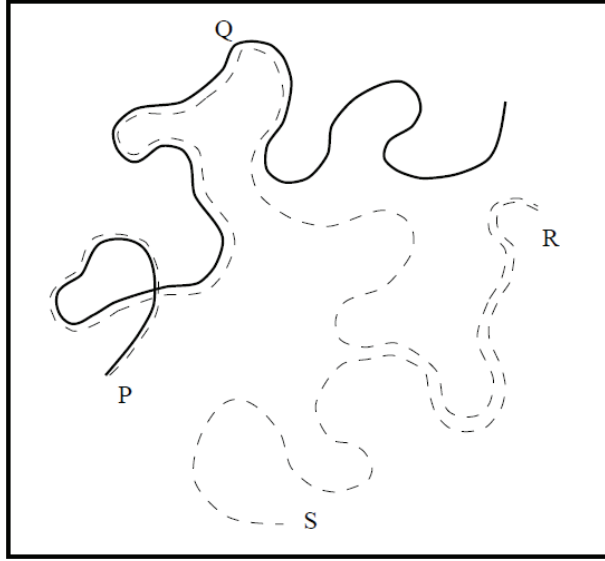


Figure 1.8: Diffusion in a tangled magnetic field (adapted from Chandran & Cowley 1998).

$L_{RR} \sim 30l_B$ (taking $l_B/\rho_e \sim 10^{13}$, typical for clusters) is called the Rochester-Rosenbluth length. Because the electron constantly drifts transverse to the field lines, L_{RR} is slightly overestimated. After the electron has traveled the distance PR , its subsequent motion is completely uncorrelated with its initial field line. That means, if at point R , the electron is reflected by a collision (or a magnetic mirror), it does not return to point P (as it would have done, had there been no transverse diffusion), but follows along the line segment RS instead. Thus, a very small amount of perpendicular diffusion restores the electron's random walk in space. Let me calculate the diffusion coefficient of such motion.

The three-dimensional net displacement of the electron as it has traveled a distance L_{RR} along the tangled field line is

$$\delta r^2 \sim D_B L_{RR} \sim l_B L_{RR}. \quad (1.52)$$

Because further motion of the particle is uncorrelated with its previous path, δr is the effective step of the isotropic electron's random walk in space. Consider first the limit $\lambda_{mfp} \gg L_{RR}$. In this limit, the electron does not collide over a distance L_{RR} , and the time it takes for it to move L_{RR} along the field line is $\delta t \sim L_{RR}/v_{th,e}$. Then, for $t > \delta t$, it diffuses isotropically in three dimensions with diffusion coefficient ³

$$D \sim \delta r^2 / \delta t = v_{th,e} l_B. \quad (1.53)$$

So, when $\lambda_{mfp} \gg L_{RR}$, the collisional mean free path of particles λ_{mfp} is replaced by the correlation length of the tangled magnetic field l_B . In the opposite limit, $\lambda_{mfp} \ll L_{RR}$ (which more likely applies to the ICM, because $\lambda_{mfp} \sim 10$ kpc, $L_{RR} \sim 30l_B \sim 100$ kpc), the electron *diffuses* a distance L_{RR} along the field line over time $\delta t \sim L_{RR}^2/D_{\parallel}$, where

³The diffusivity D is related to the thermal conductivity κ as $\kappa \sim nD$.

$D_{\parallel} = 1/3v_{\text{th},e}\lambda_{\text{mfp}}$ is the parallel diffusivity. Then, for $t > \delta t$, the effective spatial diffusion coefficient is

$$D \sim \delta r^2 / \delta t \sim v_{\text{th},e} \lambda_{\text{mfp}} \frac{l_B}{3L_{\text{RR}}} \sim 10^{-2} D_{\text{Sp}}, \quad (1.54)$$

where D_{Sp} is the Spitzer diffusivity ($\kappa_{\text{Sp}} = nD_{\text{Sp}}$). The effective transverse electron diffusion is thus greatly enhanced by the stochasticity of the field lines, while the total diffusion coefficient is about two orders of magnitude smaller than the Spitzer value.

It should be noted, however, that the cluster magnetic field can be turbulent in a broad range of scales (taking into account Alfvénic magnetic fluctuations below the viscous scale). In this case, the Rochester-Rosenbluth length L_{RR} should be corrected accordingly. Narayan & Medvedev (2001) applied the model of strong MHD turbulence to the chaotic fluctuations in the ICM and obtained a value of L_{RR} of only $\sim l_B$. Their estimate of the effective diffusivity is $D_{\text{turb}} \sim D_{\text{Sp}}/5$.

1.4 Structure of the thesis

This work aims to study some of the effects of magnetic fields on thermal conduction in the ICM. The work is based on one published and two submitted papers.

In Chapter 2, I investigate the magnetohydrodynamic effect of the correlated evolution of the magnetic field and temperature gradients in the ICM turbulence. This effect leads to local suppression of thermal conduction and may explain the long lifetime of temperature fluctuations in the ICM.

In Chapter 3, I study, with the help of hybrid-kinetic simulations, how the mirror instability can inhibit electron transport in the ICM via magnetic trapping.

The generation of polarization of thermal bremsstrahlung emission as a result of electron pressure anisotropy in the ICM is studied in Chapter 4. The small degree of polarization obtained by my calculation could be a potential estimator of electron collisionality in the ICM.

Finally, my findings are summarized in Conclusions.

Bibliography

- Ackermann M., Ajello M., Albert A., Allafort A., Atwood W. B., Baldini L., Ballet J., Barbiellini G., Bastieri D., Bechtol K., Bellazzini R., Bloom E. D., 2014, *ApJ*, 787, 18
- Batchelor G. K., 1950, *Proceedings of the Royal Society of London Series A*, 201, 405
- Birkinshaw M., 1979, *MNRAS*, 187, 847
- Boehringer H., Voges W., Fabian A. C., Edge A. C., Neumann D. M., 1993, *MNRAS*, 264, L25
- Bradt H., Mayer W., Naranan S., Rappaport S., Spada G., 1967, *ApJ*, 150, L199
- Braginskii S. I., 1965, *Reviews of Plasma Physics*, 1, 205
- Brunetti G., Lazarian A., 2007, *MNRAS*, 378, 245
- Byram E. T., Chubb T. A., Friedman H., 1966, *Science*, 152, 66
- Carilli C. L., Taylor G. B., 2002, *ARA&A*, 40, 319
- Cavaliere A., Danese L., de Zotti G., 1979, *A&A*, 75, 322
- Chandran B. D. G., Cowley S. C., 1998, *Phys. Rev. Lett.*, 80, 3077
- Churazov E., Brüggen M., Kaiser C. R., Böhringer H., Forman W., 2001, *ApJ*, 554, 261
- Churazov E., Forman W., Jones C., Böhringer H., 2000, *A&A*, 356, 788
- Churazov E., Vikhlinin A., Zhuravleva I., Schekochihin A., Parrish I., Sunyaev R., Forman W., Böhringer H., Randall S., 2012, *MNRAS*, 421, 1123
- Clarke T. E., Ensslin T., 2006, *Astronomische Nachrichten*, 327, 553
- Dolag K., Grasso D., Springel V., Tkachev I., 2005, *J. Cosmology Astropart. Phys.*, 1, 009
- Dreher J. W., Carilli C. L., Perley R. A., 1987, *ApJ*, 316, 611
- Ensslin T. A., Biermann P. L., Klein U., Kohle S., 1998, *A&A*, 332, 395

- Enßlin T. A., Vogt C., 2006, *A&A*, 453, 447
- Fabian A. C., Sanders J. S., Allen S. W., Canning R. E. A., Churazov E., Crawford C. S., Forman W., Gabany J., Hlavacek-Larrondo J., Johnstone R. M., Russell H. R., Reynolds C. S., Salomé P., Taylor G. B., Young A. J., 2011, *MNRAS*, 418, 2154
- Fabian A. C., Sanders J. S., Ettori S., Taylor G. B., Allen S. W., Crawford C. S., Iwasawa K., Johnstone R. M., Ogle P. M., 2000, *MNRAS*, 318, L65
- Fabian A. C., Sanders J. S., Williams R. J. R., Lazarian A., Ferland G. J., Johnstone R. M., 2011, *MNRAS*, 417, 172
- Feretti L., Dallacasa D., Govoni F., Giovannini G., Taylor G. B., Klein U., 1999, *A&A*, 344, 472
- Forman W., Kellogg E., Gursky H., Tananbaum H., Giacconi R., 1972, *ApJ*, 178, 309
- Fujita Y., 2005, *ApJ*, 631, L17
- Gilfanov M. R., Syunyaev R. A., Churazov E. M., 1987, *Soviet Astronomy Letters*, 13, 3
- Gnedin N. Y., Ferrara A., Zweibel E. G., 2000, *ApJ*, 539, 505
- Goldreich P., Sridhar S., 1995, *ApJ*, 438, 763
- Govoni F., Feretti L., 2004, *International Journal of Modern Physics D*, 13, 1549
- Govoni F., Taylor G. B., Dallacasa D., Feretti L., Giovannini G., 2001, *A&A*, 379, 807
- Grasso D., Rubinstein H. R., 2001, *Phys. Rep.*, 348, 163
- Gunn J. E., 1978, in Maeder A., Martinet L., Tammann G., eds, *Saas-Fee Advanced Course 8: Observational Cosmology Advanced Course The Friedmann models and optical observations in cosmology*. p. 1
- Kellogg E., Gursky H., Tananbaum H., Giacconi R., Pounds K., 1972, *ApJ*, 174, L65
- Kivelson M. G., Southwood D. J., 1996, *J. Geophys. Res.*, 101, 17365
- Kronberg P. P., Dufton Q. W., Li H., Colgate S. A., 2001, *ApJ*, 560, 178
- Kuchar P., Enßlin T. A., 2011, *A&A*, 529, A13
- Kunz M. W., Schekochihin A. A., Stone J. M., 2014, *Physical Review Letters*, 112, 205003
- Laing R. A., Bridle A. H., Parma P., Murgia M., 2008, *MNRAS*, 391, 521
- Large M. I., Mathewson D. S., Haslam C. G. T., 1959, *Nature*, 183, 1663
- Markevitch M., Vikhlinin A., 2007, *Phys. Rep.*, 443, 1

- Melville S., Schekochihin A. A., Kunz M. W., 2015, ArXiv e-prints
- Mogavero F., Schekochihin A. A., 2014, MNRAS, 440, 3226
- Mukhanov V., 2005, Physical Foundations of Cosmology
- Narayan R., Medvedev M. V., 2001, ApJ, 562, L129
- Norman M. L., Bryan G. L., 1999, in Röser H.-J., Meisenheimer K., eds, The Radio Galaxy Messier 87 Vol. 530 of Lecture Notes in Physics, Berlin Springer Verlag, Cluster Turbulence. p. 106
- Peacock J. A., 1999, Cosmological Physics
- Peebles P. J. E., 1993, Principles of Physical Cosmology
- Prokhorov D. A., Churazov E. M., 2014, A&A, 567, A93
- Rechester A. B., Rosenbluth M. N., 1978, Phys. Rev. Lett., 40, 38
- Ricker P. M., Sarazin C. L., 2001, ApJ, 561, 621
- Riquelme M., Quataert E., Verscharen D., 2016, ArXiv: 1602.03126
- Schekochihin A. A., Cowley S. C., 2006, Phys. Plasmas, 13, 056501
- Schekochihin A. A., Cowley S. C., Kulsrud R. M., Rosin M. S., Heinemann T., 2008, Physical Review Letters, 100, 081301
- Schekochihin A. A., Cowley S. C., Taylor S. F., Maron J. L., McWilliams J. C., 2004, ApJ, 612, 276
- Schuecker P., Finoguenov A., Miniati F., Böhringer H., Briel U. G., 2004, A&A, 426, 387
- Silk J., White S. D. M., 1978, ApJ, 226, L103
- Skilling J., McIvor I., Holmes J. A., 1974, MNRAS, 167, 87P
- Southwood D. J., Kivelson M. G., 1993, J. Geophys. Res., 98, 9181
- Spitzer L., 1956, Physics of Fully Ionized Gases
- Sunyaev R. A., Norman M. L., Bryan G. L., 2003, Astronomy Letters, 29, 783
- Sunyaev R. A., Zeldovich Y. B., 1972, Comments on Astrophysics and Space Physics, 4, 173
- Taylor G. B., Perley R. A., 1993, ApJ, 416, 554

- Vikhlinin A., Kravtsov A. V., Burenin R. A., Ebeling H., Forman W. R., Hornstrup A., Jones C., Murray S. S., Nagai D., Quintana H., Voevodkin A., 2009, *ApJ*, 692, 1060
- Vogt C., Enßlin T. A., 2005, *A&A*, 434, 67
- Willson M. A. G., 1970, *MNRAS*, 151, 1
- Zel'dovich Y. B., Ruzmaikin A. A., Molchanov S. A., Sokolov D. D., 1984, *Journal of Fluid Mechanics*, 144, 1
- Zeldovich Y. B., Ruzmaikin A. A., Sokoloff D. D., 1990, *The Almighty Chance. Series: World Scientific Lecture Notes in Physics*, ISBN: [ISBN 978-9971-5-0916-3](#)/ISBN. WORLD SCIENTIFIC, Edited by Ya B Zeldovich, A A Ruzmaikin and D D Sokoloff, vol. 20, 20
- Zhuravleva I., Churazov E., Arévalo P., Schekochihin A. A., Allen S. W., Fabian A. C., Forman W. R., Sanders J. S., Simionescu A., Sunyaev R., Vikhlinin A., Werner N., 2015, *MNRAS*, 450, 4184
- Zhuravleva I., Churazov E., Schekochihin A. A., Allen S. W., Arévalo P., Fabian A. C., Forman W. R., Sanders J. S., Simionescu A., Sunyaev R., Vikhlinin A., Werner N., 2014, *Nature*, 515, 85
- Zhuravleva I. V., Churazov E. M., Sazonov S. Y., Sunyaev R. A., Dolag K., 2011, *Astronomy Letters*, 37, 141

Chapter 2

Suppression of local heat flux in a turbulent magnetized intracluster medium

MNRAS, 2014, 440, 1153

S. V. Komarov, E. M. Churazov, A. A. Schekochihin and J. A. ZuHone

Abstract. X-ray observations of hot gas in galaxy clusters often show steeper temperature gradients across cold fronts – contact discontinuities, driven by the differential gas motions. These sharp (a few kpc wide) surface brightness/temperature discontinuities would be quickly smeared out by the electron thermal conduction in unmagnetized plasma, suggesting significant suppression of the heat flow across the discontinuities. In fact, the character of the gas flow near cold fronts is favorable for suppression of conduction by aligning magnetic field lines along the discontinuities. We argue that a similar mechanism is operating in the bulk of the gas. Generic 3D random isotropic and incompressible motions increase the temperature gradients (in some places) and at the same time suppress the *local* conduction by aligning the magnetic field lines perpendicular to the *local* temperature gradient. We show that the suppression of the effective conductivity in the bulk of the gas can be linked to the increase of the frozen magnetic field energy density. On average the rate of decay of the temperature fluctuations $d\langle\delta T^2\rangle/dt$ decreases as $\langle B^2\rangle^{-1/5}$.

2.1 Introduction

X-ray observations of galaxy clusters reveal significant spatial fluctuations of the gas temperature in a range of spatial scales (e.g. Markevitch et al., 2003). Given a temperature map with prominent fluctuations, it is possible to calculate an upper limit on the effective thermal conductivity, provided that the lifetime of the fluctuations can be estimated. It turns out to be at least an order of magnitude lower than the Spitzer conductivity for unmagnetized plasma (Ettori & Fabian, 2000; Markevitch et al., 2003).

Heat conduction in the intracluster medium (ICM) is primarily along the field lines because the Larmor radius of the particles is very small compared to the collisional mean free path (Braginskii, 1965). The ICM undergoes turbulent motion in a range of spatial scales (Inogamov & Sunyaev, 2003; Schuecker et al., 2004; Schekochihin & Cowley, 2006; Subramanian et al., 2006; Zhuravleva et al., 2011). As the magnetic field is, to a good approximation, frozen into the ICM, the field lines become tangled by gas motions and their topology changes constantly. Four main effects should be considered. First, parallel thermal conduction along stochastic magnetic field lines may be reduced because the heat-conducting electrons become trapped and detrapped between regions of strong magnetic field (magnetic mirrors; see Chandran & Cowley 1998; Chandran et al. 1999; Malyskin & Kulsrud 2001; Albright et al. 2001). Secondly, diffusion in the transverse direction may be boosted due to spatial divergence of the field lines (Skilling et al., 1974; Rechester & Rosenbluth, 1978; Chandran & Cowley, 1998; Narayan & Medvedev, 2001; Chandran & Maron, 2004). Thirdly, there is effective diffusion due to temporal change in the magnetic field ('field-line wandering'). Finally, if one is interested in temperature fluctuations and their diffusion, one must be mindful of the fact that the temporal evolution of the magnetic field is correlated with the evolution of the temperature field because the field lines and the temperature are advected by the same turbulent velocity field.

In this chapter, we focus on the last effect. The more conventional approach, often used to estimate the relaxation of the temperature gradients, is to consider the temperature distribution as given and study the effect of a tangled magnetic field on the heat conduction. However, the direction and value of the fluctuating temperature gradients are not statistically independent of the direction of the magnetic-field lines because the latter are also correlated with the turbulent motions of the medium. We argue that, dynamically, the fluctuating gradients tend to be oriented perpendicular to the field lines and so heat fluxes are the more heavily suppressed the stronger the thermal gradients are. We also establish the relationship between the average conductivity and the growth of the magnetic energy density.

The structure of the chapter is as follows. In Section 2.2, we provide a qualitative explanation of the correlation between the temperature gradients and the magnetic-field direction, accompanied by a number of numerical examples. In Section 2.3, a theoretical framework for modelling this effect is presented and the joint PDF of the thermal gradients, the angles between these gradients and the magnetic-field lines and the magnetic-field strength is derived in the solvable case of a simple model velocity field. The connection between the effective conductivity and the increase of the magnetic energy density is es-

established. Analytical results are supplemented by numerical calculations in Section 2.3.4, which extrapolate our results to the case of a more general velocity field. In Section 2.4, we discuss the assumptions that have been necessary to enable analytical treatment, the consequent limitations on the applicability of our results, and also present some numerical tests using a global dynamical cluster simulation, which suggest that, at least qualitatively, our results survive when most of the simplifying assumptions are relaxed. Finally, in Section 2.5, we sum up our findings.

2.2 Qualitative discussion

We consider a volume of plasma with high electric conductivity and frozen-in magnetic field tangled on a scale much greater than the mean free path of the particles. We also assume the plasma motions to be incompressible, which is a good approximation for subsonic dynamics. Across the paper we treat the temperature as a passive scalar.

2.2.1 Illustrative example: conduction between converging layers of magnetised plasma

Consider two parallel layers of an incompressible medium vertically separated by distance h with temperatures $T_1 \neq T_2$. This is illustrated in Fig. 2.1: the direction of the field line is shown with the inclined solid line, making an angle θ with the vertical, so $\cos \theta = h/\sqrt{h^2 + l^2}$, where l is the horizontal distance between the footpoints of the field line anchored in the two layers. An incompressible flow with $\partial_y u_y < 0$ reduces h and increases l so that $l \times h$ is conserved (in the absence of tangential shear). Here we are interested in the heat exchange between the layers, i.e. only the component of the heat flux along the temperature gradient $Q_{\nabla T}$ has to be calculated:

$$Q_{\nabla T} = \chi(\mathbf{b} \cdot \nabla T) \cos \theta = \kappa \frac{T_2 - T_1}{\sqrt{h^2 + l^2}} \frac{h}{\sqrt{h^2 + l^2}}. \quad (2.1)$$

Let $h(t) = h_0 f(t)$ and $l(t) = l_0/f(t)$. Then

$$Q_{\nabla T} = \kappa \frac{T_2 - T_1}{h_0} \frac{f}{f^2 + (l_0/h_0)^2 f^{-2}}, \quad (2.2)$$

where κ is the parallel thermal conductivity coefficient (Braginskii, 1965), which is assumed constant across the volume for simplicity. Therefore, in the limit of $f \rightarrow 0$, $Q_{\nabla T} \rightarrow 0$ if $l_0 \neq 0$. Similarly, when $f \rightarrow \infty$, $Q_{\nabla T} \rightarrow 0$. The decrease of the heat flux at $f > 1$ is simply due to the increase of the distance between the plates and corresponding decrease of the temperature gradient. The decrease at $f < 1$ is due to systematic increase of the angle between the field lines and the direction of the temperature gradient.

If at some moment the field lines are tangled in such a way that all angles θ are equally probable, then parametrizing compression/stretching along y by the same factor f and

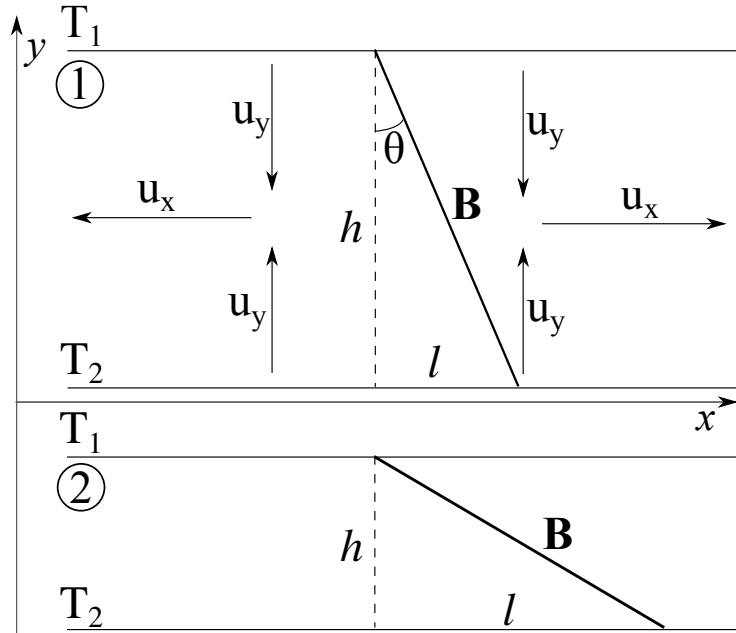


Figure 2.1: Correlated changes of the temperature gradients and the inclination of the magnetic-field lines in the case of a converging incompressible flow: plane parallel layers at different temperatures. Converging flow with $\partial_y u_y < 0$ reduces h and increases the temperature gradient $(T_2 - T_1)/h$, but suppresses heat flux. The solid line represents the direction of the magnetic field. If the medium is incompressible then $l \times h$ is conserved (in the absence of tangential shears).

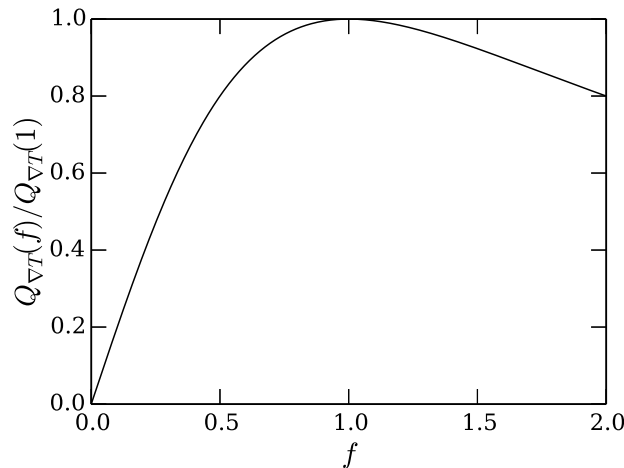


Figure 2.2: Suppression of the heat flux along the temperature gradient between two approaching/receding plates as a function of distance f between the plates, when the medium between the plates is threaded by tangled magnetic field [see equation (2.3)]. At the initial moment ($f = 1$), all angles between the magnetic field direction and the plates are equally probable. The decrease of the heat flux at $f > 1$ is simply due to the increase of the distance between the plates and corresponding decrease of the temperature gradient. The decrease at $f < 1$ is due to systematic increase of the angle between the field lines and the direction of the temperature gradient.

averaging over θ gives us the suppressed heat flux along the temperature gradient:

$$Q_{\nabla T} = \kappa \frac{T_2 - T_1}{h_0} \frac{2f}{f^2 + 1} \text{ (see Fig. 2.2)}. \quad (2.3)$$

Thus, increasing the temperature gradient by squeezing the layers of the gas does not boost the heat exchange between them but rather makes it smaller. A qualitatively similar situation might occur at the cold fronts – contact discontinuities formed by differential gas motions, a very simple model of which is discussed in the next subsection.

2.2.2 Astrophysical example: model of a cold front

Chandra observations of galaxy clusters often show sharp discontinuities in the surface brightness of the ICM emission (see review by Markevitch & Vikhlinin, 2007). Most of these structures have lower-temperature gas on the brighter (higher-density) side of the discontinuity, suggesting that they are contact discontinuities rather than shocks. In the literature, these structures are called ‘cold fronts’. Because of the sharp temperature gradients, the limits on the thermal conduction derived for the observed cold fronts are strong (see e.g. Ettori & Fabian, 2000; Vikhlinin et al., 2001; Xiang et al., 2007).

In the majority of theoretical models, the formation of a cold front involves relative motion of cold and hot gases. Here we consider the case of a hot gas flowing around a colder, gravitationally bound gas cloud, which is a prototypical model of a cold front. For simplicity, we assume that the velocity field can be approximated with a 2D potential flow past a cylinder, while the initial temperature is symmetric around the cylinder. The initial temperature distribution and stream lines of the flow are shown in the left panel of Fig. 2.3. The middle panel shows the field lines of a random magnetic field superimposed on the initial temperature distribution. The evolved temperature and magnetic field are shown in the right panel of Fig. 2.3. Stretching of the fluid elements near the stagnation point along the front leads to the contraction of the same elements in the direction perpendicular to the front. This configuration has been considered in a number of studies of the cold fronts (see e.g. Asai et al., 2007; Churazov & Inogamov, 2004; Roediger et al., 2011; Lyutikov, 2006). Qualitatively, it corresponds to the situation sketched in Section 2.2.1 and Fig. 2.1, which naturally leads to the field lines orthogonal to the temperature gradient at the front.

2.2.3 Local correlation between the magnetic-field strength and the heat flux

Let us now discuss the suppression of the local heat flux in more general terms. Consider the induction equation for an incompressible medium and the advection equation for the

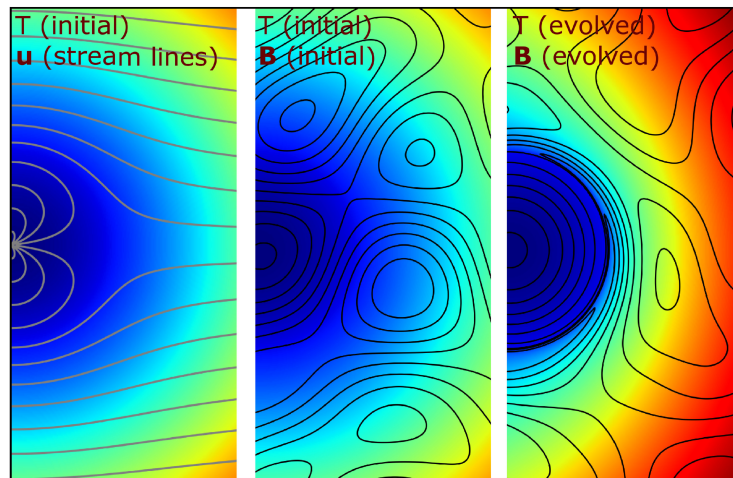


Figure 2.3: Alignment of the field lines perpendicular to the temperature gradient for the velocity field characteristic of a cold front. A potential flow past a cylinder is used in this example. The left panel shows the initial temperature distribution (color image) and stream lines of the velocity field. The middle panel shows a random tangled magnetic field superposed on the initial temperature distribution. The right panel shows the time-evolved temperature map and magnetic-field lines (superposed contours) in such a flow. The flow boosts the temperature gradient at the cold front and at the same time stretches the field lines along the lines of constant temperature. In the resulting configuration, the field lines are essentially perpendicular to the sharp temperature gradient at the front.

temperature:

$$\frac{d\mathbf{B}}{dt} = \mathbf{B} \cdot \nabla \mathbf{u}, \quad (2.4)$$

$$\frac{dT}{dt} = 0, \quad (2.5)$$

where \mathbf{B} is the magnetic field, \mathbf{u} the velocity field, T temperature and $d/dt = \partial/\partial t + \mathbf{u} \cdot \nabla$. We have neglected thermal and magnetic diffusivities. While equation (2.5) is not a full magnetohydrodynamic energy equation, it is correct in the limit of an incompressible non-stratified medium (we will further discuss its applicability in Section 2.4). Let \mathbf{g} be the unit vector in the direction of the temperature gradient, \mathbf{b} the unit vector in the direction of the field line, B the magnetic field magnitude and G the temperature gradient magnitude, so $\mathbf{B} = B\mathbf{b}$, $\nabla T = G\mathbf{g}$. The above equations imply

$$\frac{dG}{dt} = -G\mathbf{g} \cdot (\nabla \mathbf{u}) \cdot \mathbf{g}, \quad (2.6)$$

$$\frac{dB}{dt} = B\mathbf{b} \cdot (\nabla \mathbf{u}) \cdot \mathbf{b}, \quad (2.7)$$

$$\frac{d\mu}{dt} = \mu[\mathbf{g} \cdot (\nabla \mathbf{u}) \cdot \mathbf{g} - \mathbf{b} \cdot (\nabla \mathbf{u}) \cdot \mathbf{b}], \quad (2.8)$$

where $\mu = \mathbf{b} \cdot \mathbf{g}$, the cosine of the angle between \mathbf{B} and ∇T . From these equations, we can immediately infer the following equation for $\mathbf{b} \cdot \nabla T = G\mu$, a quantity proportional to the parallel heat flux:

$$\frac{d \ln(G\mu)}{dt} = -\frac{d \ln B}{dt}. \quad (2.9)$$

Thus, locally, the heat flux decreases as the field strength grows.

2.2.4 Numerical example: a random 2D velocity field

In this example, we consider a random temperature distribution and a random magnetic field in a random δ -correlated-in-time (white) Gaussian 2D velocity field (Fig. 2.4). The temperature $T(x, y)$, the magnetic field $\mathbf{B}(x, y)$ and the velocity field $\mathbf{u}(x, y)$ (assumed incompressible, $\nabla \cdot \mathbf{u} = 0$) are modelled as superpositions of Fourier harmonics with random phases and amplitudes. The temperature and the magnetic field are advected according to equations (2.4) and (2.5). The velocity field is renewed at each time step (white-in-time field). The initial conditions are shown in the top panel of Fig. 2.4; there is no initial correlation between the temperature gradients and the orientation of the field lines. With time, preferential stretching/squeezing of the fluid elements leads to alignment of the field lines along the iso-temperature lines (see bottom panel in Fig. 2.4). This happens in all regions where the stretching/squeezing is sufficiently strong. As a result, the field lines are mostly perpendicular to the direction of the temperature gradient in all regions where the gradient is large. Intuitively, one expects that in a turbulent conducting medium, this tendency of local alignment between the magnetic field and the isotherms will manifest

itself statistically. In the next section, we work out a simple statistical model of this process.

2.3 Heat conduction in a stochastic velocity field

Here we treat the suppression of the heat conduction using an analytically solvable model that allows us to predict the statistical distribution of the cosine of the angle between the thermal gradient and the field line (μ), the magnitude of the thermal gradient (G) and the magnetic-field strength (B). After the joint probability distribution function (PDF) of μ , G and B is derived (Section 2.3.5), we will be in a position to assess how statistically prevalent the behaviour discussed in Section 2.2.4 is, but we will preface this detailed calculation with some simpler arguments to quantify the suppression of the heat flux.

2.3.1 Relaxation of temperature fluctuations

Let us restore heat conduction in equation (2.5):

$$\frac{dT}{dt} = \nabla \cdot (\kappa \mathbf{b} \mathbf{b} \cdot \nabla T), \quad (2.10)$$

where χ is the parallel thermal conductivity coefficient (Braginskii, 1965). Then the volume-averaged rate of change of the rms temperature fluctuations is

$$\frac{d\langle \delta T^2 \rangle}{dt} = -2\kappa \langle |\mathbf{b} \cdot \nabla \delta T|^2 \rangle = -2\kappa \langle G^2 \mu^2 \rangle. \quad (2.11)$$

Thus, the average value of $G^2 \mu^2$ characterizes the rate at which local temperature variations are wiped out by the thermal conduction.

2.3.2 Kazantsev-Kraichnan model

We consider the magnetic field to be so weak that it does not affect the velocity field. This condition is only satisfied if the magnetic energy density is much lower than the kinetic energy density of the plasma motions. This means that our model does not describe the saturated state, when these energy densities become comparable. The non-saturated regime could be a common transient situation in the ICM, at least locally, in the sense that at any given time, the magnetic field is amplified up to the saturation value only in a small fraction of the volume.

We will wish to calculate the joint PDF $p(\mu, G, B; t)$, where μ and G are defined in Section 2.2, and investigate the evolution of the relevant correlations, viz., $\langle G^2 \mu^2 \rangle$ (see Section 2.3.1). To do that, we need to average the dynamical equations for \mathbf{g} , \mathbf{b} , G and B

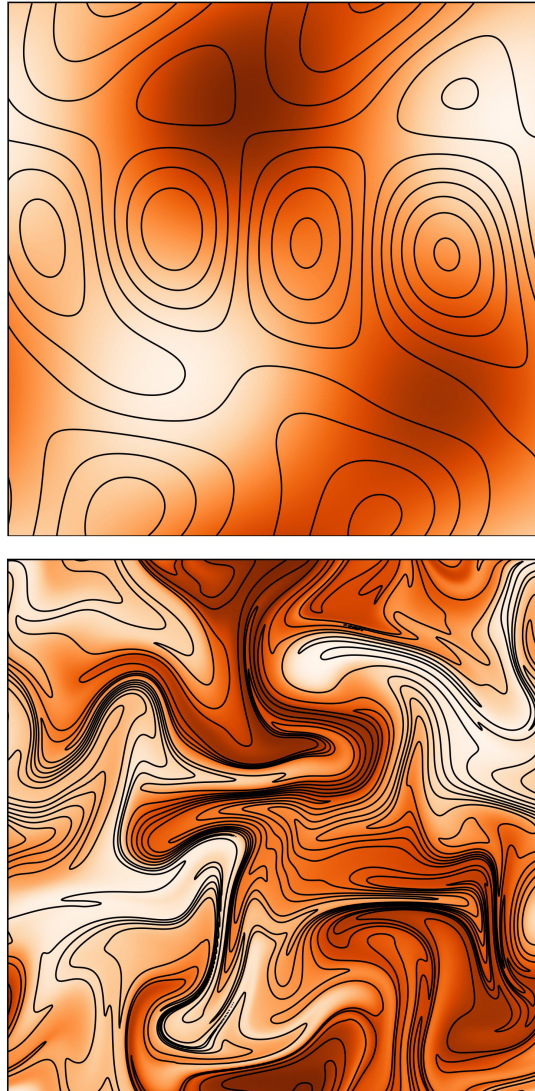


Figure 2.4: Alignment of the field lines perpendicular to the temperature gradient for a stochastic δ -correlated-in-time Gaussian incompressible velocity field, modelled as a superposition of Fourier harmonics with random phases and amplitudes. The top panel shows the initial random temperature distribution (color) with the field lines of a random magnetic field superposed (they are uncorrelated with temperature). The bottom panel shows the same fields later on in the evolution. In the evolved image, field lines follow the lines of constant temperature in the regions where the temperature gradient is large.

over all realizations of the stochastic velocity field. The equations are

$$\begin{aligned}\frac{dg^k}{dt} &= -(\delta_m^k - g^k g^m) g^i \partial_m u^i, \\ \frac{db^k}{dt} &= (\delta_i^k - b^k b^i) b^m \partial_m u^i, \\ \frac{dG}{dt} &= -G g^i g^m \partial_m u^i, \\ \frac{dB}{dt} &= B b^i b^m \partial_m u^i,\end{aligned}\tag{2.12}$$

where summation over repeated indices is implied.

This problem is solvable analytically for a Gaussian white-in-time velocity field (Kazantsev, 1968):

$$\langle u^i(t, \mathbf{x}) u^j(t', \mathbf{x}') \rangle = \delta(t - t') \kappa^{ij}(\mathbf{x} - \mathbf{x}'),\tag{2.13}$$

where κ^{ij} is the correlation tensor, whose form can be determined from symmetry and incompressibility considerations. We may assume the medium to be isotropic and homogeneous. Let us restrict our consideration to variation of magnetic field and temperature on spatial scales much smaller than that of the velocity field. Then, at any arbitrary point in space, the velocity can be expanded in linear approximation:

$$u^i(t, \mathbf{x}) = \sigma_m^i(t) x^m,\tag{2.14}$$

where $\sigma_m^i(t) = \partial_m u^i$ and we have assumed $u^i(t, 0) = 0$ without loss of generality (otherwise change the reference frame). Then the velocity gradients satisfy

$$\begin{aligned}\left\langle \frac{\partial u^i}{\partial x^m}(t, \mathbf{x}) \frac{\partial u^j}{\partial x^n}(t', \mathbf{x}') \right\rangle \Big|_{\mathbf{x}=\mathbf{x}'} &= \langle \sigma_m^i(t) \sigma_n^j(t') \rangle \\ &= \delta(t - t') \epsilon_{mn}^{ij},\end{aligned}\tag{2.15}$$

where

$$\epsilon_{mn}^{ij} = - \frac{\partial^2 \epsilon^{ij}(\mathbf{y})}{\partial y_m \partial y_n} \Big|_{\mathbf{y}=0} \equiv \epsilon T_{mn}^{ij}$$

and $\epsilon = 1/\tau_{\text{eddy}}$, τ_{eddy} being the turnover time of the turbulent eddies and

$$T_{mn}^{ij} = \delta^{ij} \delta_{mn} - \frac{1}{D+1} (\delta_m^i \delta_n^j + \delta_n^i \delta_m^j)\tag{2.16}$$

is the inevitable tensor form of ϵ_{mn}^{ij} for an isotropic incompressible medium of dimension D ($= 2, 3$). This is the so-called Kazantsev-Kraichnan model, which has been a popular tool for modelling the properties of small-scale dynamo and passive-scalar advection in turbulent media (e.g., Chertkov et al., 1999; Balkovsky & Fouxon, 1999; Boldyrev & Schekochihin, 2000; Schekochihin et al., 2002, 2004; Boldyrev & Cattaneo, 2004, and references therein).

2.3.3 Relation between magnetic-field amplification and suppression of conduction for the white-in-time velocity field

Before presenting the full statistical calculation, we wish to give a relatively simple one that establishes the connection between the relaxation rate of the temperature fluctuations and the magnetic-energy density. The heat flux along the field line $G\mu$ is inversely proportional to the length of a field-line segment s . Therefore, one can relate the change of the mean square heat flux $\langle G^2\mu^2 \rangle$, which is also the decay rate of the temperature fluctuations (see Section 2.3.1), to the growth of the magnetic-energy density as follows:

$$\langle B^2 \rangle \propto \langle s^2 \rangle, \quad \langle G^2\mu^2 \rangle \propto \langle 1/s^2 \rangle. \quad (2.17)$$

As explained in Section 2.3.2, we assume an isotropic linear random velocity field. Let it be piecewise constant in time over intervals τ_c and completely uncorrelated for $\Delta t > \tau_c$. Assume further that the amount of stretching of any fluid element over individual time intervals of duration $\sim \tau_c$ is small compared to the size of the element, which amounts to a model of white-noise field. Under these assumptions, it is easy to obtain the PDF of s as a function of time t in the limit $t/\tau_c \gg 1$. The evolution of each component of the separation vector \mathbf{x} of any two locations frozen into a velocity field constant over time interval τ_c is

$$x^i(\tau_c) \approx x^i(0) + \tau_c \sigma_j^i x^j(0) + \frac{1}{2} \tau_c^2 \sigma_j^i \sigma_k^j x^k(0) + O(\tau_c^3), \quad (2.18)$$

where σ_j^i is the velocity gradients matrix [see equation (2.14)]. Since we are dealing with a random isotropic field, we can set $\mathbf{x}(0) = (1, 0, 0)$ at $t = 0$. Then

$$\begin{aligned} x^1(\tau_c) &\approx 1 + \tau_c \sigma_1^1 + \frac{1}{2} \tau_c^2 \sigma_j^1 \sigma_1^j + O(\tau_c^3), \\ x^{i \neq 1}(\tau_c) &= \tau_c \sigma_1^i + O(\tau_c^2). \end{aligned} \quad (2.19)$$

We are interested in the time evolution of the ‘stretching factor’ $s^2 = |\mathbf{x}|^2$. For one ‘act of stretching’, equation (2.19) implies

$$\ln s^2(\tau_c) = 2\tau_c \sigma_1^1 - 2\tau_c^2 (\sigma_1^1)^2 + \tau_c^2 \sigma_1^j \sigma_1^j + \tau_c^2 \sigma_j^1 \sigma_1^j + O(\tau_c^3). \quad (2.20)$$

For $t \gg \tau_c$, the calculation of $s^2(t)$ reduces to summation of $N = t/\tau_c \gg 1$ such independent stretching episodes:

$$\ln s^2(t) = \sum \ln s^2(\tau_c). \quad (2.21)$$

After applying the central limit theorem to $(1/N) \sum \ln s^2(\tau_c)$, one readily gets the PDF of s^2 :

$$P(s^2) = \frac{1}{s^2} \frac{1}{\sqrt{2\pi\sigma_s^2}} \exp \left[-\frac{(\ln s^2 - m_s)^2}{2\sigma_s^2} \right], \quad (2.22)$$

where

$$\begin{aligned}\sigma_s &= 2\sqrt{T_{11}^{11}\frac{t}{\tau_{\text{eddy}}}}, \\ m_s &= \left[-2T_{11}^{11} + \sum_{i=1}^d (T_{11}^{ii} + T_{1i}^{i1}) \right] \frac{t}{\tau_{\text{eddy}}},\end{aligned}\quad (2.23)$$

where τ_{eddy} and T_{mn}^{ij} are defined at the end of Section 2.3.2. We have taken $\delta(0) = 1/\tau_c$ in equation (2.15). Using equation (2.17), we get

$$\langle B^2 \rangle \propto e^{m_s + \sigma_s^2/2}, \quad \langle G^2 \mu^2 \rangle \propto e^{-m_s + \sigma_s^2/2}. \quad (2.24)$$

This leads to a simple relation between the growing magnetic-energy density and the evolution of the mean square heat flux:

$$\langle G^2 \mu^2 \rangle \propto \langle B^2 \rangle^p, \quad \text{where } p = \frac{-m_s + \sigma_s^2/2}{m_s + \sigma_s^2/2}. \quad (2.25)$$

For an incompressible velocity field in 3D, using equation (2.16), we get $p = -1/5$. This is a statistical version of the dynamical equation (2.9). It implies that on average, as the magnetic-energy density grows, the rate of decay of the temperature fluctuations is reduced, although the efficiency of this reduction is modest (p is low). This is because $\langle G^2 \mu^2 \rangle$ is dominated by regions of low stretching while $\langle B^2 \rangle$ by regions of high stretching [equation (2.17)] and the distribution of these is highly intermittent.

2.3.4 Finite-time-correlated velocity field

How sensitive is this result to the obviously unphysical assumption of zero correlation time? Here, we numerically calculate the PDF of s in a random incompressible 3D velocity field evolving according to a Langevin equation with a finite correlation time. This is a generalization of the δ -correlated case considered in Section 2.3.3.

We consider a large number of independent field-line segments, each one placed in its own stochastic incompressible velocity field, given by equation (2.14), with the velocity gradient satisfying

$$\frac{d\sigma_m^i}{dt} = -\frac{1}{\tau_c}\sigma_m^i + \partial_m a^i, \quad (2.26)$$

where τ_c is the correlation time and a^i is a stochastic Gaussian acceleration whose gradient satisfies

$$\langle \partial_m a^i(t) \partial_n a^j(t') \rangle = \delta(t - t') A^2 T_{mn}^{ij}. \quad (2.27)$$

Here A^2 is the noise amplitude and the dimensionless tensor T_{mn}^{ij} is fixed by isotropy and incompressibility as given by equation (2.16). It is possible to define the effective turn-over time of turbulent eddies τ_{eddy} in much the same way as we did for the δ -correlated case:

$$\int_0^\infty \langle \sigma_m^i(0) \sigma_n^j(t) \rangle dt = \frac{1}{2} A^2 \tau_c^2 T_{mn}^{ij} \equiv \frac{1}{2\tau_{\text{eddy}}}, \quad (2.28)$$

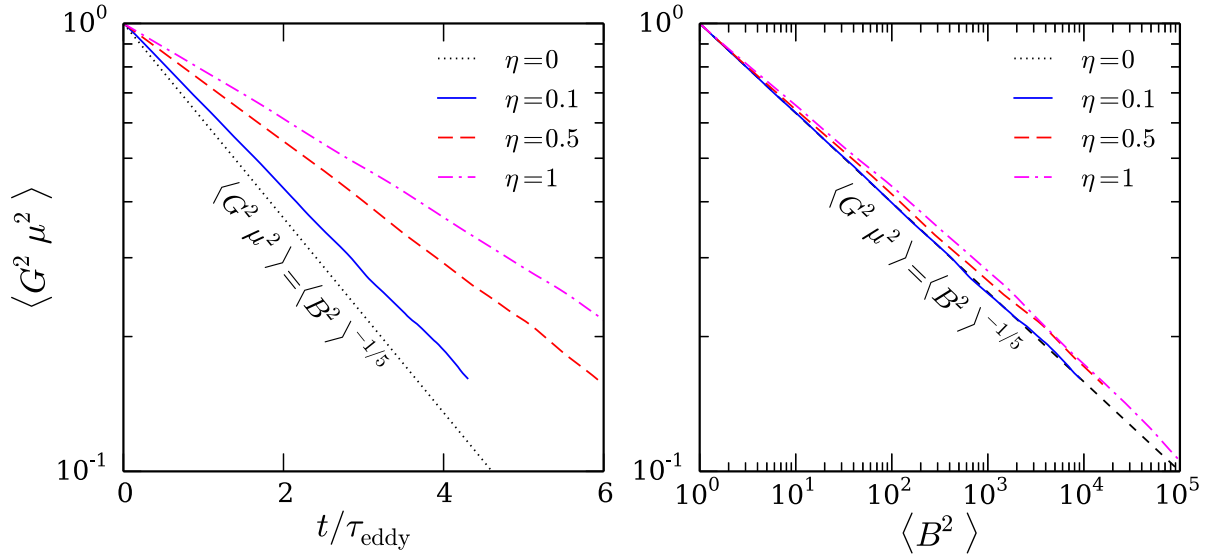


Figure 2.5: The decrease of the mean square heat flux $\langle G^2 \mu^2 \rangle$ for the time-correlated velocity field and different ratios $\tau_c/\tau_{\text{eddy}}$ (numerical results). While growth/decay rates of $\langle B^2 \rangle$ and $\langle G^2 \mu^2 \rangle$ change with correlation time, their relative behavior is practically the same: $\langle G^2 \mu^2 \rangle \propto \langle B^2 \rangle^{-0.2}$.

where the exact solution of the Langevin equation (2.26) has been substituted. Thus, $\tau_{\text{eddy}} = 1/(\tau_c A)^2$.

In view of equation (2.17), the evolution of $\langle G^2 \mu^2 \rangle$ and $\langle B^2 \rangle$ can be easily calculated from the distribution of the segment lengths. Here we do this for a range of values of the ratio $\tau_c/\tau_{\text{eddy}}$. In Section 2.3.3, we treated the case $\tau_c/\tau_{\text{eddy}} \rightarrow 0$ analytically, whereas for a physically sound case, $\tau_c/\tau_{\text{eddy}} \approx 1$ because typically turbulent velocities decorrelate over their eddy turnover times and fluid elements are stretched by order-unity amounts over the same time scales. The results are shown in Fig. 2.5. Even though the growth/decay rates of $\langle B^2 \rangle$ and $\langle G^2 \mu^2 \rangle$ do change with correlation time, their relative behaviour appears to be invariant, viz.,

$$\langle G^2 \mu^2 \rangle \propto \langle B^2 \rangle^{-1/5}, \quad (2.29)$$

practically the same as for the δ -correlated regime [cf. equation (2.25)].

Thus, finite correlation times do not change the form of the effective conduction-magnetic-energy-density relation, only modifying the time dependence. This result gives us some confidence in the Kazantsev-Kraichan velocity as a credible modelling choice.

2.3.5 Statistics of the heat flux

In this section we will finally derive the full joint statistical distribution of the fluctuating magnetic fields and temperature gradients and hence the detailed correlations between the heat flux, the field strength and the relative direction of the magnetic field and the temperature gradient.

For a velocity field given by equation (2.14), we can write equations (2.12) for \mathbf{g} , \mathbf{b} , G and B as follows:

$$\begin{aligned}\partial_t g^k &= -(\delta_m^k - g^k g^m) g^i \sigma_m^i, \\ \partial_t b^k &= (\delta_i^k - b^k b^i) b^m \sigma_m^i, \\ \partial_t G &= -G g^i g^m \sigma_m^i, \\ \partial_t B &= B b^i b^m \sigma_m^i.\end{aligned}\tag{2.30}$$

There are no advection terms here due to the homogeneity of the gas [so we can consider equation (2.12) at $\mathbf{x} = 0$].

The details of the derivation of the equation for the joint PDF $p(\mu, G, B; t)$ are presented in Appendix 2.6. The result is

$$\begin{aligned}\partial_t p &= \frac{\epsilon}{2(D+1)} [2D(1-\mu^2)(\mu\partial_\mu\mu\partial_\mu - \partial_G G\mu\partial_\mu - \partial_B B\mu\partial_\mu) \\ &\quad + (D-1)(\partial_G G\partial_G G + \partial_B B\partial_B B) + 2(1-\mu^2 D)\partial_G G\partial_B B \\ &\quad + D(D+1-2D\mu^2)(2\mu\partial_\mu - \partial_G G - \partial_B B) + 2D^2(1-D\mu^2)]p,\end{aligned}\tag{2.31}$$

where D is the dimension of space. From now on, we only consider $D = 3$.

Multiplying both sides of equation (2.31) by $G^2\mu^2$ and integrating, we find

$$\partial_t \langle G^2 \mu^2 \rangle = -\frac{\epsilon}{2} \langle G^2 \mu^2 \rangle,\tag{2.32}$$

so the mean square heat flux decays exponentially in time. Then, recalling equation (2.11) for the rate of smoothing of the temperature fluctuations,

$$\frac{d\langle \delta T^2 \rangle}{dt} \propto -e^{-\epsilon t/2} \rightarrow 0.\tag{2.33}$$

We observe that the relaxation rate of the temperature fluctuations decreases significantly on time-scales of the order of the turnover time of the turbulent eddies ($\epsilon = 1/\tau_{\text{eddy}}$).

It is also possible to recover the relation for the mean square heat flux as a function of the magnetic-energy density [equation (2.25)]. Multiplying equation (2.31) by B^2 and integrating, we obtain the evolution of the magnetic energy density:

$$\partial_t \langle B^2 \rangle = \frac{5}{2} \epsilon \langle B^2 \rangle.\tag{2.34}$$

This result, combined with equation (2.32), leads to the relation established in Section 2.3.3:

$$\langle G^2 \mu^2 \rangle = \langle B^2 \rangle^{-1/5}.\tag{2.35}$$

We expect that the temperature gradients and the magnetic-field lines will become perpendicular to each other. Let us then first investigate the limit of $\mu \rightarrow 0$, in which equation (2.31) can be solved analytically. Let $x = \ln \mu$, $y = \ln G$ and $z = \ln B$. Then the joint PDF of these variables is $h(x, y, z; t) = p(\mu(x), G(y), B(z); t)e^{x+y+z}$, where the last factor is the Jacobian of the transformation of variables. Taking $\mu \rightarrow 0$ in equation (2.31), we find that h satisfies

$$\partial_t h = \frac{\epsilon}{4}[3h_{xx} + h_{yy} + h_{zz} - 3(h_{xy} + h_{xz}) + h_{yz} + 3(2h_x - h_y - h_z)]. \quad (2.36)$$

Let us now write h in the following form:

$$h(x, y, z; t) = f(x, y; t)\delta(x + y + z). \quad (2.37)$$

Substituting this ansatz into equation (2.36), we find that the factorization goes through and f satisfies

$$\partial_t f = \frac{\epsilon}{4}[3f_{xx} + f_{yy} - 3f_{xy} + 3(2f_x - f_y)]. \quad (2.38)$$

This factorization implies that in the limit $\mu \rightarrow 0$, $G\mu \propto 1/B$ independently of the initial conditions. This result was anticipated in Section 2.3.3, where we took the ratio of $G\mu$ and $1/B$ to be the same for all the segments of the field lines at the initial moment.

Let us make another transformation: $\xi = x = \ln \mu$ and $\eta = x + 2y = \ln(G^2\mu)$ to separate variables in equation (2.38). The joint PDF of these two variables, $w(\xi, \eta; t) = f(x(\xi), y(\xi, \eta); t)$, satisfies

$$\partial_t w = \frac{\epsilon}{4}(3w_{\xi\xi} + w_{\eta\eta} + 6w_\xi). \quad (2.39)$$

This equation can be readily solved:

$$w(\xi, \eta; t) = \frac{1}{\sqrt{3\pi\epsilon t}} \int_{-\infty}^{+\infty} d\xi' d\eta' w(\xi', \eta'; 0) \exp \left\{ -\frac{1}{3\epsilon t} \left[\frac{3}{2}\kappa t + (\xi - \xi') \right]^2 \right\} \quad (2.40)$$

$$\times \exp \left\{ -\frac{1}{\epsilon t} (\eta - \eta')^2 \right\}. \quad (2.41)$$

Notice that along with diffusion in both variables, the PDF drifts to $\xi \rightarrow -\infty$, i.e. to smaller μ . So there is a continued tendency towards mutually perpendicular orientation of the thermal gradients and the field lines.

If one is interested how the joint PDF of μ and G behaves in the case of μ of order unity, the full equation (2.31) integrated over B has to be solved. Technically speaking, we are obliged to do this in order to ascertain that the limit $\mu \rightarrow 0$ was the relevant one to consider, i.e. that the joint distribution of μ and G moves towards smaller μ independently of initial conditions. Again, to separate variables, we employ the variables $\xi = \ln \mu$ and $\eta = \ln(G^2\mu)$. The PDF of these variables, $w(\xi, \eta; t) = \int p(\mu(\xi), G(\xi, \mu), B; t)e^{\frac{1}{2}(\xi+\eta)} dB$, satisfies

$$\partial_t w = \frac{\epsilon}{4}[3(1 - e^{2\xi})w_{\xi\xi} + (1 + 3e^{2\xi})w_{\eta\eta} + 6(1 - 2e^{2\xi})w_\xi - 12e^{2\xi}w]. \quad (2.42)$$

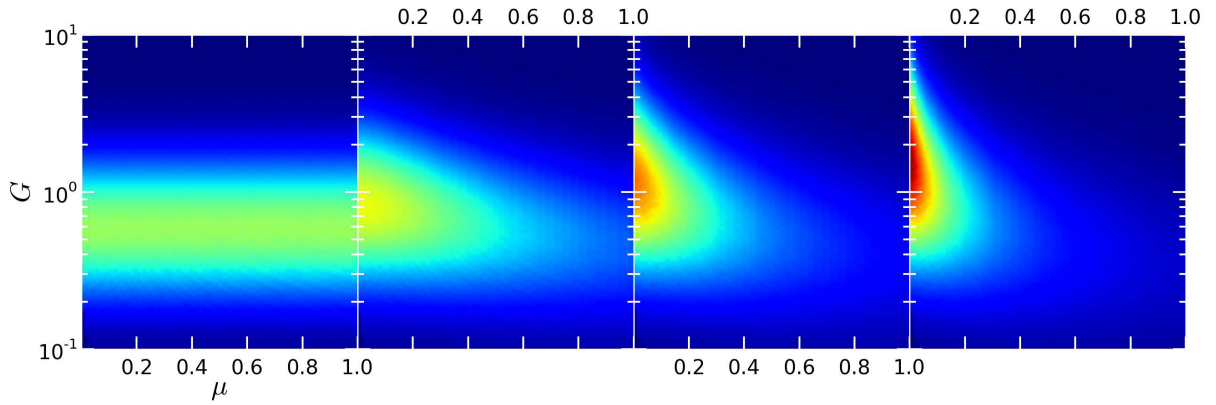


Figure 2.6: Evolution of the joint PDF of μ and G at regular time intervals from $t = 0$ to $t = \tau_{\text{eddy}}$ (turn-over time of the turbulent eddies) obtained via numerical solution of the equation (2.43). The maximum of the function drifts to the region where the thermal gradients and the field lines are perpendicular ($\mu \rightarrow 0$).

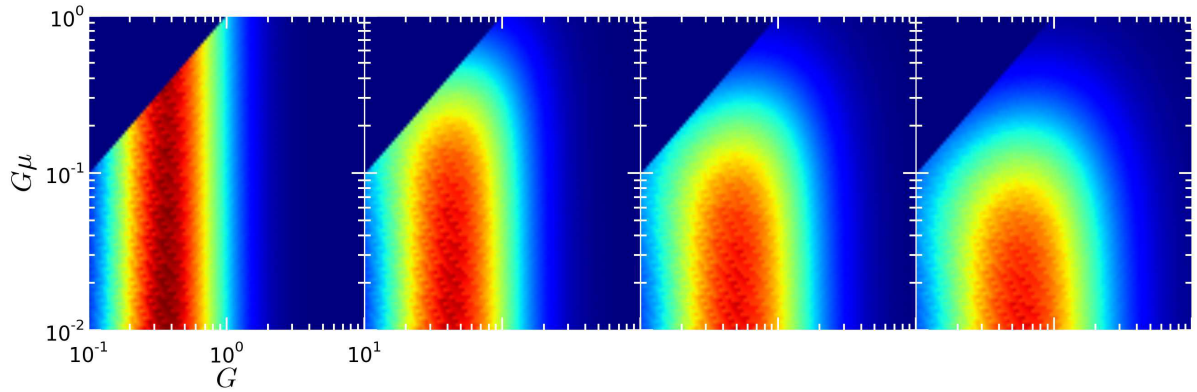


Figure 2.7: Evolution of the joint PDF in terms of heat flux $G\mu = |\mathbf{b} \cdot \nabla T|$ and $G = |\nabla T|$ at the same times as in Fig. 2.6. Sharper gradients tend to be wiped out slower due to the smaller corresponding values of the heat flux.

In order to solve this equation numerically, it is convenient to rewrite it in the divergence form as follows:

$$\partial_t w = \frac{\epsilon}{4} \{ \partial_\xi [2(1 - e^{2\xi}) + (1 - e^{2\xi})\partial_\xi] + \partial_\eta (1 + 3e^{2\xi})\partial_\eta \} w. \quad (2.43)$$

Numerical solution of this equation is presented in Fig. 2.6. With time, the maximum of the PDF does indeed shift towards smaller μ , demonstrating that the temperature gradient and the magnetic-field vector are becoming ever more orthogonal to each other. One can replot this graph in coordinates $G\mu$ (heat flux) and G to observe that the rate of smearing of the temperature fluctuations in equation (2.11) is correlated with the magnitude of the temperature gradients (Fig. 2.7) in such a way that sharper gradients on average tend to be wiped out slower due to smaller corresponding values of $G\mu$.

2.4 Limitations of our theory and a numerical test

We now discuss the assumptions we have made in our theory and the extent to which they limit its applicability.

2.4.1 Spatial scales

The ordering of scales in the problem considered in this paper obeys the following relations:

$$\rho_e \ll \lambda_{\text{mfp}} \lesssim l \lesssim \lambda_u, \quad (2.44)$$

where l is the characteristic size of the region we deal with, ρ_e is the electron Larmor radius, λ_{mfp} is the electron mean-free path and λ_u is the typical size of a turbulent eddy.

The limit $l \ll \lambda_u$ simplifies the calculation of the field-line stretching because the linear expansion of the velocity field can be used [equation (2.14)]. This allows for an analytic treatment of the problem. Note that the kinematic dynamo naturally sets the parallel correlation length of the magnetic field $\lambda_{B\parallel}$ to be $\sim \lambda_u$ (Schekochihin et al., 2002, 2004).

The condition $\lambda_{\text{mfp}} \lesssim l$ allows us to apply the thermal conduction equation (2.10) at these spatial scales. Due to the fact that in the kinematic-dynamo regime, $\lambda_u \sim \lambda_{B\parallel}$, we also have $\lambda_{\text{mfp}} \lesssim \lambda_{B\parallel}$. This limit being assumed, we can ignore the magnetic mirroring effects because the electrons are free to escape magnetic traps via collisional pitch-angle scattering (Chandran & Cowley, 1998; Chandran et al., 1999).

The typical value of the mean-free path between Coulomb collisions,

$$\lambda_{\text{mfp}} \sim 8 \text{ kpc} \left(\frac{T}{5 \text{ KeV}} \right)^2 \left(\frac{n_e}{10^{-3} \text{ cm}^{-3}} \right)^{-1}, \quad (2.45)$$

varies in cluster cores from 0.01 to 20 kpc depending on their temperature and density. For example, in the core of the Coma cluster, the mean-free path is ~ 5 kpc (Churazov et al., 2012); in M87/Virgo, it is much smaller, $\lambda_{\text{mfp}} \sim 0.01$ kpc, due to lower temperature

and higher density (Churazov et al., 2008). On the other hand, the value of λ_u can be in the range of 10 kpc to 200 kpc (Inogamov & Sunyaev, 2003; Schuecker et al., 2004; Schekochihin & Cowley, 2006; Subramanian et al., 2006; Zhuravleva et al., 2011; Kunz et al., 2011). Therefore, our analysis is relevant for temperature fluctuations on scales in the range 10^{-1} – 10^2 kpc. Some of these scales are directly resolvable with *Chandra* or *XMM-Newton*, suggesting that in observed substructures in the temperature maps, the isotherm contours should be roughly aligned with the magnetic-field lines.

2.4.2 Incompressibility

The assumption of incompressibility [needed to use equation (2.16)] for the description of the velocity field) is valid as long as the gas velocities are subsonic. This is reasonable for the ICM, except for cases of strong mergers or AGN-driven strong shocks in the very core of a cluster. The comparison of cluster-mass estimates from X-ray data and lensing or stellar kinematics (e.g. Churazov et al., 2008) and simulations (e.g. Lau et al., 2009) suggest that the kinetic energy of the gas motions is at the level of 5-15% of its thermal energy in relaxed clusters. Slight deviations from incompressibility should not dramatically alter our results.

2.4.3 Stratification

We have neglected the effects of stratification. It is well known that in the ICM anisotropic thermal conduction modifies the classical Schwarzschild stability criterion in such a way that any radial temperature gradient leads to an instability: the magnetothermal instability (MTI, Balbus 2000) if the thermal gradient and the gravity force are codirectional and the heat-flux-driven buoyancy instability (HBI, Quataert 2008) if they are oppositely directed. These instabilities have been extensively studied in numerical simulations (Sharma et al., 2009; Parrish et al., 2009; Bogdanović et al., 2009; Ruszkowski & Oh, 2010; Ruszkowski et al., 2011; McCourt et al., 2011; Kunz et al., 2012).

However, the instabilities are driven by large-scale mean gradients and in a turbulent plasma, at small enough scales, the buoyancy effects are likely to be less important than turbulent motions (cf. Ruszkowski & Oh, 2010) — essentially because turbulent time-scales get shorter at shorter spatial scales, while the buoyancy timescale is fixed. Indeed, the typical turbulent timescale is $\tau_{\text{turb}} \sim \lambda_u/u = \lambda_u/(Mc_s)$, where u is the (subsonic) velocity of turbulent motion, M is the Mach number, c_s is the speed of sound; in contrast, the buoyancy time-scale is $\tau_{\text{buoy}} \sim \sqrt{l_{P,T}/g} \sim \sqrt{l_{P,T}l_P}/c_s$, where g is the gravitational acceleration caused by the cluster potential, l_P is the characteristic length of change of the pressure profile and l_T (in the case of MTI/HBI) is that of the macroscopic temperature profile. Therefore, $\tau_{\text{turb}} \lesssim \tau_{\text{buoy}}$ if $\lambda_u \lesssim Ml_P$ or $\lambda_u \lesssim M\sqrt{l_P l_T}$ (for MTI/HBI). Let M be ~ 0.3 . For typical cluster core parameters ($l_P \sim 100$ kpc, $l_T \sim 300$ kpc), we get $\lambda_u \lesssim 50$ kpc; for the bulk ($l_P \sim 300$ kpc, $l_T \sim 1000$ kpc), we get $\lambda_u \lesssim 200$ kpc.

Thus, our results apply at smaller spatial scales, where the turbulence time-scales are shorter than the buoyancy time-scale. Obviously, one cannot neglect stratification while

constructing a full self-consistent model of the ICM, but comparison with global cluster simulations (Section 2.4.7) suggests that accounting for buoyancy does not eliminate the phenomenon of local orthogonalization of the field lines and temperature gradients.

2.4.4 Thermal conduction

Our model requires the eddy turnover time to be smaller than the conduction time, which is quite a serious restriction. Applying the standard formula for the Spitzer thermal conduction timescale, one gets

$$\tau_{\text{cond}} \sim n_e k_B l^2 / \kappa_{\text{Sp}} \approx 3 \times 10^7 \left(\frac{n_e}{10^{-3} \text{ cm}^{-3}} \right) \left(\frac{l}{100 \text{ kpc}} \right)^2 \left(\frac{T_e}{5 \text{ KeV}} \right)^{-5/2} \text{ yr}, \quad (2.46)$$

where n_e is the electron density, T_e the electron temperature and κ_{Sp} the Spitzer thermal conductivity. At the same time,

$$\tau_{\text{turb}} \sim 5 \times 10^8 \left(\frac{\lambda_u}{100 \text{ kpc}} \right) \left(\frac{M}{0.3} \right)^{-1} \text{ yr}. \quad (2.47)$$

From this estimate, it is clear that in the cool cores, the conduction time-scale can be longer than that of the turbulence, but in the hot ($\sim 8 \text{ KeV}$) and rarefied ICM outside the core, the conduction time-scale can instead be much shorter.

Nevertheless, even outside the core the orthogonalization of the temperature gradients and field lines is likely to take place. Qualitatively, this is because the effect of the orthogonalization is to switch off conduction, i.e. effectively lengthen the conduction time-scale compared to the estimate (2.46). Thus, while gradients codirectional with field lines at some initial moment may be quickly erased by conduction, the ones that make large angles with the field lines can survive longer and, as turbulence orthogonalizes them further, conduction will become increasingly inefficient. In other words, the assumption of slow conduction will become better satisfied as the evolution proceeds. We will see that these qualitative arguments are indeed corroborated by cluster simulations with anisotropic conduction (Section 2.4.7).

2.4.5 Dynamics of the magnetic field

As shown in Section 2.3.3, the evolution of the decay rate of the small-scale ($l \lesssim \lambda_u$) temperature variations can be linked to the amount of stretching of the field lines as $\propto \langle 1/s^2 \rangle$. Essentially the decay rate goes down because the field lines, along which the heat is transported, are stretched.¹ The amount of stretching is, of course, limited by saturation of the magnetic field. This may turn out to be a key effect in the problem, but it is not analytically treatable as easily as the case of passive field considered here and is

¹The effect of the field-line stretching on the suppression of thermal conduction has previously been studied by Rosner & Tucker 1989 and Tao 1995, but in the case of $\lambda_B < \lambda_{mfp}$ and constant macroscopic thermal gradient.

best addressed with direct numerical simulations (see Section 2.4.7). Another potentially important effect we have ignored is the reconnection of the field lines, which may in principle considerably modify their topology. While we believe the simple model considered in this paper correctly captures the qualitative picture, direct numerical simulations are required to confirm this.

2.4.6 Local versus global conduction

We stress again that we have only considered the suppression of *local* thermal conduction, as applies to temperature *fluctuations* on scales $l < \lambda_u$. We have established that the gradients associated with these fluctuations are predominantly oriented perpendicular to the magnetic-field lines by the plasma flow. In general, however, if one is interested in the global heat transport on scales $l \gg \lambda_u$, other effects start to be important: in particular, exponential divergence of field lines (Rechester & Rosenbluth, 1978; Narayan & Medvedev, 2001; Chandran & Maron, 2004).

2.4.7 Comparison with global cluster simulations

To back up our qualitative arguments in support of the conclusions of our theoretical model despite the many simplifying assumptions that were required to make it solvable, we have employed the data drawn from the simulations reported by ZuHone et al. (2013). These are global dynamic MHD simulations of a disturbed cluster, which were not specifically designed to test our model but represent a current state-of-the-art numerical model of cluster evolution in response to a minor merger. The simulations incorporate all of the additional physics that we neglected and that is essential for a global model: a range of spatial and time-scales, compressibility, large-scale stratification, buoyancy, anisotropic thermal conduction, radiative cooling and dynamic back-reaction of the magnetic field on the fluid motions.

In these simulations, a massive ($M \approx 1.5 \times 10^{15} M_\odot$, $T \sim 8$ keV), cool-core cluster, initially in hydrostatic equilibrium, merged with a small (mass ratio $R = 5$) gasless sub-cluster, which set off the sloshing of the cool core. The simulation started at a point in time when the cluster centers had a mutual separation of $d = 3$ Mpc and an impact parameter $b = 500$ kpc. The initial velocities of the subclusters were set up assuming that the total kinetic energy of the system was set to half of its total potential energy. The main cluster was set up within a cubical computational domain of width $L = 2.4$ Mpc on a side, with the finest cell size on the grid of 2.34 kpc. A random magnetic field was set up in Fourier space using independent normal random deviates for the real and imaginary components of the field. The field spectrum corresponded to a Kolmogorov shape with cut-offs at large (≈ 500 kpc) and small (≈ 40 kpc) linear scales. The initial plasma β was 400. For the detailed description of these simulations, see ZuHone et al. (2013) and ZuHone et al. (2011). In the tests reported below, we only considered the central 500 kpc of the simulated cluster (Fig. 2.8), where the disturbance of the ICM was greatest, leading to significant local temperature variation and tangled magnetic field.

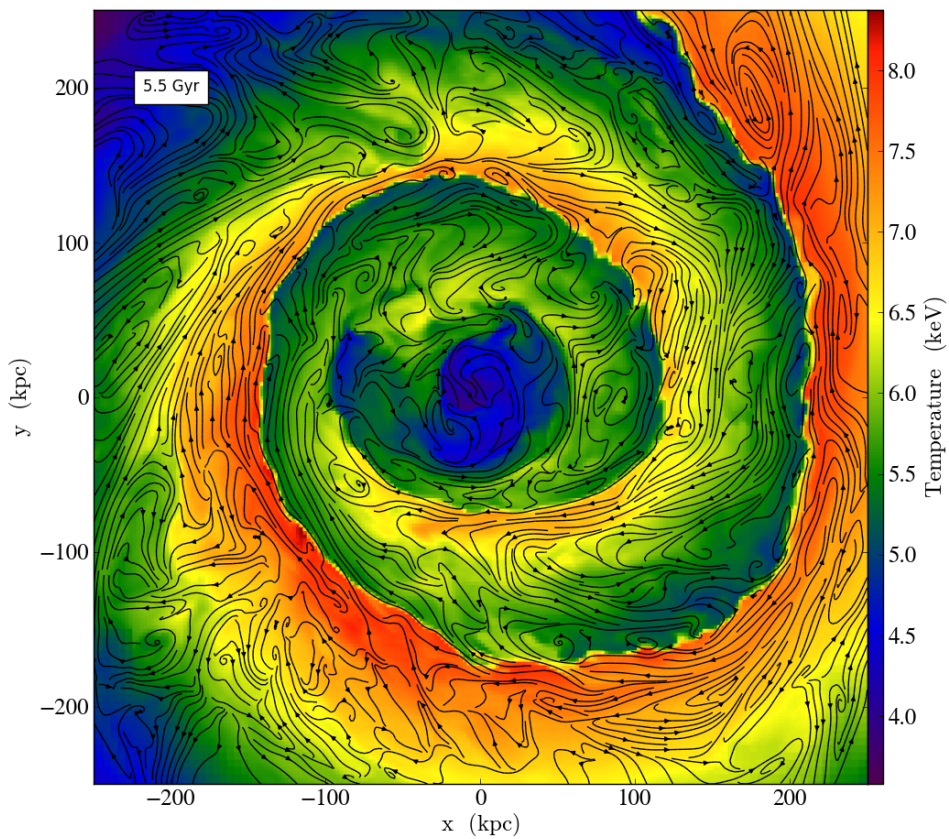


Figure 2.8: Central 500-kpc region of the simulation box of ZuHone et al. (2013) at $t = 5.5$ Gyr used for comparison of our theory with the simulations.

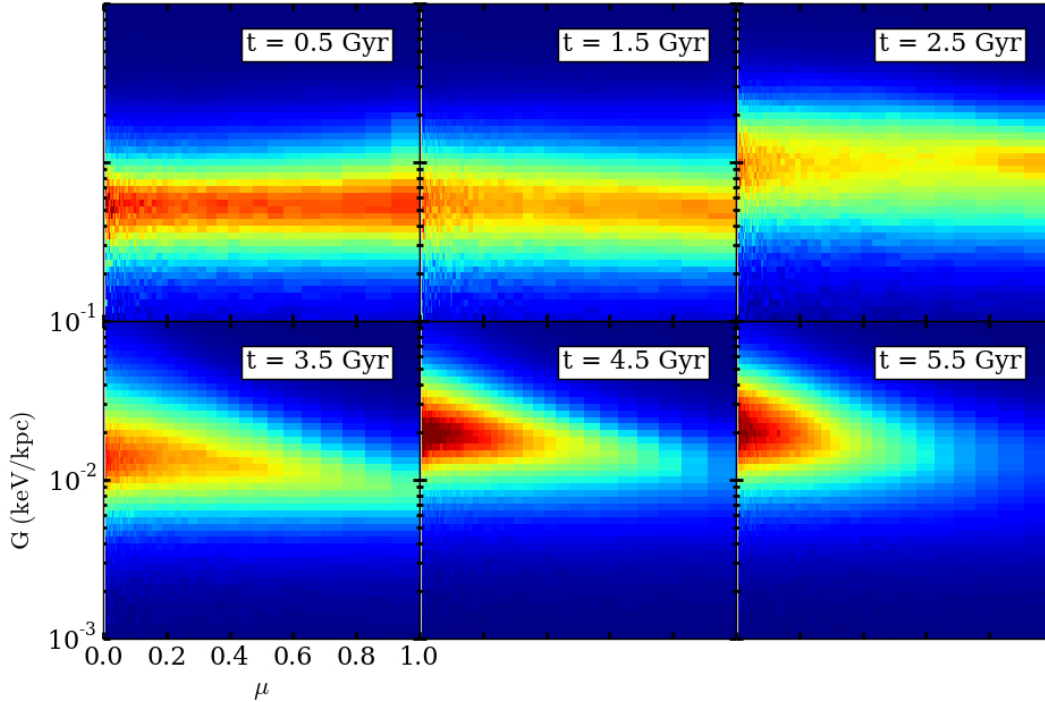


Figure 2.9: Evolution of the joint PDF of $\mu = |\mathbf{b} \cdot \nabla T|$ and $G = |\nabla T|$ for the Run S1 of ZuHone et al. (2013) – a global MHD cluster simulation with thermal conduction and radiative cooling switched off.

First, we examined a simulation with thermal conduction and radiative cooling turned off – this is the Run S1 from ZuHone et al. (2013). Fig. 2.9 shows the evolution of the joint PDF(G, μ) analogous to that shown in Fig. 2.6. Initially, the magnetic field orientation was random as indicated by the flat PDF over μ in the top left frame in Fig. 2.9. With time, the most probable value of G increased, while the corresponding μ decreased. This behavior is qualitatively very similar to the evolution of the model PDF shown in Fig. 2.6. Note that in Fig. 2.8, it is visually manifest that magnetic field lines and surfaces of constant temperature are aligned in much of the disturbed ICM, including both sharp fronts (cf. Section 2.2.2) and the more random turbulent regions.

When radiative cooling was switched on, while conduction was still off (Run SX of ZuHone et al. 2013), the behaviour of the joint PDF of G and μ was qualitatively very similar to that in pure MHD case described above, except for a small increase of the PDF at higher gradients independent of the value of μ , which is expected because cooling may generate temperature gradients from the density gradients regardless of the magnetic-field orientation.

Finally, consider a simulation identical to the ones used above but with both cooling

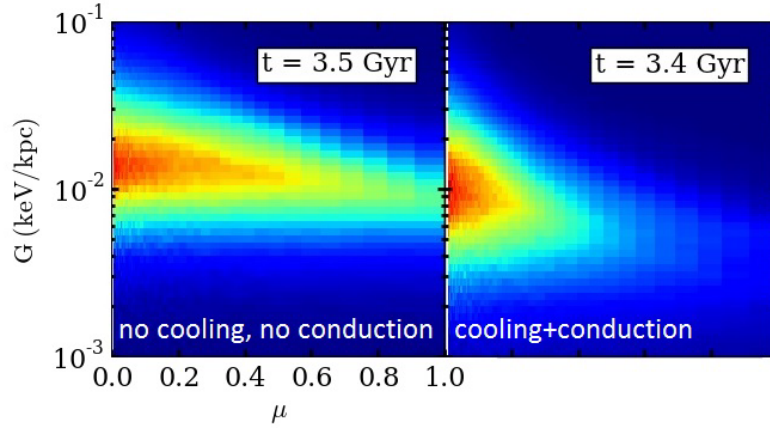


Figure 2.10: Joint PDF of G and μ in a global cluster simulations. Left panel: same case as in Fig. 2.9. Right panel: identical case except with anisotropic conduction and radiative cooling switched on (Run SCX1 of ZuHone et al. 2013).

and anisotropic conduction switched on (Run SCX1 of ZuHone et al. 2013). In Fig. 2.10, the joint PDF of G and μ for the cluster, taken at a late stage in its evolution, is contrasted to the case without conduction at a similar time. For this hot ($T \sim 8$ KeV) simulated cluster, thermal conduction was strong enough to make a non-trivial impact on the PDF. Efficient anisotropic conduction quickly eliminated small-scale thermal gradients in the regions where the field lines and the temperature gradients were aligned in the initial setup, while the gradients orthogonal to the field survived longer. This process shifted the PDF to smaller μ and lower G as compared to the case with no conduction (see Fig. 2.9). At the same time, the high gradients in the regions with small μ were preserved and enhanced on average by the gas motions. The maximum of the PDF still drifted to higher gradients and smaller μ so that high temperature gradients ended up associated with perpendicular orientation of the gradients and the field lines. Clearly, both effects (one driven by gas motions and another by anisotropic conduction) lead to a similar net result: large temperature gradients one can expect to find in the ICM are likely associated with regions where μ is small. Thus, the shape of the PDF derived from the simulation with cooling and thermal conduction is qualitatively similar to the one in the absence of cooling and thermal conduction (see Fig. 2.10). We conclude that the effect proposed in this paper is identifiable even if efficient thermal conduction smears out the initial gradients on small scales.

At last, let us stress again that these simulations were not specifically tailored for the problem at hand. For example, in our theoretical model, we assume continuous and spatially homogeneous driving with a well defined eddy turn-over time scale, while in the simulations, the cluster is perturbed at a specific time and in a special way. Also, on the numerical side, a precise evaluation of the angle between the field lines and gradients in the presence of small-scale eddies should have considerable uncertainty, precluding firm

conclusion on the behavior of the PDF at very small μ . This makes further detailed quantitative comparisons between theory and simulations problematic. A bespoke numerical study would clearly be a worthwhile undertaking and is left for the future. However, it appears that even on the basis of this limited comparison, we can conclude optimistically that the correlation between large gradients of T and small values of μ is clearly present in the numerical model, which does not suffer from the limitations of our theory and contains much of the physics currently believed to be relevant.²

2.5 Conclusions

We have studied the correlations between the local fluctuating temperature gradients and the orientation of the frozen-in magnetic-field lines in the turbulent ICM. We have argued that the mutual orientation between isotherms and magnetic-field lines is not random, but rather a strong alignment is expected: gas motions tend to increase the temperature gradients and, at the same time, align the field lines perpendicular to the gradients. Cold fronts in clusters provide a vivid example of this process on large scales. The net result of the correlated evolution of the temperature distribution and the magnetic field is the effective suppression of the local heat flux. We note that global thermal conduction defined by radial temperature profiles of galaxy clusters (which is one of the possible solutions to the cooling flow problem) is beyond the scope of this work.

We have calculated explicitly the joint distribution function of the gradients and the angles they make relative to the field lines and demonstrated that significant suppression takes place for generic 3D isotropic incompressible motions. The main conclusions are as follows:

- Strong correlation of the fluctuating temperature gradients and the local magnetic field orientation is established on the timescale of the turbulent eddy turnover.
- On average, the decay rate of temperature fluctuations is anti-correlated with the degree of amplification of the magnetic field by the gas motions. Volume averaged decay rate decreases with the growth of the magnetic-energy density as $\langle B^2 \rangle^{-1/5}$.
- For disturbed clusters, where large-scale clumps of gas are displaced, the largest observed *local* gradients should be associated with the largest heat flux suppression. The estimates of the effective conductivity based on these gradients may not be characteristic of the bulk of the gas. This conclusion appears to be supported by global dynamic cluster simulations with and without anisotropic conduction.

²Although it still takes no account of some of the plasma microphysics whose role remains poorly understood if potentially dramatic (Kunz et al., 2011; Mogavero & Schekochihin, 2013).

Acknowledgements

This work was supported in part by the Leverhulme Trust Network on Magnetized Plasma Turbulence.

2.6 Appendix: statistical calculation of the joint PDF of μ , G and B

The general form of the joint PDF of the magnetic field and the temperature gradient is

$$P(\mathbf{g}, \mathbf{b}, G, B; t) = \langle \tilde{P} \rangle, \quad (2.48)$$

$$\tilde{P} = \delta(\mathbf{g} - \mathbf{g}(t))\delta(\mathbf{b} - \mathbf{b}(t))\delta(G - G(t))\delta(B - B(t)), \quad (2.49)$$

where \mathbf{g} , \mathbf{b} , G and B are variables and $\mathbf{g}(t)$, $\mathbf{b}(t)$, $G(t)$ and $B(t)$ are stochastic processes that are solutions of equations (2.30). Taking time derivative of \tilde{P} and using equations (2.30), we obtain

$$\partial_t P = \hat{L}_i^m \sigma_m^i \tilde{P}, \quad (2.50)$$

where

$$\hat{L}_i^m = \frac{\partial}{\partial g^k} (\delta_m^k - g^k g^m) g^i - \frac{\partial}{\partial b^k} (\delta_i^k - b^k b^i) b^m + \frac{\partial}{\partial G} g^i g^m G - \frac{\partial}{\partial B} b^i b^m B. \quad (2.51)$$

The average of equation (2.50) is

$$\partial_t P = \hat{L}_i^m \langle \sigma_m^i \tilde{P} \rangle \quad (2.52)$$

and we now apply the Furutsu-Novikov formula (Furutsu, 1963; Novikov, 1965) to calculate the right-hand side:

$$\langle \sigma_m^i(t) \tilde{P}(t) \rangle = \int dt' \langle \sigma_m^i(t) \sigma_n^j(t') \rangle \left\langle \frac{\delta \tilde{P}(t)}{\delta \sigma_n^j(t')} \right\rangle = \epsilon T_{mn}^{ij} \left\langle \frac{\delta \tilde{P}(t)}{\delta \sigma_n^j(t)} \right\rangle \quad (2.53)$$

where we have used equation (2.15). From equation (2.50),

$$\frac{\delta \tilde{P}(t)}{\delta \sigma_n^j(t)} = \int_{-\infty}^t dt' \left[\hat{L}_i^m \delta_j^i \delta_m^n \delta(t-t') \tilde{P}(t') + \hat{L}_i^m \sigma_m^i(t') \frac{\delta \tilde{P}(t')}{\delta \sigma_n^j(t)} \right] = \frac{1}{2} \hat{L}_j^n \tilde{P}(t). \quad (2.54)$$

The second term inside the integral vanishes by causality ($t' < t$). Using equation (2.54) in equation (2.53) and substituting into equation (2.52), we arrive at a closed equation for the desired PDF:

$$\partial_t P = \frac{\epsilon}{2} T_{mn}^{ij} \hat{L}_i^m \hat{L}_j^n P. \quad (2.55)$$

Since the medium is isotropic, the PDF only depends on G , B and the angle between the unit vectors \mathbf{g} and \mathbf{b} . Therefore, it can be factorized as

$$P(\mathbf{g}, \mathbf{b}, G, B; t) = \frac{1}{8\pi^2} \delta(\mathbf{g}^2 - 1) \delta(\mathbf{b}^2 - 1) p(\mu, G, B; t), \quad (2.56)$$

where $\mu = \mathbf{b} \cdot \mathbf{g}$. The factor $1/8\pi^2$ has been introduced in order to keep $p(\mu, G, B; t)$ normalized to unity. Substituting this expression into equation (2.55), we get

$$\begin{aligned}
\hat{L}_i^m \hat{L}_j^n P = & \delta(\mathbf{g}^2 - 1)\delta(\mathbf{b}^2 - 1)\{(b^i b^j b^m b^n + g^i g^j g^m g^n - g^i b^j g^m b^n - b^i g^j b^m g^n)\mu\partial_\mu\mu\partial_\mu \\
& + (b^i g^j b^m g^n - g^i g^j g^m g^n)\mu\partial_\mu\partial_G G + (g^i b^j g^m b^n - 2b^i b^j b^m b^n + b^i g^j b^m g^n)\mu\partial_\mu\partial_B B \\
& - (g^i b^j g^m b^n + b^i g^j b^m g^n)\partial_G G\partial_B B + g^i g^j g^m g^n \partial_G G\partial_G G \\
& + [2(D+1)(b^i b^j b^m b^n + g^i g^j g^m g^n) - 2D(g^i b^j g^m b^n + b^i g^j b^m g^n) \\
& - b^m b^n \delta_j^i - b^j b^m \delta_n^i - g^i g^n \delta_m^j - g^i g^j \delta_n^m]\mu\partial_\mu \\
& + [-2(D+1)g^i g^j g^m g^n + D(g^i b^j g^m b^n + b^i g^j b^m g^n) + g^i g^n \delta_m^j + g^i g^j \delta_n^m]\partial_G G \\
& + [-2(D+1)b^i b^j b^m b^n + Dg^i b^j g^m b^n + Db^i g^j b^m g^n + b^m b^n \delta_j^i + b^j b^m \delta_m^j]\partial_B B \\
& + D[(D+2)(b^i b^j b^m b^n + g^i g^j g^m g^n) - D(g^i b^j g^m b^n + b^i g^j b^m g^n) \\
& - (b^m b^n \delta_j^i + b^j b^m \delta_n^i + g^i g^n \delta_m^j + g^i g^j \delta_n^m)]\}p, \tag{2.57}
\end{aligned}$$

where D is the number of spatial dimensions. The PDF is factorized, as it ought to be, and we only need to solve the equation for $p(\mu, G, B; t)$. Substituting equation (2.57) into equation (2.55), we perform the convolutions involving T_{mn}^{ij} [see equation (2.16)] using the identities

$$\begin{aligned}
T_{mn}^{ij} b^i b^j b^m b^n &= \frac{D-1}{D+1}, \\
T_{mn}^{ij} g^i b^j g^m b^n &= \frac{\mu^2 - 1}{D+1}, \\
T_{mn}^{ij} b^j b^m \delta_n^i &= 0, \\
T_{mn}^{ij} b^m b^n \delta_j^i &= \frac{(D-1)(D+2)}{D+1}, \\
T_{mn}^{ij} b^i g^j b^m g^n &= \frac{\mu^2 - 1}{D+1}, \\
T_{mn}^{ij} g^i g^j g^m g^n &= \frac{D-1}{D+1}, \\
T_{mn}^{ij} g^i g^n \delta_m^j &= 0, \\
T_{mn}^{ij} g^i g^j \delta_n^m &= \frac{(D-1)(D-2)}{D+1}. \tag{2.58}
\end{aligned}$$

The result is equation (2.31).

Bibliography

- Albright B. J., Chandran B. D. G., Cowley S. C., Loh M., 2001, *Phys. Plasmas*, 8, 777
- Asai N., Fukuda N., Matsumoto R., 2007, *ApJ*, 663, 816
- Balbus S. A., 2000, *ApJ*, 534, 420
- Balkovsky E., Fouxon A., 1999, *Phys. Rev. E*, 60, 4164
- Bogdanović T., Reynolds C. S., Balbus S. A., Parrish I. J., 2009, *ApJ*, 704, 211
- Boldyrev S., Cattaneo F., 2004, *Phys. Rev. Lett.*, 92, 144501
- Boldyrev S. A., Schekochihin A. A., 2000, *Phys. Rev. E*, 62, 545
- Braginskii S. I., 1965, *Rev. Plasma Phys.*, 1, 205
- Chandran B. D. G., Cowley S. C., 1998, *Phys. Rev. Lett.*, 80, 3077
- Chandran B. D. G., Cowley S. C., Ivanushkina M., Sydora R., 1999, *ApJ*, 525, 638
- Chandran B. D. G., Maron J. L., 2004, *ApJ*, 602, 170
- Chertkov M., Falkovich G., Kolokolov I., Vergassola M., 1999, *Phys. Rev. Lett.*, 83, 4065
- Churazov E., Forman W., Vikhlinin A., Tremaine S., Gerhard O., Jones C., 2008, *MNRAS*, 388, 1062
- Churazov E., Inogamov N., 2004, *MNRAS*, 350, L52
- Churazov E., Vikhlinin A., Zhuravleva I., Schekochihin A., Parrish I., Sunyaev R., Forman W., Böhringer H., Randall S., 2012, *MNRAS*, 421, 1123
- Ettori S., Fabian A. C., 2000, *MNRAS*, 317, L57
- Furutsu K., 1963, *J. Res. NBS*, 67D, 303
- Inogamov N. A., Sunyaev R. A., 2003, *Astron. Lett.*, 29, 791
- Kazantsev A. P., 1968, *Soviet Phys. JETP*, 26, 1031

- Kunz M. W., Bogdanović T., Reynolds C. S., Stone J. M., 2012, *ApJ*, 754, 122
- Kunz M. W., Schekochihin A. A., Cowley S. C., Binney J. J., Sanders J. S., 2011, *MNRAS*, 410, 2446
- Lau E. T., Kravtsov A. V., Nagai D., 2009, *ApJ*, 705, 1129
- Lyutikov M., 2006, *MNRAS*, 373, 73
- Malyshev L., Kulsrud R., 2001, *ApJ*, 549, 402
- Markevitch M., Mazzotta P., Vikhlinin A., Burke D., Butt Y., David L., Donnelly H., Forman W. R., Harris D., Kim D.-W., Virani S., Vrtilik J., 2003, *ApJ*, 586, L19
- Markevitch M., Vikhlinin A., 2007, *Phys. Rep.*, 443, 1
- McCourt M., Parrish I. J., Sharma P., Quataert E., 2011, *MNRAS*, 413, 1295
- Mogavero F., Schekochihin A. A., 2013, *ArXiv*: 1312.3672
- Narayan R., Medvedev M. V., 2001, *ApJ*, 562, L129
- Novikov E., 1965, *Soviet Phys. JETP*, 20, 1290
- Parrish I. J., Quataert E., Sharma P., 2009, *ApJ*, 703, 96
- Quataert E., 2008, *ApJ*, 673, 758
- Rechester A. B., Rosenbluth M. N., 1978, *Phys. Rev. Lett.*, 40, 38
- Roediger E., Brüggem M., Simionescu A., Böhringer H., Churazov E., Forman W. R., 2011, *MNRAS*, 413, 2057
- Rosner R., Tucker W. H., 1989, *ApJ*, 338, 761
- Ruszkowski M., Lee D., Brüggem M., Parrish I., Oh S. P., 2011, *ApJ*, 740, 81
- Ruszkowski M., Oh S. P., 2010, *ApJ*, 713, 1332
- Schekochihin A., Cowley S., Maron J., Malyshev L., 2002, *Phys. Rev. E*, 65, 016305
- Schekochihin A. A., Cowley S. C., 2006, *Phys. Plasmas*, 13, 056501
- Schekochihin A. A., Cowley S. C., Taylor S. F., Maron J. L., McWilliams J. C., 2004, *ApJ*, 612, 276
- Schekochihin A. A., Haynes P. H., Cowley S. C., 2004, *Phys. Rev. E*, 70, 046304
- Schuecker P., Finoguenov A., Miniati F., Böhringer H., Briel U. G., 2004, *A&A*, 426, 387

Sharma P., Chandran B. D. G., Quataert E., Parrish I. J., 2009, *ApJ*, 699, 348

Skilling J., McIvor I., Holmes J. A., 1974, *MNRAS*, 167, 87P

Subramanian K., Shukurov A., Haugen N. E. L., 2006, *MNRAS*, 366, 1437

Tao L., 1995, *MNRAS*, 275, 965

Vikhlinin A., Markevitch M., Murray S. S., 2001, *ApJ*, 549, L47

Xiang F., Churazov E., Dolag K., Springel V., Vikhlinin A., 2007, *MNRAS*, 379, 1325

Zhuravleva I. V., Churazov E. M., Sazonov S. Y., Sunyaev R. A., Dolag K., 2011, *Astron. Lett.*, 37, 141

ZuHone J. A., Markevitch M., Lee D., 2011, *ApJ*, 743, 16

ZuHone J. A., Markevitch M., Ruszkowski M., Lee D., 2013, *ApJ*, 762, 69

Chapter 3

Conduction in a mirror-unstable plasma

MNRAS, 2016, 460, 467

S. V. Komarov, E. M. Churazov, M. W. Kunz and A. A. Schekochihin

Abstract. The plasma of galaxy clusters is subject to firehose and mirror instabilities at scales of order the ion Larmor radius. The mirror instability generates fluctuations of magnetic-field strength $\delta B/B \sim 1$. These fluctuations act as magnetic traps for the heat-conducting electrons, suppressing their transport. We calculate the effective parallel thermal conductivity in the intracluster medium (ICM) in the presence of the mirror fluctuations for different stages of the evolution of the instability. The mirror fluctuations are limited in amplitude by the maximum and minimum values of the field strength, with no large deviations from the mean value. This key property leads to a finite suppression of thermal conduction at large scales. We find suppression down to ≈ 0.2 of the Spitzer value for the secular phase of the perturbations' growth, and ≈ 0.3 for their saturated phase. The effect operates in addition to other suppression mechanisms and independently of them. Globally, fluctuations $\delta B/B \sim 1$ can be present on much larger scales, of the order of the scale of turbulent motions. However, we do not expect large suppression of thermal conduction by these, because their scale is considerably larger than the collisional mean free path of the ICM electrons. The obtained suppression of thermal conduction by a factor of ~ 5 appears to be characteristic and potentially universal for a weakly collisional mirror-unstable plasma.

3.1 Introduction

Thermal conduction in a magnetized plasma is a long-standing problem in astrophysics, dating back to the realization that virtually all astrophysical plasmas possess magnetic fields (based on both theoretical considerations and observations of synchrotron emission

and the Faraday rotation). Although these fields are relatively weak ($\sim 1 - 10 \mu\text{G}$ in the bulk of the ICM, see, e.g., Carilli & Taylor 2002 or Feretti et al. 2012 for reviews), they constrain the motion of charged particles to spiraling along the field lines with Larmor radii typically very small compared to other physically relevant scales, namely, to the collisional mean free path and the correlation length of the plasma flows. In such a plasma, the electrons predominantly transfer heat along the field lines.

In the ICM, the quest for a theory of effective heat conductivity is strongly motivated by the observations of apparently long-lived temperature substructures (e.g., Markevitch et al., 2003) and sharp gradients (cold fronts; e.g., Markevitch et al. 2000; Ettore & Fabian 2000; Vikhlinin et al. 2001; Markevitch & Vikhlinin 2007) that would not have survived had the electron conductivity been determined by the classic Spitzer expression for an unmagnetized plasma (Spitzer, 1962). Another puzzling topic is the stability of cluster cool cores, in which the role of thermal conduction is still unclear (e.g., Ruszkowski & Begelman, 2002; Zakamska & Narayan, 2003; Voigt & Fabian, 2004; Dennis & Chandran, 2005).

The general problem of thermal conduction in an astrophysical plasma is greatly complicated by the fact that the medium is likely turbulent (for the ICM, see, e.g., Inogamov & Sunyaev 2003; Schuecker et al. 2004; Schekochihin & Cowley 2006; Subramanian et al. 2006; Zhuravleva et al. 2014), and so the magnetic-field lines are randomly tangled. It is practical to subdivide the problem into more narrowly formulated questions and study them separately. First, parallel conduction in a static magnetic field of a given structure can be investigated (e.g., Chandran & Cowley, 1998). The static approximation is reasonable because electrons stream along magnetic fields faster than these fields are evolved by turbulence. Next, one can study the effective boost of the transverse conduction across the field lines due to their exponential divergence (Skilling et al., 1974; Rechester & Rosenbluth, 1978; Chandran & Cowley, 1998; Narayan & Medvedev, 2001; Malyshkin, 2001; Chandran & Maron, 2004). Finally, local heat fluxes at the scale of turbulent eddies are affected by the correlation between temperature gradients and the magnetic field as they evolve in the same turbulent velocity field (Komarov et al. 2014; this process occurs on longer time scales than the other two). In this chapter, we only address the first part of the problem, parallel thermal conduction, as applied to the ICM.

Parallel conduction can be affected by magnetic trapping of electrons by fluctuations of the field strength along a field line (Klepach & Ptuskin, 1995; Chandran & Cowley, 1998; Chandran et al., 1999; Malyshkin & Kulsrud, 2001; Albright et al., 2001). These fluctuations might be produced by various mechanisms. At the scale of turbulent motions, they can be generated by the small-scale turbulent MHD dynamo as a result of a series of random stretchings and compressions by the velocity field (e.g., Schekochihin et al., 2002, 2004; Schekochihin & Cowley, 2006, and references therein). At microscales of the order of the ion Larmor radius, the ICM plasma is subject to kinetic instabilities (Schekochihin et al., 2005; Schekochihin & Cowley, 2006). As the ion Larmor radius is many orders of magnitude smaller than the collisional mean free path, the plasma is weakly collisional, which results in conservation of adiabatic invariants, the first of them being the magnetic moment of a particle $\mu = v_{\perp}^2/(2B)$, where v_{\perp} is the component of the particle velocity

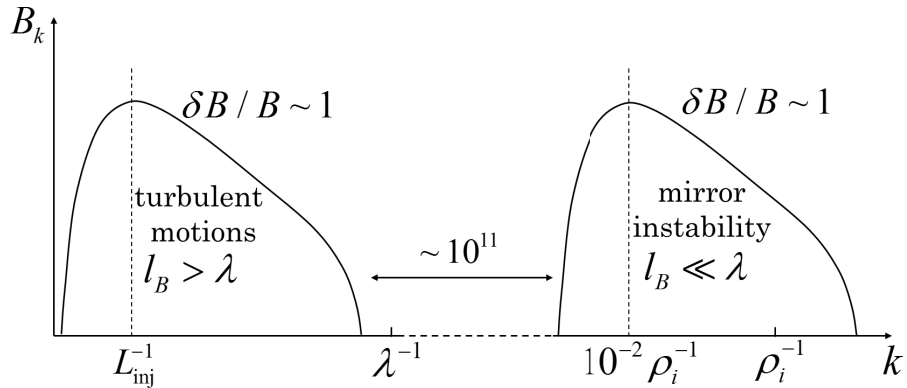


Figure 3.1: A sketch of the spectrum of the fluctuations of magnetic-field strength in the ICM. The perturbations $\delta B/B \sim 1$ (relevant for magnetic trapping) generated by turbulence occupy the region $\lambda \lesssim l_B$, where magnetic trapping is ineffective. The mirror fluctuations, in contrast, are at the scales comparable to the ion Larmor radius ρ_i , $\lambda \sim 10^{13} \rho_i$, where magnetic mirrors can suppress electron transport considerably.

perpendicular to the magnetic field. Consequently, the magnetic-field strength changes are correlated with changes in the perpendicular pressure, giving rise to pressure anisotropy. In turn, pressure anisotropy triggers firehose and mirror instabilities (Chandrasekhar et al., 1958; Parker, 1958; Hasegawa, 1969) that hold the degree of anisotropy $\Delta = (p_{\perp} - p_{\parallel})/p_{\perp}$ at marginal levels $|\Delta| \sim 1/\beta$, where β is the plasma beta, the ratio of thermal to magnetic energy density (for observational evidence in the solar wind, see Kasper et al. 2002; Hellinger et al. 2006; Bale et al. 2009; for theoretical discussion of possible mechanisms of maintaining marginality, see Melville et al. 2016 and references therein). The firehose instability occurs when $\Delta < -2/\beta$, which happens in regions where the field strength is decreasing, near the reversal points of the field lines, and typically generates small ($\delta B_{\perp}/B \ll 1$) transverse Alfvénic fluctuations of the field direction. The mirror instability (or the ‘mirror mode’) is a resonant instability set off when $\Delta > 1/\beta$, which is the case where the field is amplified along the stretches of the field lines. The mirror mode produces fluctuations of magnetic-field strength of order unity ($\delta B/B \sim 1$), which form magnetic traps and may, in principle, inhibit electron transport along the field lines. While field-strength fluctuations $\delta B/B \sim 1$ can also be generated by turbulent motions, we will argue in Section 3.4 that the resulting suppression of transport is very moderate, because the electron mean free path λ is smaller than the parallel correlation length of the magnetic field l_B , and the electrons can escape from magnetic traps relatively easily. Illustratively, the presumed combined spectrum of magnetic-field strength fluctuations in the ICM is sketched in Fig. 3.1: the magnetic mirrors capable of efficient suppression of electron transport reside in the region $\lambda \gg l_B$.

The mirror magnetic fluctuations are impossible to observe directly in the ICM due to their extremely small scales, but they can be modeled by numerical simulations. The recent

hybrid particle-in-cell simulations of the firehose and mirror instabilities in a shearing box done by Kunz et al. (2014) suit this task well in providing the typical statistical properties of the magnetic mirror fluctuations. In this paper, we use the mirror fluctuations produced by their simulations to model the electron motion along the resulting perturbed field lines and estimate the conductivity.

The chapter is organized as follows. In Section 3.2, we describe a model for parallel electron diffusion and its Monte Carlo equivalent for numerical calculations. Then, in Section 3.3, we apply this model to the mirror magnetic fluctuations taken from the simulations of Kunz et al. (2014) to infer the suppression of parallel electron diffusivity (Section 3.3.2) and thermal conductivity (Section 3.3.3). Next, in Section 3.4, we argue that large-scale turbulent magnetic fluctuations in the ICM, modeled by an isotropic MHD simulation, do not cause a sizable suppression. Finally, in Section 3.5, we summarize our results and their relevance to the problem of thermal conduction in the ICM and in turbulent weakly collisional plasmas in general.

3.2 A model for parallel electron diffusion in a static magnetic field

For our calculations, we assume the electron diffusion timescale to be smaller than the characteristic times of fluid motions and of the magnetic-field evolution, so that the magnetic field can be viewed as static. We will assess the validity of this assumption in Section 3.5.

If magnetic fluctuations occur at parallel scales l_B much larger than the electron Larmor radius ρ_e , which is indeed true for turbulent magnetic fluctuations, as well as for the mirror-mode perturbations produced at the scale of $1 - 100 \rho_i$, where $\rho_i = (m_i/m_e)^{1/2} \rho_e \sim 40 \rho_e$ is the ion Larmor radius, and if all fluid motions are neglected, we may use the drift-kinetic equation

$$\frac{\partial f}{\partial t} + v\xi\nabla_{\parallel}f - \frac{\nabla_{\parallel}B}{B}v\frac{1-\xi^2}{2}\frac{\partial f}{\partial\xi} = \nu(v)\frac{\partial}{\partial\xi}\frac{1-\xi^2}{2}\frac{\partial f}{\partial\xi}, \quad (3.1)$$

to evolve the electron distribution function $f = f(t, \mathbf{x}, v, \xi)$ (Kulsrud, 1964). Here $\nabla_{\parallel} = \hat{\mathbf{b}} \cdot \nabla$ is the derivative taken along the local magnetic field and $\xi = \hat{\mathbf{b}} \cdot \mathbf{v}/v = \cos\theta$, where θ is the pitch angle. The unit vector $\hat{\mathbf{b}} = \mathbf{B}/B$ points in the local magnetic-field direction. The last term on the left-hand side of equation (3.1) represents the mirror force, which guarantees conservation of the magnetic moment $\mu = v_{\perp}^2/(2B) = v^2(1-\xi^2)/(2B)$ in the absence of collisions. Isotropic collisions with collision frequency ν are described by the Lorentz pitch-angle scattering operator on the right-hand side of equation (3.1). In this section, we restrict our analysis to monoenergetic electrons, so there is no energy exchange between the particles. We also neglect the electric field because, close to marginal stability ($\Delta \sim 1/\beta$), the mirror instability generates an electric field of order $E_{\parallel} \sim (T/e)(\nabla_{\parallel}B/B)(1/\beta)$, where T is the electron temperature, e the absolute electron charge. In astrophysical plasmas, β is typically large (e.g., ~ 100 in the ICM), so the electric field can be safely neglected.

The problem is effectively one-dimensional with respect to the arc length ℓ along a field line, because all spatial derivatives in equation (3.1) are taken along the local magnetic field. Thus, we can rewrite equation (3.1) in field-aligned coordinates by normalizing the distribution function using the Jacobian of this coordinate transformation, $\tilde{f}(t, \ell, \xi) = f/B$:

$$\frac{\partial \tilde{f}}{\partial t} + \xi \frac{\partial \tilde{f}}{\partial \ell} - M(\ell) \frac{\partial}{\partial \xi} \frac{1 - \xi^2}{2} \tilde{f} = \frac{1}{\lambda} \frac{\partial}{\partial \xi} \frac{1 - \xi^2}{2} \frac{\partial \tilde{f}}{\partial \xi}, \quad (3.2)$$

where $M(\ell) = \partial \ln B / \partial \ell$ is the mirror force, $\lambda = v/\nu$ is the electron mean free path¹, and time has been rescaled as $vt \rightarrow t$. Using $\xi = \cos \theta$, the distribution function $F(t, \ell, \theta) = \tilde{f} \sin \theta$ satisfies

$$\frac{\partial F}{\partial t} + \cos \theta \frac{\partial F}{\partial \ell} + \frac{\partial}{\partial \theta} \left[\frac{1}{2} M(\ell) \sin \theta + \frac{\cot \theta}{2\lambda} \right] F = \frac{1}{2\lambda} \frac{\partial^2 F}{\partial \theta^2}. \quad (3.3)$$

A convenient way to solve this equation by the Monte Carlo method is to treat it as the Fokker-Planck equation for particles whose equations of motions are

$$\begin{aligned} \dot{\ell} &= \cos \theta, \\ \dot{\theta} &= \frac{1}{2} M(\ell) \sin \theta + \frac{\cot \theta}{2\lambda} + \frac{1}{\sqrt{\lambda}} \eta(t), \end{aligned} \quad (3.4)$$

where $\eta(t)$ is a unit Gaussian white noise, $\langle \eta(t) \eta(t') \rangle = \delta(t - t')$. As clearly seen from these equations, a particle experiences the mirror force $M(\ell)$ defined by the static magnetic field and isotropizing collisions represented by the last two terms on the right-hand side. Equations (3.4) can be easily solved numerically.

Without collisions, only the particles in the loss cone defined by $|\xi| > (1 - 2\mu B/v^2)^{1/2}$ can travel freely. The rest are reflected by regions of strong field (magnetic mirrors). Collisions allow trapped particles to get scattered into the loss cone and escape from magnetic traps. Oppositely, a free particle can be knocked out of the loss cone by collisions and become trapped. The key parameter that defines the regime of diffusion is the ratio of the collisional mean free path λ to the parallel correlation length of the magnetic field l_B . If $\lambda/l_B \ll 1$, collisions make magnetic trapping ineffective, and the electrons undergo ordinary diffusion with diffusion coefficient $D \sim \lambda v$. In the opposite limit $\lambda/l_B \gg 1$, collisions are very rare, so the pitch angle changes only slightly over the correlation length of the field. In this regime, the suppression of diffusion is greatest because a certain fraction of the particles is trapped and, in addition, the passing particles have their mean free paths effectively reduced as small-angle collisions cause leakage from the loss cone so that a free particle travels only a fraction of its mean free path before it is scattered out of the loss cone and becomes trapped (Chandran & Cowley, 1998; Chandran et al., 1999).

¹Electron collisionality may be anomalous due to, e.g., scattering off magnetic fluctuations generated by electron microinstabilities. This could reduce the effective electron mean free path, but our main results would remain valid as long as the effective mean free path is much larger than the ion Larmor scale.

3.3 Electron diffusion in a magnetic mirror field

3.3.1 Properties of the mirror field

A description of the numerical code and set-up used to generate the mirror magnetic fluctuations can be found in Kunz et al. (2014). The code (Kunz et al. 2014a) is a hybrid-kinetic particle-in-cell code, in which the electrons are fluid while the ions are treated kinetically as quasi-particles. To trigger the mirror instability, a square 2D region of plasma of spatial extent $L = 1152d_{i0}$, where d_{i0} is the initial ion skin depth, is threaded by a magnetic field directed at an angle to the y -direction and subjected to a linear shear $\mathbf{u}_0 = -Sx\hat{\mathbf{y}}$, which stretches the field lines and, by adiabatic invariance, produces pressure anisotropy. The initial magnetic field strength is B_0 , the initial plasma beta of the ions is taken to be $\beta_0 = 200$, and the shear is $S = 3 \times 10^{-4}\Omega_i$, where Ω_i is the ion gyrofrequency. The ion Larmor radius is $\rho_i = \sqrt{\beta}d_i$. Once the (ion) pressure anisotropy $\Delta = p_\perp/p_\parallel - 1$ reaches $1/\beta$, the plasma becomes mirror-unstable. Magnetic perturbations grow exponentially until they become large enough to drive the anisotropy back to the marginal level, $\Delta \rightarrow 1/\beta$. Persistent large-scale driving of the pressure anisotropy, coupled with the requirement for the plasma to remain marginally stable, leads to a long phase of secular growth of the mirror perturbations. The spatial structure of the perturbations during this phase is shown in Fig. 3.2. The mirror fluctuations are elongated in the direction of the mean magnetic field and have $\delta B_\parallel \gg \delta B_\perp$. During this secular phase, the field grows as $\delta B \propto t^{4/3}$ and the dominant modes shift towards longer wavelengths ($k_\parallel\rho_i \sim 10^{-2}$) as the pressure anisotropy asymptotically approaches marginal stability. The marginal stability is achieved and maintained during the secular phase by the trapping of ions in magnetic mirrors (see Rincon et al., 2016; Melville et al., 2016). The final saturation sets in when $\delta B/B_0 \sim 1$ at $St \gtrsim 1$, and is caused by the enhanced scattering of ions off sharp ($\delta B_\parallel/B_0 \sim 1$, $k_\parallel\rho_i \sim 1$) bends in the magnetic field at the edges of the mirrors.

We note that the electrons in the code are isothermal with $T_e = T_i$, so we are not attempting to solve the problem of the electron heat transfer self-consistently (no thermal gradients and heat fluxes are present). We have extracted two representative magnetic-field lines from the simulation domain, one during the secular phase ($St = 1$), and one during the saturated phase ($St \approx 1.8$). Each of these crosses the box eight times (note that, although the box is shearing-periodic, a field line does not bite its tail and hence can be followed over several crossings) and has a length of $\approx 18000d_{i0}$ (we adopt d_{i0} as our unit of length because d_i is practically constant in time, while ρ_i is a function of the field strength). The variation of the magnetic-field strength B along the lines is shown in Fig. 3.3. From the analysis of the probability density functions (PDF) of B for the two field lines (Fig. 3.4), it is clear that in both cases, the PDFs have abrupt cut-offs at large $B \sim$ several B_0 , as well as at small B . Therefore, the field is bounded with no large deviations from the mean value, in contrast to, e.g., a lognormal stochastic magnetic field with the same rms (shown by the dotted line in Fig. 3.4 for comparison) with a tail in its PDF, for which there is always a non-zero probability to find a large deviation at a large enough scale. This also means that the extracted field lines fully represent the statistics

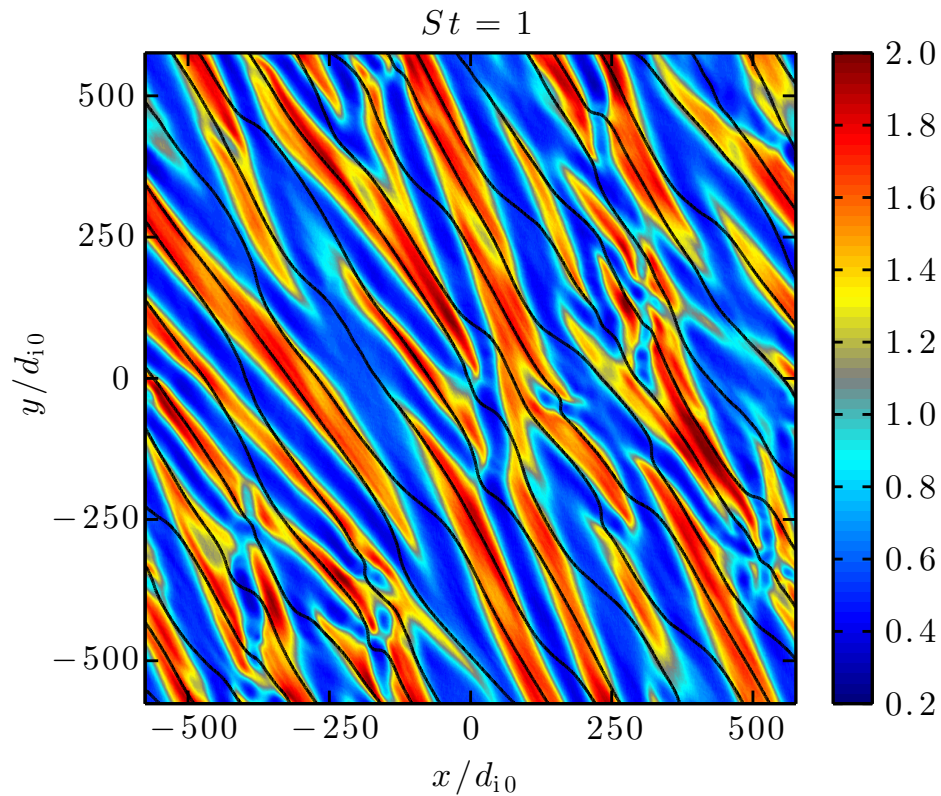


Figure 3.2: Spatial structure of the mirror instability (Kunz et al., 2014) during the secular phase of the perturbations' growth, after one shear time. The magnetic-field strength $B/\langle B \rangle$ is shown by color, the field lines are shown by contours. Length is in the units of the ion skin depth $d_{i0} = \rho_i(St = 0)/\sqrt{\beta_0}$. At time $St = 1$, the ion Larmor radius is $\rho_i \approx 8.7d_{i0}$.

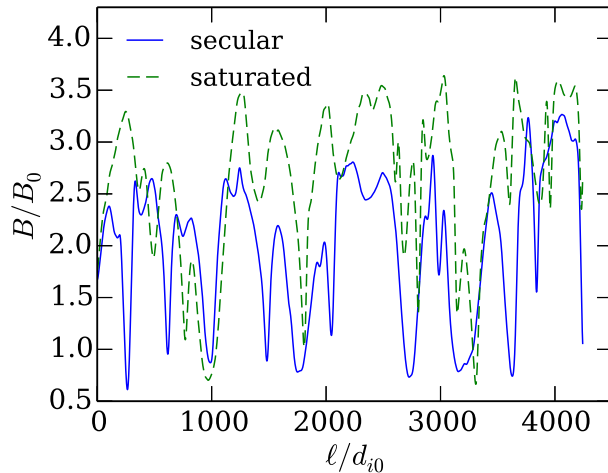


Figure 3.3: Variation of the magnetic-field strength along a field line during the two different phases of evolution of the mirror fluctuations (*solid*: secularly growing fluctuations at time $St = 1$; *dashed*: saturated fluctuations at time $St \approx 1.8$). B_0 is the initial magnetic-field strength in the simulation. For convenience, 4000- d_{i0} line segments are shown. The ion Larmor radii are $\rho_i(St = 1) \approx 8.7d_{i0}$ and $\rho_i(St \approx 1.8) \approx 6.2d_{i0}$.

of B (a longer field line would not contain more statistical information). The bounded PDF(B) is a key property of the mirror magnetic field, which leads to a finite value of suppression of electron transport at large λ/l_B , unlike in the case of stochastic magnetic fields (lognormal, Gaussian, exponential) that can completely inhibit particle transport in this limit (Mal'yskin & Kulsrud, 2001; Albright et al., 2001).

3.3.2 Electron diffusivity in the limit $\lambda/l_B \gg 1$

Results of the Monte Carlo simulations

For the two extracted field lines, we integrate the particles' trajectories defined by equations (3.4) numerically. Initially, the particle distribution is isotropic with the particle density along a field line set to $\propto 1/B$, which is a uniform density distribution in real space [recall the Jacobian of the coordinate transformation to field-aligned coordinates in equation (3.2)]. Then we trace the evolution of the particles over time $t_1 = 20 t_{\text{coll}}$, where $t_{\text{coll}} = 1/\nu$ is the collision time. The monoenergetic diffusion coefficient D is calculated as

$$D = \frac{\langle [\ell_i(t_1) - \ell_i(t_0)]^2 \rangle}{2(t_1 - t_0)}, \quad (3.5)$$

where ℓ_i are the particles' displacements. We choose $t_0 = 5 t_{\text{coll}}$ in order to allow the particles to collide a few times until the ballistic regime gives way to diffusion at $t \gtrsim$

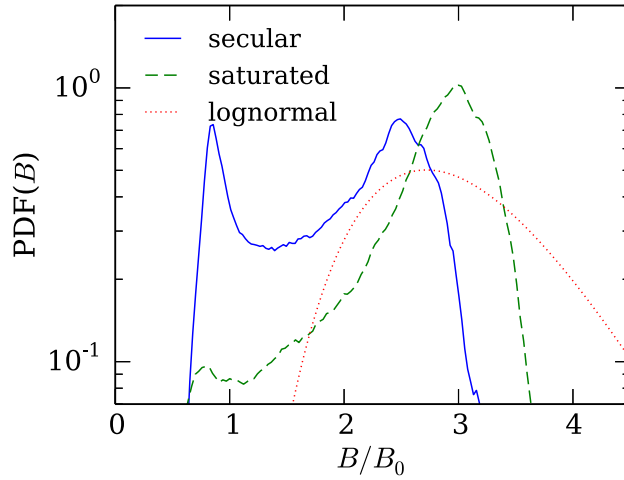


Figure 3.4: PDFs of the magnetic-field-strength fluctuations generated by the mirror instability. A lognormal distribution with rms equal to the rms of the logarithm of the saturated mirror fluctuations is shown by the dotted line for comparison.

t_{coll} . The same procedure is carried out for several different ratios λ/l_B in the range $2 \times 10^{-4} - 5 \times 10^4$. The correlation lengths of the field strength along the lines are $l_B \approx 850d_{i0} \approx 100\rho_i (St = 1)$ for the secular phase and $l_B \approx 1430d_{i0} \approx 230\rho_i (St \approx 1.8)$ for the saturated phase.

Defining $D_0 = (1/3)\lambda v$, the diffusion coefficient in the absence of the magnetic fields, we thus obtain the monoenergetic diffusion suppression factor $S_D = D/D_0$ as a function of λ/l_B (Fig. 3.5). Averaging the monoenergetic diffusivity D over a thermal distribution of the electron speeds v introduces only a slight change in the shape of the function $S_D(\lambda/l_B)$, so we only present the monoenergetic diffusion suppression in what follows.

For magnetic mirror fluctuations in the ICM, the limit $\lambda/l_B \gg 1$ is the relevant one, because the ion Larmor radius is many orders of magnitude smaller than the mean free path:

$$\lambda \approx 20 \text{ kpc} \left(\frac{T}{8 \text{ KeV}} \right)^2 \left(\frac{n}{10^{-3} \text{ cm}^{-3}} \right)^{-1}, \quad (3.6)$$

$$\rho_i \approx 5 \times 10^{-12} \text{ kpc} \left(\frac{T}{8 \text{ KeV}} \right)^{1/2} \left(\frac{B}{1 \mu\text{G}} \right)^{-1}. \quad (3.7)$$

In this limit, the suppression factor asymptotically approaches $S_D \approx 0.12$ during the secular phase, and $S_D \approx 0.19$ for the saturated mirrors. The absence of the mean-free-path dependence at large λ/l_B is due to the fact that the mirror fluctuations are bounded, as we have seen by analyzing their PDF (Fig. 3.4). This is very different from the case of stochastic magnetic mirrors (see Malyshkin & Kulsrud 2001; we will discuss stochastic magnetic mirrors in more detail in Section 3.4.1).

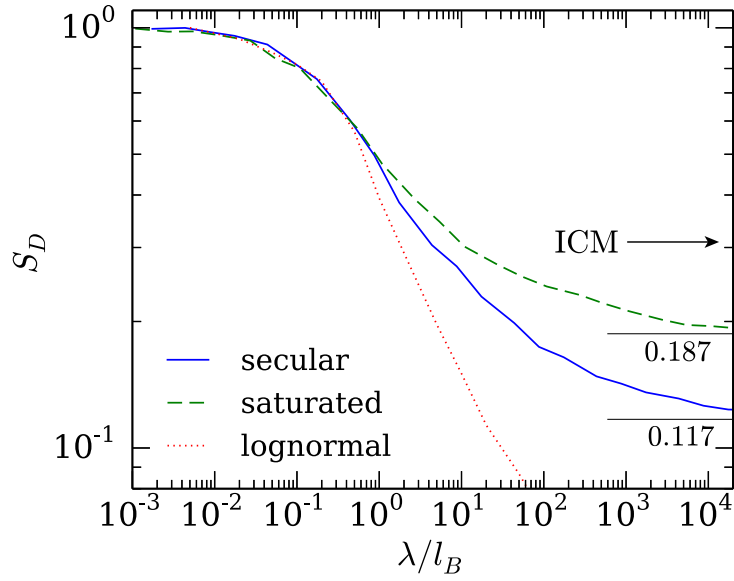


Figure 3.5: Suppression factor of the electron diffusivity $S_D = D/D_0$ in the secularly growing (solid line) and saturated (dashed line) magnetic mirror fluctuations. The correlation lengths of the field strength along the field lines are $l_B \approx 850d_{i0} \approx 100\rho_i(St = 1)$ during the secular phase and $l_B \approx 1430d_{i0} \approx 230\rho_i(St \approx 1.8)$ for the saturated mirrors. For comparison, the dotted line shows suppression in a synthetic lognormal magnetic field with the same rms value of $\log B$ as during the phase of secular growth of the mirror fluctuations, correlation length $l_B = 850d_{i0}$ and a Kolmogorov spectrum in space (see its PDF in Fig. 3.4).

The role of the PDF(B)

The limiting values of S_D in Fig. 3.5 depend only on the PDF(B) along the field lines. This fact is intuitive because the change in the pitch angle of a passing particle due to collisions as it travels the correlation length l_B of the field is very small, and the order in which the particle encounters regions of different B plays no role. Therefore, one can rearrange the mirror magnetic fluctuations (Fig. 3.3) by sorting the array elements in ascending order over some length L , $l_B \lesssim L \ll \lambda$, and making the resulting array periodic with period L (Fig. 3.6). Since the field is bounded, we do not lose statistical information if L is set to just a few l_B . Clearly, this procedure keeps the PDF(B) unchanged, and the resulting magnetic field produces the same amount of suppression, while having a much simpler shape. By comparing such simplified shapes of magnetic fluctuations for different field lines, one can determine which line causes more suppression. The loss cone for a particle is defined as $|\xi| > (1 - B/B_{\max})^{1/2}$, where B is the magnetic-field strength at the location of the particle and B_{\max} is the global maximum of the field strength. The more concave (or less convex in our case of the mirror fluctuations) the shape is, the more suppression is produced by magnetic mirroring, because the loss cones of most of the particles become narrower. The extreme case of this is a field that consists of narrow periodic peaks of height $B_{\max} - B_{\min}$. This field causes maximum suppression of diffusion for given values of B_{\min} and B_{\max} , because the loss cone for almost all the particles, $|\xi| > (1 - B_{\min}/B_{\max})^{1/2}$, is the narrowest it can be for all possible PDF(B). Based on this argument, and noticing that, in Fig. 3.4, the PDF of the saturated mirror field is more concentrated around the maximum field strength, one can predict more suppression of electron diffusion by secularly growing mirrors than by saturated ones, even though B_{\max} is smaller for the former than for the latter. Indeed, we see in Fig. 3.5 that the effect of the field shape prevails over the difference in B_{\max} , and the diffusion suppression is stronger for the secular phase.

The physical mechanism of the suppression of electron diffusion at large λ/l_B

In the limit $\lambda/l_B \gg 1$, Chandran et al. (1999) derived an analytic expression for the suppression of diffusivity of monoenergetic electrons by periodic magnetic mirrors [their equation (95)]:

$$S_D = \frac{3}{\langle 1/B' \rangle} \int_0^1 d\mu'_1 \int_{\mu'_1}^1 d\mu'_2 \frac{1}{\langle |\xi(\mu'_2)|/B' \rangle}, \quad (3.8)$$

where $B' = B/B_{\max}$ is the magnetic-field strength normalized to its global maximum value, $\mu' = \mu/\mu_{\text{crit}}$ is the magnetic moment of a particle $\mu = v^2(1 - \xi^2)/(2B)$ normalized to $\mu_{\text{crit}} = v^2/(2B_{\max})$, the averaging is performed over the period of the magnetic field, and the integration is carried over the passing particles in the loss cone. As we have discussed in Section 3.3.2, bounded mirror fluctuations can be replaced by periodic variations with the same PDF(B) without affecting the suppression factor. This means that equation (3.8), where the averaging in the angle brackets is done over PDF(B), can be readily applied to the simulated mirror fluctuations. The asymptotic values of S_D calculated by (3.8),

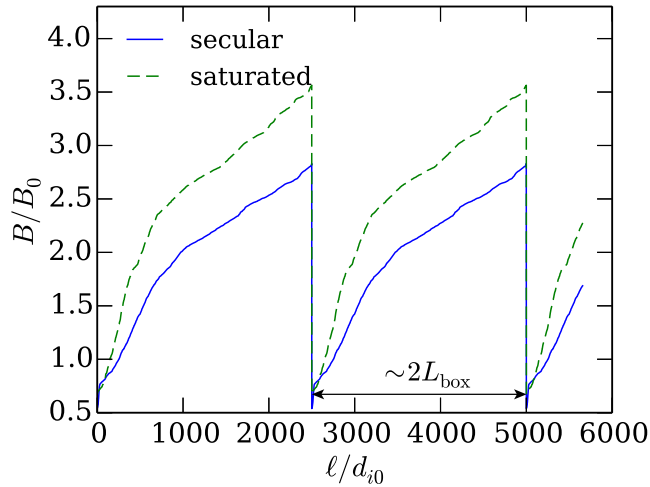


Figure 3.6: Equivalent representation of the mirror magnetic fluctuations along the field lines in the case $\lambda/l_B \gg 1$. Reordering the magnetic-field strength values over length $L \sim 2L_{\text{box}}$, $l_B \lesssim L \ll \lambda$, does not change the PDF(B) and, therefore, the amount of diffusion suppression.

$S_D \approx 0.117$ for the secularly growing mirrors and $S_D \approx 0.187$ for the saturated ones, agree extremely well with the results of our Monte Carlo simulation (see Fig. 3.5).

We can break down the suppression effect encoded in equation (3.8) into two physical effects:

$$S_D = S_p \frac{\lambda_{\text{eff}}}{\lambda}, \quad (3.9)$$

where S_p is the suppression of diffusivity due to the fact that only the passing particles contribute to electron transport, λ_{eff} is the effective mean free path of the passing particles, reduced because a passing particle is scattered out of the loss cone, becomes trapped and randomizes its direction of motion in only a fraction of its collision time. The parameters S_p and λ_{eff} have a very clear physical interpretation in terms of the particle velocity autocorrelation function.

The electron diffusion coefficient D can be expressed as the integral of the parallel-velocity autocorrelation function $C(t)$:

$$D = \int_0^\infty \langle v_{\parallel}(0)v_{\parallel}(t) \rangle dt \equiv \int_0^\infty C(t) dt. \quad (3.10)$$

Using the results of our Monte Carlo simulations of monoenergetic diffusion in magnetic fluctuations generated by the mirror instability, we can calculate the parallel-velocity autocorrelation function, which is, for monoenergetic electrons, the autocorrelation function of the cosine of the pitch angle $\xi = \cos \theta$, namely $C(t) = v^2 \langle \xi(0)\xi(t) \rangle$. It is plotted in

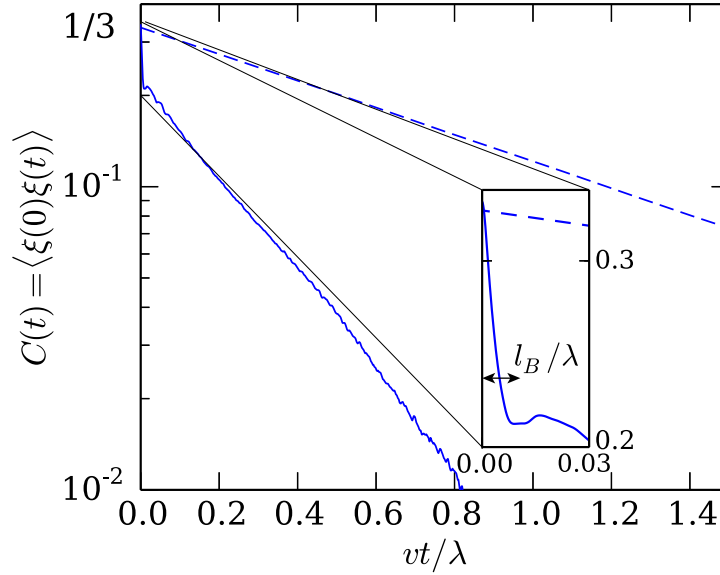


Figure 3.7: The parallel velocity autocorrelation functions $C(t)/v^2$ for electron diffusion in a constant magnetic field (dashed) and in the magnetic field of secularly growing mirrors (solid), based on the results of the Monte Carlo simulation. The ratio of the electron mean free path to the correlation length of the magnetic field $\lambda/l_B = 100$. The narrow peak at $t < l_B/v$ is caused by the bouncing trapped particles, which do not contribute to electron transport.

Fig. 3.7 for diffusion with no magnetic mirrors (dashed line) and diffusion in the mirror magnetic field with $\lambda/l_B = 100$ (solid line). With no mirrors,

$$C_0(t) = \frac{1}{3}v^2e^{-\nu t}, \quad (3.11)$$

where $\nu = v/\lambda$. Both with or without mirrors, the autocorrelation function is equal to $1/3$ at $t = 0$ due to isotropy (even in the presence of magnetic mirrors, collisions restore isotropy over times $\gg \nu^{-1}$). In the mirror field, $C(t)$ has a narrow peak of width $\sim l_B/v$ at small t , while the rest of the autocorrelation function is an exponential that is well fitted by

$$C(t > l_B/v) = \frac{1}{3}S_p v^2 e^{-\nu_{\text{eff}} t}, \quad (3.12)$$

where $S_p < 1$ and $\nu_{\text{eff}} > \nu$.

The narrow peak of $C(t)$ at small t is caused by the contribution to $C(t)$ of the population of trapped particles, which bounce inside magnetic traps at a typical time scale $\sim l_B/v$. The physical meaning of the reduction factor $S_p < 1$ is that only the passing

particles contribute to transport processes. This factor can be calculated as

$$S_p = f_{\text{pass}} \frac{\langle \xi^2 \rangle_{\text{pass}}}{\langle \xi^2 \rangle}, \quad (3.13)$$

where f_{pass} is the fraction of the passing particles, the averaging is performed over the passing particles in the numerator, and over all particles in the denominator. The value of S_p is greater than simply the fraction of the passing particles, because they travel in their loss cones and, therefore, have parallel velocities greater than the mean square parallel velocity $v^2 \langle \xi^2 \rangle = v^2/3$ averaged over all particles.

The physical interpretation of the fact that $\nu_{\text{eff}} > \nu$ in equation (3.12) is the reduced effective mean free path of the passing particles: recall that a passing particle travels only a fraction of λ before it becomes trapped and, obviously, $\nu_{\text{eff}}/\nu = \lambda/\lambda_{\text{eff}}$. Since the diffusion coefficient is the integral of $C(t)$ [equation (3.10)], we obtain equation (3.9).

From the above arguments, it follows that a system with magnetic mirrors and $\lambda/l_B \gg 1$ can be translated into a system with no mirrors, but with a lower mean square parallel velocity and an enhanced scattering rate. The lower parallel velocity is related to the fact that the passing particles become trapped now and then, and while they are trapped, their effective parallel velocity is zero.

Using the results of our Monte Carlo simulations and the velocity autocorrelation function analysis described above, we can measure S_p and $\lambda_{\text{eff}}/\lambda$. For the secularly growing mirrors, we get $S_p \approx 0.63$, $\lambda_{\text{eff}}/\lambda \approx 0.19$; for the saturated mirrors, $S_p \approx 0.74$, $\lambda_{\text{eff}}/\lambda \approx 0.26$. Substituting these into equation (3.9), we recover $S_D \approx 0.12$ and $S_D \approx 0.19$, the same as was obtained in direct measurement [equation (3.5)] and from equation (3.8).

3.3.3 Electron thermal conductivity in the limit $\lambda/l_B \gg 1$

As we have shown above, the effect of magnetic mirrors on scales much larger than the electron mean free path is the suppression of spatial diffusion via two effects: reduced fraction and reduced effective mean free path (or, equivalently, an enhanced scattering rate) of the passing particles participating in transport [see (3.9)]. In a plasma with a temperature gradient and no mirrors, heat transport is governed not only by pitch-angle diffusion, but by diffusion in the energy space as well. Magnetic mirrors do not change a particle's energy, therefore, one can model their effect on large scales by enhancing the pitch-angle scattering rate (but not the energy diffusion rate) and, simultaneously, reducing the effective density of particles carrying energy in order to subtract the trapped population.

The rates of pitch-angle scattering (perpendicular velocity diffusion) ν_{\perp} and energy exchange ν_{ε} for a test electron in a hydrogen plasma are (Spitzer, 1962)

$$\nu_{\perp,es} = 2[(1 - 1/2x)\psi(x) + \psi'(x)]\nu_0, \quad (3.14)$$

$$\nu_{\varepsilon,es} = 2[(m_e/m_s)\psi(x) - \psi'(x)]\nu_0, \quad (3.15)$$

where

$$\nu_0 = \frac{4\pi e^4 \ln \Lambda n_e}{m_e^2 v^2}, \quad x = v^2/v_{\text{th},e}^2, \quad (3.16)$$

$$\psi(x) = \frac{2}{\sqrt{\pi}} \int_0^x dt \sqrt{t} e^{-t}, \quad \psi'(x) = \frac{d\psi}{dx}, \quad (3.17)$$

$s = e, i$ is the species of the background particles, $v_{\text{th},e} = (2kT_e/m_e)^{1/2}$ is the electron thermal speed, and $\ln \Lambda \sim 40$ is the Coulomb logarithm. Heat is transferred by slightly superthermal electrons with $v \approx 2.5 v_{\text{th},e}$ (this rough estimate is based on a simple calculation of thermal conductivity for a Lorenz gas, when electrons interact only with ions). At this velocity, $\nu_{\perp,ei} \approx 1.5 \nu_0$, $\nu_{\perp,ee} \approx 1.8 \nu_0$, $\nu_\varepsilon = \nu_{\varepsilon,ei} + \nu_{\varepsilon,ee} \approx \nu_{\varepsilon,ee} \approx 2 \nu_0$. Thus, the electron energy exchange rate ν_ε is close to the total perpendicular electron diffusion rate $\nu_\perp \approx 3.3 \nu_0$ for the heat-conducting electrons.

At this point, we make a qualitative assumption that the total rate of spatial energy transfer can be reasonably approximated by the sum of the energy exchange rate and the pitch-angle scattering rate. This assumption is corroborated by the mathematical fact that in a plasma with a gradient of a diffusing passive scalar, the flux of the scalar is inversely proportional to the sum of the rate of spatial diffusion of the particles (or pitch-angle scattering) and the collisional exchange rate of the passive scalar [see Appendix 3.6, (3.30)]. The passive scalar in this calculations models temperature, as if every particle carried an averaged value of thermal energy that did not depend on the particle's velocity. Then for the thermal conductivity κ , we use the approximation

$$\kappa \sim \frac{v_{\text{th},e}^2}{\nu_\varepsilon + \nu_\perp}. \quad (3.18)$$

The reduction of the effective density of the heat-conducting electrons affects both pitch-angle and energy diffusion, while the enhanced scattering rate only affects pitch-angle diffusion. Thus, the suppression of thermal conduction is smaller than the suppression of spatial diffusion. A qualitative expression for the suppression of thermal conductivity $S_\kappa = \kappa/\kappa_0$ in the limit $\lambda/l_B \gg 1$ is then

$$S_\kappa \sim S_p \frac{\nu_\perp + \nu_\varepsilon}{(\lambda/\lambda_{\text{eff}})\nu_\perp + \nu_\varepsilon} \sim \frac{2S_p}{1 + \lambda/\lambda_{\text{eff}}}, \quad (3.19)$$

where S_p and λ_{eff} are the parameters in (3.9): S_p is related to the fraction of the passing particles, λ_{eff} is the effective mean free path of the passing particles. For a passive scalar in the limit $\lambda/l_B \gg 1$, (3.19) is exact and derived in Appendix 3.6 by establishing a simple relationship between the amount of suppression of the scalar flux and the parallel-velocity autocorrelation function. Substituting the values of S_p and $\lambda_{\text{eff}}/\lambda$ calculated at the end of Section 3.3.2 into (3.19), we obtain the suppression factor of thermal conductivity: $S_\kappa \sim 0.2$ for the secularly growing mirrors and $S_\kappa \sim 0.3$ for the saturated ones. We see that heat transport is suppressed by a factor of ~ 2 less than spatial diffusion, because the

diffusion in energy space is suppressed much less than the spatial (pitch-angle) diffusion. Equation (3.19) can only be used when S_p and λ_{eff} do not depend on the electron velocity (or, equivalently, on the electron mean free path λ), which is indeed the case in the limit $\lambda/l_B \gg 1$ (see Fig. 3.5).

3.4 Electron transport in MHD turbulence

As mentioned in Section 3.1, another source of fluctuations of magnetic-field strength in the ICM is turbulent stretching/compression of the field lines. The turbulent dynamo produces a stochastic distribution of the field strength along a field line: lognormal during the kinematic phase, exponential in saturation (see Schekochihin et al., 2004). However, as we have also noted in Section 3.1, we do not expect much suppression of thermal conduction by these fields, because the electron mean free path is smaller than the parallel correlation length of turbulent magnetic fluctuations, and so magnetic mirrors are rare and not very effective. In this section, we demonstrate this explicitly by means of an isotropic MHD simulation of turbulent dynamo.

3.4.1 Electron transport in a system of stochastic magnetic mirrors

Before we consider the magnetic fields produced by the turbulent MHD dynamo, let us first illustrate how different diffusion in a stochastic magnetic field is from the case of a periodic field (characteristic of the mirror fluctuations) by the example of a lognormally distributed field. A stochastic magnetic field with a long tail in its PDF produces a larger amount of suppression compared to periodic magnetic fluctuations, because the dominant suppression is caused by the so-called principal magnetic mirrors of strength $m_p = B_p/\langle B \rangle \gg 1$ separated from each other by a distance of order the effective mean free path (characteristic length that a passing particle travels before it gets scattered out of the loss cone and becomes trapped) λ/m_p (Malyshkin & Kulsrud, 2001). Because $\lambda/m_p \gg l_B$ (see Malyshkin & Kulsrud 2001 for a calculation of m_p), the principal mirrors arise at scales much larger than l_B and therefore are strong deviations of the field strength from the mean value found in the tail of the PDF.

We generate a lognormal magnetic field with a Kolmogorov spectrum and the same rms value of the logarithm of the field strength and the same correlation length l_B as the secularly growing mirror fluctuations analyzed in Section 3.3 (the dotted PDF in Fig. 3.4). The diffusivity suppression factor is obtained by a Monte Carlo simulation and shown in Fig. 3.5 by the dash-dotted line. Its dependence on λ/l_B is much steeper than for the mirror fields, with no constant asymptotic value at large λ/l_B . Qualitatively, it is quite similar to the effective suppression of conductivity obtained for stochastic distributions by Malyshkin & Kulsrud (2001, see their Fig. 3).

3.4.2 Electron transport in a saturated magnetic field produced by MHD dynamo.

We have demonstrated that the suppression of electron diffusion in a stochastic field may be considerably larger than in a mirror-like periodic field, most notably if $\lambda \gg l_B$. However, this regime is inapplicable to the magnetic fluctuations generated by MHD turbulence in the ICM, because there $\lambda \lesssim l_\nu < L_{\text{inj}} \sim l_B$, where l_ν is the viscous scale of turbulent eddies, L_{inj} the outer (injection) scale of turbulence, and l_B is the *parallel* correlation length of the magnetic field. While MHD-dynamo-produced magnetic fluctuations decorrelate at small (resistive) scales, it is the field's variation perpendicular to itself (direction reversals) that occurs at those scales, whereas the parallel variation is on scales l_B of order the flow scale $L_{\text{inj}} \gg \lambda$ (Schekochihin et al., 2002, 2004). In the cool cores of galaxy clusters, $\lambda \sim 0.05$ kpc, $l_\nu \sim 0.4$ kpc, $L_{\text{inj}} \sim 10$ kpc (based on the parameters for the Hydra A cluster given by Enßlin & Vogt 2006); in the hot ICM, $\lambda \sim 20$ kpc, $l_\nu \sim 100$ kpc, $L_{\text{inj}} \sim 200$ kpc. Schematically, the spectrum of magnetic-field-strength fluctuations in the ICM is shown in Fig. 3.1. In order for magnetic trapping to be effective, magnetic-field-strength fluctuations $\delta B/B \sim 1$ need to exist at spatial scales below the electron mean free path. While mirror fluctuations easily satisfy this condition, MHD turbulence capable of creating parallel magnetic fluctuations occupies scales above λ , so large suppression is not expected in this case.

In order to estimate an upper limit on the suppression of electron diffusion by MHD magnetic fluctuations, we use simulations of a turbulent MHD dynamo at different magnetic Prandtl numbers $\text{Pm} = \nu/\eta$, where ν is the fluid viscosity, η the magnetic diffusivity. Our code solves the full set of compressible MHD equations in 3D, and is based on the unsplit van Leer integrator combined with the constrained transport (CT) method, similar to the one implemented in *ATHENA* (Stone & Gardiner 2009). We initiate a 3D 256^3 periodic box of MHD plasma with magnetic fluctuations at the level $\beta = 2000$, and stir it by a random white-in-time nonhelical body force applied at the largest scales ($L_{\text{inj}} \sim$ the box size). As we noted earlier in this section, the smaller the ratio λ/L_{inj} is, the less effective magnetic trapping is. In terms of the Reynolds number $\text{Re} \sim L_{\text{inj}}u/\lambda\nu_{\text{th},i}$, it means that for small Ma/Re , where Ma is the Mach number of the turbulent motions, conduction suppression should be negligible. In the cores of galaxy clusters, $\text{Re} \sim 100$ (Hydra A), while in the bulk of the ICM, $\text{Re} \sim 1 - 10$ (ignoring the possible effects of microinstabilities on the gas viscosity). The typical Mach number in galaxy clusters is believed to be $\text{Ma} \sim 0.1$ (e.g., Zhuravleva et al., 2015). Because we seek to obtain an upper limit on suppression, we restrict our analysis to low Re , corresponding to the hot ICM (at such low Re , turbulence will not have a wide inertial range, but that is irrelevant because turbulent MHD dynamo only requires a stochastic velocity field, not necessarily a fully developed Kolmogorov turbulence). Namely, in our simulation, we use $\text{Re} = 3$, and $\text{Pm} = 1000$. The simulation lasts until the magnetic field becomes saturated: $\langle B^2 \rangle / (8\pi) \sim \langle \rho v^2 \rangle / 2$, where ρ is the mass density, v the turbulent plasma flow velocity (in saturation, $\beta \sim 50$ and $\text{Ma} \sim 0.1$). The structure of the magnetic and velocity fields in the saturated state is shown in Fig. 3.8: magnetic folds are clearly seen at the scale of the box, while the velocity is stochastic but

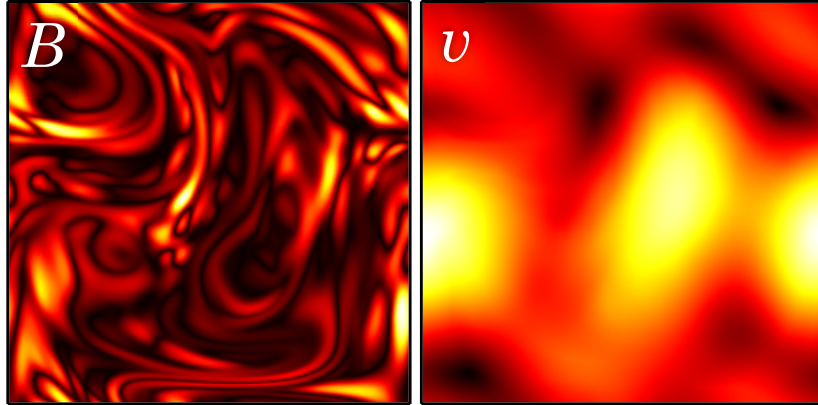


Figure 3.8: Central snapshot of cross-sections of a dynamo-generated magnetic-field (*left*) and velocity (*right*) magnitudes during the saturated turbulent MHD state for $\text{Pm} = 1000$, $\text{Re} = 3$.

smooth, due to low Re . This simulation setup and the properties of the saturated magnetic field are similar to those of the run ‘S4-sat’ in Schekochihin et al. (2004).

Following the same strategy as in the case of the mirror fields, we have extracted a magnetic-field line from the box in the saturated state. The extracted field line spans 100 box sizes (again, a field line does not bite its tail, although the box is periodic). This is necessary to make it statistically representative, because the PDF of the field now has an exponential tail. A line segment that spans eight boxes is shown in Fig. 3.9. The PDF of the magnetic-field strength calculated over the whole 3D simulation domain and one calculated along the field (by multiplying the 3D PDF by the magnetic-field strength) are shown in Fig. 3.10. They clearly exhibit an exponential shape. We calculate the suppression of electron diffusion in the same way as we did for the mirror fields in Section 3.3.2. The suppression factor is shown in Fig. 3.11 as a function of the ratio of the mean free path λ to the injection scale L_{inj}^2 . For the fiducial parameters of the hot ICM with the largest value of λ , we choose $L_{\text{inj}} \sim 200$ kpc and $\lambda \sim 20$ kpc. These parameters provide maximum suppression factor of electron diffusion $S_D \sim 0.9$. It is shown in Fig. 3.11 by the cross, the solid line corresponds to the suppression factor at lower λ , while the dashed line shows this factor for test monoenergetic electrons at higher λ to better exhibit the shape of the function $S_D(\lambda/l_B)$ for the dynamo-generated magnetic field. Though in this case, there is no simple connection between diffusivity and thermal conductivity [like (3.19)], because S_D now strongly depends on the mean free path (or velocity), the suppression of thermal conduction for $\lambda \lesssim 20$ kpc should be essentially insignificant.

²Note that this is a somewhat artificial parameter scan as we do not vary the ion mean free path, i.e., the viscosity, in a manner consistent with the electron mean free path.

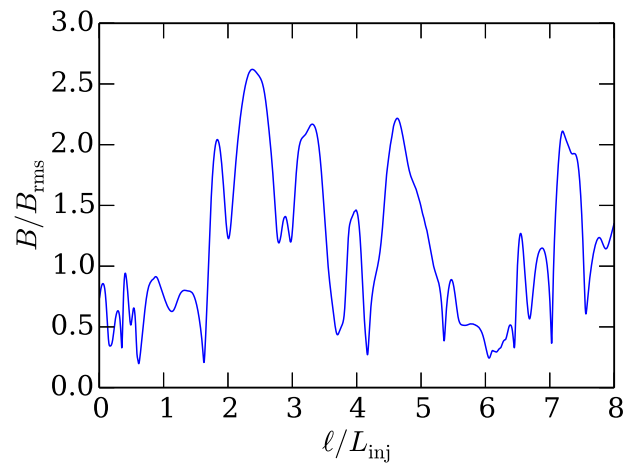


Figure 3.9: Variation of the magnetic-field strength along a field line segment that spans 8 boxes (box size = energy injection scale L_{inj}), taken from an MHD simulation of the saturated state of turbulent dynamo at $\text{Pm} = 1000$, $\text{Re} = 3$.

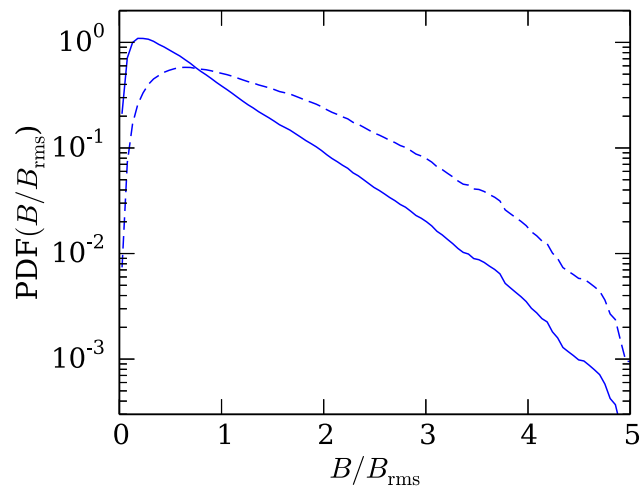


Figure 3.10: Solid line: the 3D PDF of the magnetic-field strength in saturated state for $\text{Pm} = 1000$, $\text{Re} = 3$. Dashed line: the PDF of B along the field line (the 3D PDF multiplied by B).

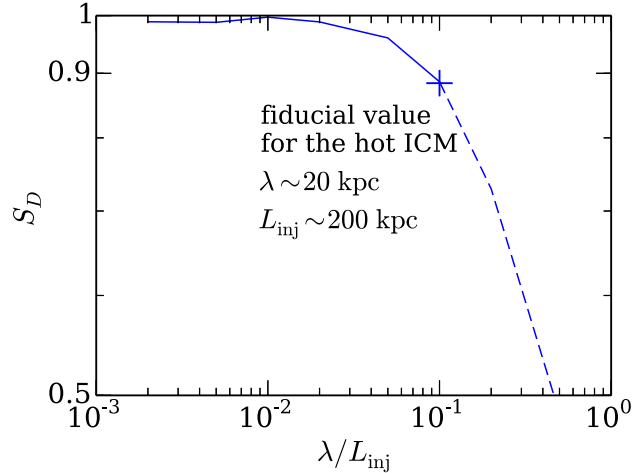


Figure 3.11: The suppression factor $S_D = D/D_0$ of the electron diffusivity by turbulent-dynamo-produced magnetic fields. The cross indicates the largest possible suppression for the fiducial parameters of the hot ICM: $L_{\text{inj}} \sim 200$ kpc, $\lambda \sim 20$ kpc.

3.5 Discussion

It is well recognized that thermal conduction in the ICM is anisotropic in the presence of even an extremely weak magnetic field. A popular assumption, adopted in many theoretical and numerical studies, is that conduction is suppressed across the field, while along the field, it is equal to the isotropic thermal conduction in an unmagnetized plasma. This assumption is typically applied to large-scale fields in the ICM, e.g., to scales of order 10 kpc, which correspond to the characteristic field correlation length inferred from Faraday rotation measurements (e.g., Kuchar & Enßlin, 2011). However, the ICM is likely to be susceptible to microinstabilities on much smaller scales comparable with the ion Larmor radius. In particular, the mirror instability can generate fluctuations of the field strength of large amplitude $\delta B/B \sim 1$, which can partially suppress electron transport along the field lines. Given that the ion Larmor radius is some 13 orders of magnitude smaller than the typical macroscopic scales, small-scale magnetic mirrors could potentially modify thermal conduction in a significant way, provided that mirrors can trap the electrons.

To address this question, we have examined the properties of the field-strength fluctuations in the recent shearing-box simulations of the mirror instability by Kunz et al. (2014). The striking difference between the magnetic fluctuations produced in these simulations and a generic random field is that their PDF(B) has sharp cutoffs at both low and high B , with the ratio of the maximal and minimal field strengths over the field lines $B_{\text{max}}/B_{\text{min}} \sim 6-7$. Since the ratio $B_{\text{max}}/B(\ell)$ determines the loss cone for a particle at the location ℓ along the line, the modest values of $B_{\text{max}}/B_{\text{min}}$ already suggest a limited amount of suppression, although it depends also on the exact shape of the PDF(B) (see

Section 3.3.2). While we have used 2D simulations, this imposes no obvious qualitative constraints on the mirror perturbations. The first 3D simulations of a dynamo-generated magnetic field by Rincon et al. (2016) indeed appear to show qualitatively familiar-looking mirrors being generated along stretched field lines. While the parallel correlation length of the mirror fluctuations in our work is not much smaller than the size of the computational box, this imposes no unphysical constraints on their structure. This is because the box is shearing-periodic, and the scale of mirrors is set by the distance to marginal stability, which depends on the shear, not on the box size (see Kunz et al. 2014 and Rincon et al. 2016).

Indeed, in our Monte Carlo simulations, we have found that the electron diffusivity is suppressed by a factor of ~ 8 for secularly growing mirrors and by a factor of ~ 5 for saturated ones. A lognormal magnetic field with the same rms would produce a much stronger suppression. We further argue that the suppression of thermal conduction relative to an unmagnetized plasma is a factor of ~ 2 less strong due to the fact that mirrors primarily affect spatial transport of the electrons, and much less the energy equilibration time. We conclude that microscale magnetic mirrors give rise to a factor of ~ 5 suppression of the parallel thermal conductivity.

In this work, we assumed a static magnetic field taken from a region of a plasma where the field lines are stretched by a linear shear. Though at a given location in the ICM plasma, the field lines are not constantly stretched, the turbulent dynamo produces a magnetic-field-line configuration that consists of long folds (regions of amplified field) and short reversals (regions of decreasing/weak field). This means that mirror fluctuations may develop almost everywhere along the field lines in a turbulent ICM (see Rincon et al. 2016 for the first numerical evidence of this). We note that it is not yet known how the mirror and firehose instabilities evolve over multiple correlation times of a turbulent velocity field. However, the recent results by Melville et al. (2016) indicate that at the values of β typical for the ICM, the relaxation of pressure anisotropy in a changing macroscale velocity shear is almost instantaneous compared to the shear time. This may therefore suggest that the mirror instability does not have time to ever reach the saturated state (at $St \gtrsim 2$ according to Kunz et al. 2014), because the turbulent shear decorrelates earlier (at $St \sim 1$). Thus, secularly growing mirrors are expected to be more common. In any case, since the results for both phases are similar up to a factor of order unity, we do not expect large deviations from the described above behavior. We may then argue that the amount of suppression found using the shearing-box simulations is characteristic for the ICM or any other turbulent weakly collisional high- β plasma.

When the parallel scale of the field is larger than the particles' mean free path, the suppression of conductivity is not strong because collisions are frequent enough to stop particle trapping. This means that even though macroscopic MHD turbulence can produce large-scale variations of B , the resulting suppression of parallel conduction should be negligible. We illustrate this point by carrying out MHD simulations of saturated turbulent dynamo and explicitly calculating the suppression factor (Section 3.4.2).

Parallel thermal conduction can also be reduced by anomalous pitch-angle scattering of electrons off magnetic perturbations. Such perturbations can be produced at the scale

of the electron Larmor radius by the whistler instability triggered by electron pressure anisotropy (Riquelme et al., 2016). In the ICM, Riquelme et al. (2016) estimate the resulting effective electron mean free path to be at most a few times smaller than the Coulomb mean free path, so our results remain valid (the mean free path is still much larger than the ion Larmor scale). The additional electron scattering will cause additional suppression of thermal conduction. The suppression by the mirror instability should then be our factor of $S_D \sim 1/5$ relative to this whistler-modified conductivity.

In addition to the suppression of parallel thermal conduction, the stochastic topology of the magnetic-field lines contributes to the total suppression of the global large-scale thermal conductivity by making the path travelled by an electron longer. When studying this effect, the effective increase of transverse diffusion due to the exponential divergence of the stochastic field lines should be taken into account (e.g., Rechester & Rosenbluth, 1978), because it restores the diffusive regime of spatial particle transport. If magnetic turbulence develops over a range of scales, the suppression effect is quite modest, $\sim 1/5$ of the Spitzer value (Narayan & Medvedev, 2001; Chandran & Maron, 2004). Since we have shown that the parallel conductivity is suppressed by another factor of ~ 5 , we argue that the global large-scale thermal conduction in the ICM is roughly $\sim 1/20 - 1/30$ of the Spitzer value.³

Acknowledgements

We thank S. C. Cowley for helpful discussions. The authors are grateful to W. Pauli Institute, Vienna, for its hospitality.

3.6 Appendix: transport of a passive scalar

Assume a collisional 1D gas with a linear mean gradient of a scalar quantity a transferred by the gas particles:

$$\langle a(x) \rangle = \text{const} + \alpha x. \quad (3.20)$$

Here and below, the angle brackets denote averaging over the particles' distribution. The gradient is sustained by fixed boundary conditions (e.g., walls kept at constant a). The particles can exchange a via collisions. Our goal is to evaluate the flux of a given by

$$q_a = \langle av_{\parallel} \rangle, \quad (3.21)$$

where v_{\parallel} is particle velocity (that is the parallel electron velocity along a field line in application to our problem).

Let us first write the Langevin equation for a particle's velocity:

$$\dot{v}_{\parallel} = -\nu_1 v_{\parallel} + \eta_1(t), \quad (3.22)$$

³And perhaps down by another factor of a few if whistlers are triggered and have the effect predicted by Riquelme et al. (2016).

where ν_1 is the particle-scattering collision rate, and $\eta_1(t)$ is a Gaussian white noise with zero mean. Solving for v_{\parallel} gives

$$v_{\parallel} = v_{\parallel}(0)e^{-\nu_1 t} + \int_0^t dt' e^{\nu_1(t'-t)} \eta_1(t'), \quad (3.23)$$

and, integrating again,

$$x = x(0) + \frac{v_{\parallel}(0)}{\nu_1}(1 - e^{-\nu_1 t}) + \int_0^t dt' \int_0^{t'} dt'' e^{\nu_1(t''-t')} \eta_1(t''). \quad (3.24)$$

The Langevin equation for the evolution of a of a given particle due to collisions reads:

$$\dot{a} = -\nu_2(a - \langle a \rangle) + \eta_2(t), \quad (3.25)$$

where ν_2 is the a -exchange collision rate, and η_2 is a Gaussian white noise with zero mean. Solving for a , we get

$$a = a(0)e^{-\nu_2 t} + \nu_2 \int_0^t dt' e^{\nu_2(t'-t)} \langle a[x(t')] \rangle + \int_0^t dt' e^{\nu_2(t'-t)} \eta_2(t'). \quad (3.26)$$

Combining equations (3.20), (3.21) and (3.26), we can calculate the scalar flux q_a at time t :

$$q_a = \langle a(t)v_{\parallel}(t) \rangle = \nu_2 \int_0^t dt' e^{\nu_2(t'-t)} \langle \langle a[x(t')] \rangle v_{\parallel}(t) \rangle = \alpha \nu_2 \int_0^t dt' e^{\nu_2(t'-t)} \langle x(t')v_{\parallel}(t) \rangle. \quad (3.27)$$

The noise terms do not contribute to the flux because they all have zero mean value. We can express $x(t')$ similar to equation (3.24) as

$$x(t') = x(t) - \frac{v_{\parallel}(t)}{\nu_1} [1 - e^{\nu_1(t'-t)}] + \int_t^{t'} dt'' \int_t^{t''} dt''' e^{\nu_1(t'''-t'')} \eta_1(t'''). \quad (3.28)$$

Substituting $x(t')$ into (3.27), we get

$$q_a = -\alpha \langle v_{\parallel}^2(t) \rangle \frac{\nu_2}{\nu_1} \int_0^t dt' e^{\nu_2(t'-t)} [1 - e^{\nu_1(t'-t)}] \rightarrow -\frac{\alpha}{3} \frac{\langle v^2 \rangle}{\nu_1 + \nu_2} \text{ as } t \rightarrow \infty, \quad (3.29)$$

where $\langle v_{\parallel}^2(t) \rangle = (1/3)\langle v^2 \rangle$. We see that the flux of the passive scalar a is inversely proportional to the sum of the scattering rate of the particles ν_1 and the a -exchange rate ν_2 . Then the scalar conductivity κ_{a0} is

$$\kappa_{a0} = \frac{1}{3} \frac{\langle v^2 \rangle}{\nu_1 + \nu_2}. \quad (3.30)$$

If the particles only exchange a and do not exchange energy, $\langle v^2 \rangle = v^2$.

It is also useful to derive the connection between the scalar flux q_a and the velocity autocorrelation function. Let us first write $x(t')$ as

$$x(t') = x(t) - \int_{t'}^t v_{\parallel}(t'') dt'' \quad (3.31)$$

and substitute this into (3.27):

$$\begin{aligned} q_a &= -\alpha\nu_2 \int_0^t dt' e^{\nu_2(t'-t)} \int_{t'}^t dt'' \langle v_{\parallel}(t'') v_{\parallel}(t) \rangle = -\alpha\nu_2 \int_0^t dt' e^{\nu_2(t'-t)} \int_{t'-t}^0 d\tau \langle v_{\parallel}(t+\tau) v_{\parallel}(t) \rangle \\ &\rightarrow -\alpha\nu_2 \int_0^{\infty} dt' e^{-\nu_2 t'} \int_0^{t'} d\tau C(\tau) \text{ as } t \rightarrow \infty, \end{aligned} \quad (3.32)$$

where $C(\tau) = \langle v_{\parallel}(0) v_{\parallel}(\tau) \rangle$ is the parallel-velocity autocorrelation function. For the conductivity κ_a of the scalar a , we infer

$$\kappa_a = \nu_2 \int_0^{\infty} dt' e^{-\nu_2 t'} \int_0^{t'} d\tau C(\tau). \quad (3.33)$$

With no magnetic mirrors, $C_0(\tau) = (1/3)v^2 e^{-\nu_1 \tau}$, and after substitution of C_0 into (3.33), we recover (3.30).

In Section 3.3.2, we demonstrated that in the limit $\lambda/l_B \gg 1$, the parallel velocity autocorrelation function of the monoenergetic electrons in the presence of mirror fluctuations has the form

$$C(t) = \frac{1}{3} S_p v^2 e^{-\nu_{\text{eff}} t}. \quad (3.34)$$

The coefficients S_p and ν_{eff} are determined by the Monte Carlo simulations. Now we can express κ_a in terms of these two coefficients and the a -exchange rate ν_2 by substituting $C(t)$ into (3.33):

$$\kappa_a = \frac{1}{3} \frac{S_p v^2}{\nu_{\text{eff}} + \nu_2} = \frac{1}{3} \frac{S_p v^2}{(\lambda/\lambda_{\text{eff}})\nu_1 + \nu_2}. \quad (3.35)$$

By combining equations (3.30) and (3.35), we obtain the suppression factor of the scalar conductivity κ_a/κ_{a0} :

$$\frac{\kappa_a}{\kappa_{a0}} = S_p \frac{\nu_1 + \nu_2}{(\lambda/\lambda_{\text{eff}})\nu_1 + \nu_2}. \quad (3.36)$$

We apply the above formula to relate the suppression of diffusion with the suppression of thermal conduction qualitatively, by taking a to be the electron temperature.

Bibliography

- Albright B. J., Chandran B. D. G., Cowley S. C., Loh M., 2001, *Phys. Plasmas*, 8, 777
- Bale S. D., Kasper J. C., Howes G. G., Quataert E., Salem C., Sundkvist D., 2009, *Phys. Rev. Lett.*, 103, 211101
- Carilli C. L., Taylor G. B., 2002, *A&A*, 40, 319
- Chandran B. D. G., Cowley S. C., 1998, *Phys. Rev. Lett.*, 80, 3077
- Chandran B. D. G., Cowley S. C., Ivanushkina M., Sydora R., 1999, *ApJ*, 525, 638
- Chandran B. D. G., Maron J. L., 2004, *ApJ*, 602, 170
- Chandrasekhar S., Kaufman A. N., Watson K. M., 1958, *Proc. R. Soc. A*, 245, 435
- Dennis T. J., Chandran B. D. G., 2005, *ApJ*, 622, 205
- Enßlin T. A., Vogt C., 2006, *A&A*, 453, 447
- Ettori S., Fabian A. C., 2000, *MNRAS*, 317, L57
- Feretti L., Giovannini G., Govoni F., Murgia M., 2012, *A&A Rev.*, 20, 54
- Hasegawa A., 1969, *Phys. Fluids*, 12, 2642
- Hellinger P., Trávníček P., Kasper J. C., Lazarus A. J., 2006, *Geophys. Res. Lett.*, 33, 9101
- Inogamov N. A., Sunyaev R. A., 2003, *Astron. Lett.*, 29, 791
- Kasper J. C., Lazarus A. J., Gary S. P., 2002, *Geophys. Res. Lett.*, 29, 1839
- Klepach E. G., Ptuskin V. S., 1995, *Astron. Lett.*, 21, 411
- Komarov S. V., Churazov E. M., Schekochihin A. A., ZuHone J. A., 2014, *MNRAS*, 440, 1153
- Kuchar P., Enßlin T. A., 2011, *A&A*, 529, A13
- Kulsrud R., 1964, in Rosenbluth M. N., ed., *Advanced Plasma Theory General Stability Theory in Plasma Physics*. Academic Press, New York, p. 54

- Kunz M. W., Schekochihin A. A., Stone J. M., 2014, *Phys. Rev. Lett.*, 112, 205003
- Kunz M. W., Stone J. M., Bai X.-N., 2014, *J. Comp. Phys.*, 259, 154
- Malyshkin L., 2001, *ApJ*, 554, 561
- Malyshkin L., Kulsrud R., 2001, *ApJ*, 549, 402
- Markevitch M., Mazzotta P., Vikhlinin A., Burke D., Butt Y., David L., Donnelly H., Forman W. R., Harris D., Kim D.-W., Virani S., Vrtilik J., 2003, *ApJ*, 586, L19
- Markevitch M., Ponman T. J., Nulsen P. E. J., Bautz M. W., Burke D. J., David L. P., Davis 2000, *ApJ*, 541, 542
- Markevitch M., Vikhlinin A., 2007, *Phys. Rep.*, 443, 1
- Melville S., Schekochihin A. A., Kunz M. W., 2016, *MNRAS*, 459, 2701
- Narayan R., Medvedev M. V., 2001, *ApJ*, 562, L129
- Parker E. N., 1958, *Phys. Rev.*, 109, 1874
- Rechester A. B., Rosenbluth M. N., 1978, *Phys. Rev. Lett.*, 40, 38
- Rincon F., Califano F., Schekochihin A. A., Valentini F., 2016, *Proc. Nat. Acad. Sci.*, 113, 3950
- Riquelme M. A., Quataert E., Verscharen D., 2016, *ApJ*, 824, 123
- Ruszkowski M., Begelman M. C., 2002, *ApJ*, 581, 223
- Schekochihin A., Cowley S., Maron J., Malyshkin L., 2002, *Phys. Rev. E*, 65, 016305
- Schekochihin A. A., Cowley S. C., 2006, *Phys. Plasmas*, 13, 056501
- Schekochihin A. A., Cowley S. C., Kulsrud R. M., Hammett G. W., Sharma P., 2005, *ApJ*, 629, 139
- Schekochihin A. A., Cowley S. C., Taylor S. F., Maron J. L., McWilliams J. C., 2004, *ApJ*, 612, 276
- Schuecker P., Finoguenov A., Miniati F., Böhringer H., Briel U. G., 2004, *A&A*, 426, 387
- Skilling J., McIvor I., Holmes J. A., 1974, *MNRAS*, 167, 87P
- Spitzer L., 1962, *Physics of Fully Ionized Gases*. Interscience, New York
- Stone J. M., Gardiner T., 2009, *New Astron.*, 14, 139
- Subramanian K., Shukurov A., Haugen N. E. L., 2006, *MNRAS*, 366, 1437

Vikhlinin A., Markevitch M., Murray S. S., 2001, *ApJ*, 549, L47

Voigt L. M., Fabian A. C., 2004, *MNRAS*, 347, 1130

Zakamska N. L., Narayan R., 2003, *ApJ*, 582, 162

Zhuravleva I., Churazov E., Arévalo P., Schekochihin A. A., Allen S. W., Fabian A. C., Forman W. R., Sanders J. S., Simionescu A., Sunyaev R., Vikhlinin A., Werner N., 2015, *MNRAS*, 450, 4184

Zhuravleva I., Churazov E., Schekochihin A. A., Allen S. W., Arévalo P., Fabian A. C., Forman W. R., Sanders J. S., Simionescu A., Sunyaev R., Vikhlinin A., Werner N., 2014, *Nature*, 515, 85

Chapter 4

Polarization of thermal bremsstrahlung emission due to electron pressure anisotropy in galaxy-cluster plasmas

MNRAS, 2016, 461, 2162

S. V. Komarov, I. I. Khabibullin, E. M. Churazov and A. A. Schekochihin

Abstract. Astrophysical plasmas are typically magnetized, with the Larmor radii of the charged particles many orders of magnitude smaller than their collisional mean free paths. The fundamental properties of such plasmas, e.g., conduction and viscosity, may depend on the instabilities driven by the anisotropy of the particle distribution functions and operating at scales comparable to the Larmor scales. We discuss a possibility that the pressure anisotropy of thermal electrons could produce polarization of thermal bremsstrahlung emission. In particular, we consider coherent large-scale motions in galaxy clusters to estimate the level of anisotropy driven by stretching of the magnetic-field lines by plasma flow and by heat fluxes associated with thermal gradients. Our estimate of the degree of polarization is $\sim 0.1\%$ at energies $\gtrsim kT$. While this value is too low for the forthcoming generation of X-ray polarimeters, it is potentially an important proxy for the processes taking place at extremely small scales, which are impossible to resolve spatially. The absence of the effect at the predicted level may set a lower limit on the electron collisionality in the ICM. At the same time, the small value of the effect implies that it does not preclude the use of clusters as (unpolarized) calibration sources for X-ray polarimeters at this level of accuracy.

4.1 Introduction

For the electrons in a hot tenuous astrophysical plasma, the equilibration time scale due to Coulomb collisions is often sufficiently long compared to other characteristic time scales to allow for deviations from thermal equilibrium manifested by anisotropies or non-thermal tails. The latter typically require a mechanism to accelerate a fraction of particles to high energies, e.g., magnetic reconnection or diffusive shock acceleration (Krymskii 1977; Axford et al. 1977; Blandford & Ostriker 1978; Bell 1978). Anisotropies, on the other hand, are commonly associated with the presence of a magnetic field.

In many astrophysical plasmas, magnetic fields are strong enough to force a charged particle to orbit around a field line with the Larmor radius many orders of magnitude smaller than the particle’s collisional mean free path. If the magnetic field is not constant in time, adiabatic invariance compels the perpendicular and parallel components of the particle’s velocity to adjust to the field magnitude in different ways, thus producing pressure anisotropy (Chew et al., 1956; Kulsrud, 1964). A heat flux along the field lines also contributes to anisotropy. Above a certain threshold, pressure anisotropies trigger kinetic microinstabilities, e.g., firehose and mirror (Chandrasekhar et al., 1958; Parker, 1958; Hasegawa, 1969), which are believed to hold the anisotropy at a marginal level by increasing the effective collision rate via scattering off magnetic perturbations and magnetic trapping (for observational evidence in the solar wind, see Kasper et al. 2002; Hellinger et al. 2006; Bale et al. 2009; for theoretical discussion, see, e.g., Melville et al. 2016 and references therein).

Temporal changes of magnetic-field strength may be caused by random turbulent motions or by a specific ordered plasma flow, e.g., a flow past a cold dense cloud of gas in “cold fronts” in the ICM (see, e.g., Markevitch & Vikhlinin, 2007, for a review) or a shear flow in accretion disks (Sharma et al., 2006). Cold fronts also manifest sharp temperature gradients at the interface between the cold cloud and the hot ambient plasma. In a hot rarefied plasma, the electron temperature anisotropy generated by both the magnetic-field evolution and heat fluxes leaves an imprint in the form of polarization of bremsstrahlung emission (for an example in solar flares, see, e.g., Haug, 1972). If a flow orients the magnetic field in some preferential direction, the polarization does not cancel out and potentially can be observed by X-ray polarimeters.

In this chapter, we examine the possible magnitude and detectability of electron pressure anisotropy in galaxy clusters. We start by describing the theoretical framework for the problem at hand. Generation of pressure anisotropies in a plasma with evolving magnetic fields and temperature gradients is discussed in Section 4.2.1. In Section 4.2.2, we derive the polarization of bremsstrahlung emission for a given anisotropic bi-Maxwellian electron distribution. Then we proceed with application of our theory to cold fronts and shocks in the ICM with the help of analytical models and numerical magnetohydrodynamic (MHD) simulations (Section 4.3). The effects are weak, of the order of 0.1%, but they produce a characteristic pattern and may provide constraints on the pressure anisotropy and electron collisionality in the ICM. We briefly discuss the role of the effects for observations of galaxy clusters with future X-ray calorimeters in Section 4.4. Finally, we summarize our findings

in Section 4.5.

4.2 Theoretical framework

4.2.1 Generation of pressure anisotropies in a weakly collisional plasma

In an astrophysical plasma, the Larmor radii ρ_s of all particle species are typically much smaller than their collisional mean free paths λ_s ; equivalently, their collision frequencies ν_s are much smaller than the Larmor frequencies Ω_s ($s = i, e$, with e the electrons, i the ions). If the magnetic-field strength B changes slowly, $\gamma = B^{-1}dB/dt$, each particle conserves its first adiabatic invariant $\mu = v_{\perp s}^2/2B \propto p_{\perp s}/B$, which is the magnetic moment of the particle, where $v_{\perp s}$ is the component of the particle's velocity perpendicular to the field line, $p_{\perp s}$ is the perpendicular pressure. To demonstrate how pressure anisotropy is driven and sustained by evolving magnetic fields in an incompressible plasma with no heat flux, we express the assumption that μ is conserved but for rare occasional collision as

$$\frac{1}{p_{\perp s}} \frac{dp_{\perp s}}{dt} \sim \frac{1}{B} \frac{dB}{dt} - \nu_s \frac{p_{\perp s} - p_{\parallel s}}{p_{\perp s}}, \quad (4.1)$$

where $p_{\parallel s}$ is the parallel pressure, and the last term corresponds to isotropization of pressure by collisions. If $\gamma \ll \nu_s$, the pressure anisotropy Δ_s can be estimated from the balance between the collisional relaxation and the rate of change of the magnetic-field:

$$\Delta_s = \frac{p_{\perp s} - p_{\parallel s}}{p_{\perp s}} \sim \frac{1}{\nu_s} \frac{1}{B} \frac{dB}{dt} = \frac{\gamma}{\nu_s}. \quad (4.2)$$

It is clear from this estimate that the electron anisotropy is $\nu_e/\nu_i \sim (m_i/m_e)^{1/2} \approx 40$ times weaker than that of the ions (if the electron and ion temperatures are equal).

The more general form of Δ_s taking into account the evolution of the parallel pressure can be obtained from the so-called CGL equations (Chew et al., 1956) with collisions retained, which are derived by taking the second moments of the kinetic magnetohydrodynamics equations (KMHD). The KMHD equations arise after averaging the full kinetic equation over the gyroangle. The CGL equations read

$$p_{\perp s} \frac{d}{dt} \ln \frac{p_{\perp s}}{n_s B} = \nabla \cdot (q_{\perp s} \mathbf{b}) - q_{\perp s} \nabla \cdot \mathbf{b} - \nu_s (p_{\perp s} - p_{\parallel s}), \quad (4.3)$$

$$p_{\parallel s} \frac{d}{dt} \ln \frac{p_{\parallel s} B^2}{n_s^3} = \nabla \cdot (q_{\parallel s} \mathbf{b}) + 2q_{\perp s} \nabla \cdot \mathbf{b} - 2\nu_s (p_{\parallel s} - p_{\perp s}), \quad (4.4)$$

where $d/dt = \partial/\partial t + \mathbf{u}_s \cdot \nabla$ is the convective derivative associated with species s (\mathbf{u}_s is the plasma flow velocity), \mathbf{b} is the unit vector in the direction of the magnetic field, and

n_s the number densities,

$$p_{\perp s} = \int d^3\mathbf{w} \frac{m_s w_{\perp}^2}{2} f_s, \quad (4.5)$$

$$p_{\parallel s} = \int d^3\mathbf{w} m_s w_{\parallel}^2 f_s \quad (4.6)$$

are the perpendicular and parallel pressures,

$$q_{\perp s} = \int d^3\mathbf{w} \frac{m_s w_{\perp}^2}{2} w_{\parallel} f_s, \quad (4.7)$$

$$q_{\parallel s} = \int d^3\mathbf{w} m_s w_{\parallel}^3 f_s, \quad (4.8)$$

$q_{\perp s}$ and $q_{\parallel s}$ are heat fluxes (the parallel flux of the ‘‘perpendicular internal energy’’ and the parallel flux of the ‘‘parallel internal energy’’, respectively), \mathbf{w} the thermal component of a particle’s velocity, f_s the distribution functions of the particles. Subtracting equation (4.4) from equation (4.3), we get an evolution equation for the pressure anisotropy:

$$\begin{aligned} \frac{d}{dt}(p_{\perp s} - p_{\parallel s}) &= (p_{\perp s} + 2p_{\parallel s}) \frac{1}{B} \frac{dB}{dt} + (p_{\perp s} - 3p_{\parallel s}) \frac{1}{n_s} \frac{dn_s}{dt} - \nabla \cdot [(q_{\perp s} - q_{\parallel s})\mathbf{b}] - 3q_{\perp s} \nabla \cdot \mathbf{b} \\ &\quad - 3\nu_s(p_{\perp s} - p_{\parallel s}). \end{aligned} \quad (4.9)$$

Assuming that collisions are fast compared to the fluid motions, the pressure anisotropy is then small, $p_{\parallel s} - p_{\perp s} \ll p_{\perp s} \approx p_{\parallel s} \approx p_s$, the collisional heat fluxes are $q_{\perp s} \approx (1/3)q_{\parallel s}$, and the total heat flux along a field line $q_s = q_{\perp s} + q_{\parallel s}/2 = (5/6)q_{\parallel s}$. The value of the anisotropy is set by the balance between collisional relaxation and various driving terms:

$$\Delta_s \approx \frac{p_{\perp s} - p_{\parallel s}}{p_s} \approx \frac{1}{\nu_s} \left[\frac{1}{B} \frac{dB}{dt} - \frac{2}{3} \frac{1}{n_s} \frac{dn_s}{dt} + \frac{4\nabla \cdot (q_s \mathbf{b}) - 6q_s \nabla \cdot \mathbf{b}}{15p_s} \right]. \quad (4.10)$$

Thus, the pressure anisotropy is driven by changing magnetic-field strength, changing particle density, and by parallel heat fluxes.

It is useful to estimate the degree of anisotropy induced by different driving terms in (4.10). If we consider fluid motions with velocity u at scale L_u , variations of B at the scale of the velocity field $L_B = L_u$, and parallel temperature gradient $\nabla_{\parallel} T_s \sim \delta T_s / L_T$ at scale L_T , we can evaluate the contribution $\Delta_{B,n;s}$ of changing B and n , and the contribution $\Delta_{T;s}$ of the heat fluxes, to the total anisotropy as

$$\Delta_{B,n;s} \sim \frac{u}{v_{\text{th},s}} \frac{\lambda_s}{L_u}, \quad (4.11)$$

$$\Delta_{T;s} \sim \frac{\lambda_s^2}{L_T L_u} \frac{\delta T_s}{T_s}, \quad (4.12)$$

where we have used the expression for the heat flux $q_s = -\kappa_s \nabla_{\parallel} T_s$ with thermal conductivity $\kappa_s \sim n_s v_{\text{th},s} \lambda_s$, λ_s the mean free path, $v_{\text{th},s}$ the thermal speed. Assume that the flow

velocity is nearly sonic, $u \sim v_{\text{th},i}$, and that the variations of temperature are of order unity, $\delta T/T \sim 1$. Then $\Delta_T \sim \lambda^2/(L_u L_T)$ for both particle species, and $\Delta_{B,n;s} \sim \lambda/L_u \times v_{\text{th},s}/v_{\text{th},i}$. Hence, in our ordering, for the ions, the term linked to the magnetic-field changes $\Delta_{B,n;i} \sim \lambda/L_u$ is dominant if $L_T \gg \lambda$ (even in astrophysical systems with very sharp temperature gradients, e.g., cold fronts or buoyant bubbles of relativistic plasma in the ICM, the magnetic-field lines are typically stretched by the fluid flow in the direction perpendicular to the gradient (e.g., Komarov et al., 2014), thus significantly increasing the scale of temperature variation along the field lines). For the electrons, $\Delta_{B,n;e} \sim 1/40 \times \lambda/L_u$, and the two contributions can be of the same order ($\Delta_{B,n;e} \sim \Delta_{T;e}$), depending on the properties of the flow and the orientation of the magnetic-field lines connecting the hot and cold regions of the plasma. Note that the total anisotropy $\Delta_{\text{tot}} = \Delta_e + \Delta_i$ is bounded from below by the firehose instability, $\Delta_{\text{tot}} > -2/\beta$, where β is the ratio of thermal to magnetic-energy densities. If the positive ion anisotropy dominates ($\Delta_i \gg \Delta_e$), then the mirror instability compels Δ_i to stay below the mirror marginal level, $\Delta_i \lesssim 1/\beta$. Therefore, in regions of high plasma β , either γ ($= B^{-1}dB/dt$) or ν_s is modified by the instabilities to keep the anisotropy between the marginal levels, $-2/\beta < \Delta_{\text{tot}} < 1/\beta$ (e.g., Melville et al., 2016). In Appendix 4.6, we calculate the ion anisotropy for the simulated cold fronts (Section 4.3) and mark the regions where the firehose and mirror instabilities could develop. Because in our work the ion anisotropy is typically dominant, the two instabilities are regulated by the ions.

In this work, we are primarily interested in electron pressure anisotropy because of its possible observational imprint in the form of polarization of thermal bremsstrahlung. From the above estimates, it is clear that in the case of astrophysical systems with large temperature gradients, the driving term linked to heat fluxes must be taken into account along with the driving by the magnetic-field changes. We do this in detail for cold fronts in Section 4.3.

4.2.2 Polarization of bremsstrahlung by electron anisotropy

Consider first the polarization of bremsstrahlung emission from an electron beam deflected by a single ion. At low energies (compared to the kinetic energy of an electron), photons produced by small-angle scattering of the electrons off the ion are polarized in the plane perpendicular to the electron beam due to the mainly perpendicular acceleration that slightly changes only the direction of the electron velocity. At higher energies, when both the direction and the magnitude of the electron velocity change significantly, polarization becomes dominated by the acceleration the electrons experience parallel to the beam. Below, we demonstrate that the latter regime is of first importance for our problem, because the degree of polarization is considerably larger at high energies in the case of thermal bremsstrahlung from a cloud of anisotropic electrons.

Bremsstrahlung emission from a beam of electrons of energy ε is fully described by differential cross sections per unit solid angle and photon energy, $d^2\sigma_{\perp}(\varepsilon, \epsilon, \theta)$ and $d^2\sigma_{\parallel}(\varepsilon, \epsilon, \theta)$, for the components perpendicular and parallel to the radiation plane (spanned by an emitted photon's and an initial electron's momenta). Here, $d^2 = d^2/(d\epsilon d\Omega)$, ϵ stands for the

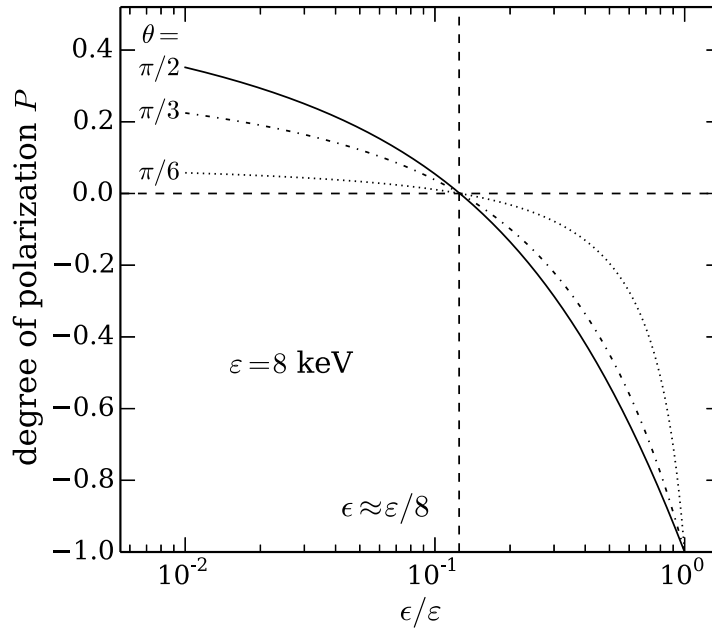


Figure 4.1: The degree of bremsstrahlung polarization $P(\epsilon, \theta) = (d^2\sigma_{\perp} - d^2\sigma_{\parallel}) / (d^2\sigma_{\perp} + d^2\sigma_{\parallel})$ from a beam of electrons of energy $\epsilon = 8$ KeV as a function of the emitted photon's energy ϵ and the angle θ between the beam axis and the photon's momentum.

emitted photon's energy, and θ the angle between the emitted photon's momentum and the beam axis. We use the fully relativistic cross sections calculated by Gluckstern & Hull (1953) in the first Born approximation, which are appropriate for the problem at hand¹. Because the formulae in the original paper by Gluckstern & Hull (1953), as well as those given later by Bai & Ramaty (1978), are both subjected to typos, we provide the correct explicit expressions for the cross sections in Appendix 4.7. The degree of polarization is $P(\epsilon, \theta) = (d^2\sigma_{\perp} - d^2\sigma_{\parallel}) / (d^2\sigma_{\perp} + d^2\sigma_{\parallel}) = d^2\sigma_1 / d^2\sigma_0$, where $d^2\sigma_1$ is the differential cross section of the polarized emission, $d^2\sigma_0$ of the total emission. Its dependence on the photon energy and direction with respect to the beam axis is illustrated in Fig. 4.1. The transition between the perpendicular and parallel polarization occurs at photon energy $\epsilon \sim \epsilon/8$. As noted before, the perpendicular polarization at low energies is produced by small-angle scattering of the electrons, while the parallel is the result of collisions that significantly change the electron energy.

Since the differential cross sections presented above are essentially the 'Green's functions' of the bremsstrahlung emission, the total and polarized emission from a cloud of electrons can be found by integrating over the electron distribution function. Let us introduce

¹The limit of validity of this approximation is given by condition $\epsilon' / m_e c^2 \gg (Z/137)^2$, where Z is the charge of the scattering ion in atomic units, ϵ' the energy of an outgoing electron (Gluckstern & Hull, 1953). For $Z = 1$, the condition is satisfied for outgoing electrons at energies $\epsilon' \gg 30$ eV.

a spherical coordinate system and assume that the electron distribution is axisymmetric with respect to the magnetic-field direction, taken to be the z axis. We denote the unit vector in the direction of the incoming electron $\hat{\mathbf{p}} = (\sin \theta_0 \cos \phi_0, \sin \theta_0 \sin \phi_0, \cos \theta_0)$, and the direction of the line of sight $\hat{\mathbf{k}} = (\sin \theta, 0, \cos \theta)$ (choose $\phi = 0$ without loss of generality because the resulting polarization pattern is also axisymmetric). The geometry of the vectors is illustrated in Fig. 4.2. The polarization directions perpendicular and parallel to the plane spanned by the vectors $\hat{\mathbf{p}}$ and $\hat{\mathbf{k}}$ (the radiation plane) are, respectively,

$$\hat{\mathbf{e}}_{\perp} = \frac{\hat{\mathbf{p}} \times \hat{\mathbf{k}}}{|\hat{\mathbf{p}} \times \hat{\mathbf{k}}|}, \quad (4.13)$$

$$\hat{\mathbf{e}}_{\parallel} = \frac{\hat{\mathbf{k}} \times (\hat{\mathbf{p}} \times \hat{\mathbf{k}})}{|\hat{\mathbf{p}} \times \hat{\mathbf{k}}|}. \quad (4.14)$$

Then $\hat{\mathbf{e}}_{\perp}$ is rotated by angle χ (see Fig. 4.2) with respect to the y direction, which is the perpendicular polarization direction in the reference xz plane that contains the line of sight $\hat{\mathbf{k}}$. The angle χ is expressed as

$$\cos \chi = \hat{\mathbf{e}}_{\perp y} = (\sin \theta \cos \theta_0 - \cos \theta \sin \theta_0 \cos \phi_0) / \sin \theta', \quad (4.15)$$

where θ' is the angle between $\hat{\mathbf{p}}$ and $\hat{\mathbf{k}}$:

$$\cos \theta' = \cos \theta \cos \theta_0 + \sin \theta \sin \theta_0 \cos \phi_0. \quad (4.16)$$

Linear polarization (for unpolarized electrons, bremsstrahlung photons are never circularly polarized) is described by the two independent Stokes parameters P_1 and P_2 : P_1 corresponds to the degree of polarization with respect to a given reference plane (xz in our case); P_2 to the degree of polarization with respect to a plane rotated around the line of sight by $\pi/4$ from the reference plane. For a given momentum of the initial electron, P_1 and P_2 , normalized by the total intensity, are transformed by rotation of the radiation plane relative to the reference plane as

$$\begin{aligned} P_{1,\hat{\mathbf{p}}} &= \cos 2\chi \frac{d^2 \sigma_1}{d^2 \sigma_0}, \\ P_{2,\hat{\mathbf{p}}} &= \sin 2\chi \frac{d^2 \sigma_1}{d^2 \sigma_0}. \end{aligned} \quad (4.17)$$

Thus, knowing the expression for the angle χ [equation (4.15)] between the radiation and reference planes, we can calculate the degree of polarization of bremsstrahlung emission from a cloud of electrons $P_{1,2} = \mathcal{I}_{1,2}/\mathcal{I}_0$, where $\mathcal{I}_{1,2}$ is the intensity of the polarized emission and \mathcal{I}_0 the total intensity, both integrated over the electron distribution $F(\varepsilon, \theta_0)$:

$$\mathcal{I}_0(\varepsilon, \theta) = n_i \int_{\varepsilon}^{\infty} d\varepsilon \int_{-1}^1 d(\cos \theta_0) \int_0^{2\pi} d\phi_0 v(\varepsilon) F(\varepsilon, \theta_0) d^2 \sigma_0(\varepsilon, \varepsilon, \theta'), \quad (4.18)$$

$$\mathcal{I}_1(\varepsilon, \theta) = n_i \int_{\varepsilon}^{\infty} d\varepsilon \int_{-1}^{+1} d(\cos \theta_0) \int_0^{2\pi} d\phi_0 v(\varepsilon) F(\varepsilon, \theta_0) \cos 2\chi d^2 \sigma_1(\varepsilon, \varepsilon, \theta'), \quad (4.19)$$

$$\mathcal{I}_2(\varepsilon, \theta) = n_i \int_{\varepsilon}^{\infty} d\varepsilon \int_{-1}^{+1} d(\cos \theta_0) \int_0^{2\pi} d\phi_0 v(\varepsilon) F(\varepsilon, \theta_0) \sin 2\chi d^2 \sigma_1(\varepsilon, \varepsilon, \theta'). \quad (4.20)$$

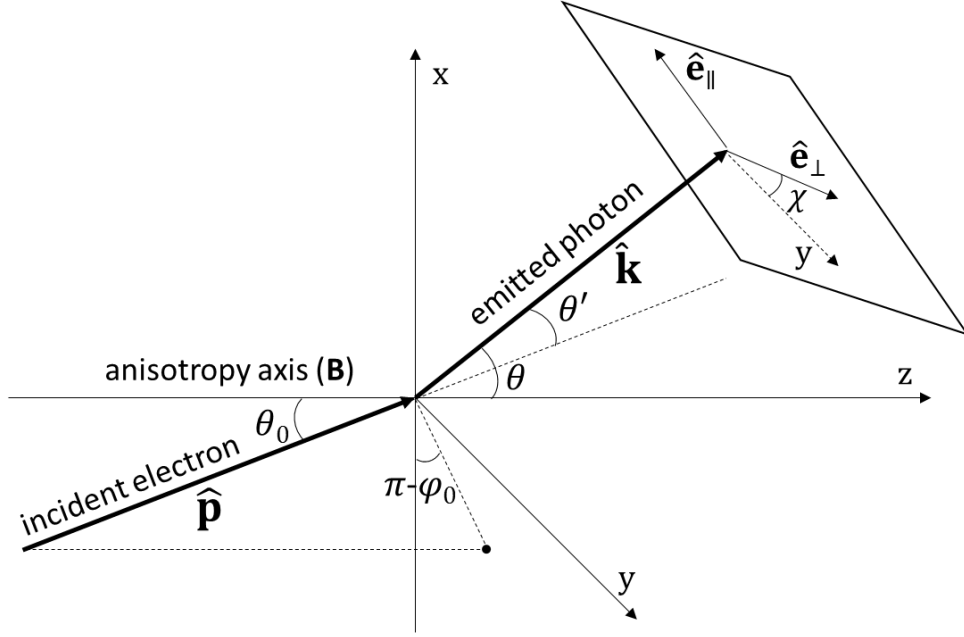


Figure 4.2: Geometry for the problem of the polarization of bremsstrahlung emission from a cloud of electrons.

Due to the axisymmetry of the electron distribution function, \mathcal{I}_2 integrates to zero [see, e.g., the appendix of Haug (1972) for a mathematical proof of this], and the total degree of linear polarization is $P = \mathcal{I}_1/\mathcal{I}_0$.

The distribution function $F(\varepsilon, \theta_0)$ is related to the velocity distribution function $f(v, \theta_0)$ as

$$F(\varepsilon, \theta_0) = v^2 f(v, \theta_0) \frac{dv}{d\varepsilon}. \quad (4.21)$$

For the velocity distribution function, we employ a bi-Maxwellian:

$$f(v, \theta_0) = n_e \left(\frac{m_e}{2\pi T_\perp} \right) \left(\frac{m_e}{2\pi T_\parallel} \right)^{1/2} \exp \left[-\frac{m_e v^2}{2T_0} \left(\frac{T_0}{T_\perp} \sin^2 \theta_0 + \frac{T_0}{T_\parallel} \cos^2 \theta_0 \right) \right]. \quad (4.22)$$

where $T_0 = (1/3)T_\parallel + (2/3)T_\perp$ is the total temperature. If the anisotropy

$$\Delta = \frac{T_\perp - T_\parallel}{T_0} \quad (4.23)$$

is small, and $\Delta m_e v^2 / (2T_0) \ll 1$, one can expand the distribution function to the first order in Δ :

$$f(v, \theta_0) = f_0(v) + \delta f_\Delta(v, \theta_0), \quad (4.24)$$

where $f_0(v)$ is an isotropic Maxwell distribution at temperature T_0 :

$$f_0(v) = n_e \left(\frac{m_e}{2\pi T_0} \right)^{3/2} \exp \left(-\frac{m_e v^2}{2T_0} \right), \quad (4.25)$$

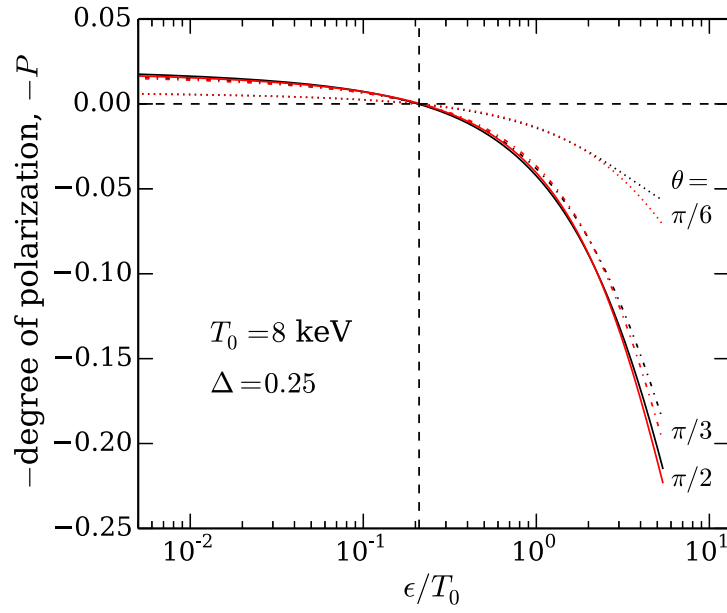


Figure 4.3: The degree of bremsstrahlung polarization from a cloud of electrons with a bi-Maxwellian distribution at temperature $T_0 = 8$ keV and anisotropy level $\Delta = 0.25$ [(4.23)] as a function of the emitted photon energy ϵ and the angle between the axis of anisotropy and the line of sight. Results in the linear approximation [equations (4.24)-(4.25)] are shown in red for comparison. The polarization degree is plotted with the minus sign to facilitate comparison with Fig. 4.1. The opposite sign comes from the fact that the electron pressure anisotropy Δ is defined to be positive for $T_\perp > T_\parallel$ [equation (4.23)].

and the anisotropic perturbation is

$$\delta f_{\Delta}(v, \theta_0) = \Delta \frac{m_e v^2}{2T_0} \left(\frac{1}{3} - \cos^2 \theta_0 \right) f_0(v). \quad (4.26)$$

Using equations (4.20), (4.21), and (4.26), we obtain the degree of polarization of thermal bremsstrahlung for a small anisotropic perturbation of the electron distribution, when the linear approximation (expansion in Δ) [equation (4.24)] is applicable:

$$P(\epsilon, T_0, \theta) = \Delta \sin^2 \theta G(\epsilon, T_0), \quad (4.27)$$

where $G(\epsilon, T_0)$ becomes a function of ϵ/T_0 at temperatures $T_0 \lesssim 10$ keV. At $\epsilon \sim$ a few T_0 , $G(\epsilon, T_0) \sim 1$. The degree of polarization from a cloud of anisotropic electrons with $\Delta = 0.25$ at $T_0 = 8$ KeV is shown in Fig. 4.3 in black for a general bi-Maxwellian distribution, and in red in the linear approximation [equation (4.27)]. We see that the linear approximation holds at least up to $\Delta \approx 0.25$.

4.3 Application to cold fronts and shocks in the ICM

4.3.1 Qualitative estimates

Cold fronts are sharp discontinuities of temperature and density seen in X-rays in a number of clusters (Markevitch et al., 2000; Ettori & Fabian, 2000; Vikhlinin et al., 2001; Markevitch & Vikhlinin, 2007). These are commonly associated with a flow of the hot ambient ICM plasma around a cold subcluster moving in the host cluster nearly at the virial speed. The plasma flow produces draping of the frozen-in magnetic-field lines over the cold cloud (e.g., Lyutikov, 2006; Asai et al., 2007; Dursi & Pfrommer, 2008). Near the front, the flow is essentially a convergence flow, and the field lines are continuously stretched along the interface. This leads to perpendicular orientation of the field lines and temperature gradient and likely inhibits thermal conduction, preserving the sharp gradient between the cold cloud and hot ICM over dynamically long times (e.g., Vikhlinin & Markevitch, 2002).

The field-line stretching should naturally produce pressure anisotropy. In Section 4.2.1, we made simple estimates of the degree of pressure anisotropy for a sonic flow of plasma. These depend on three parameters: the collisional mean free path λ , the characteristic scales of the flow L_u and the parallel temperature gradient L_T . Let us now estimate the typical electron anisotropy induced by the magnetic-field evolution at the interface of a cold front. Because the subcluster is moving at around the virial speed, the flow of the hot ICM in the comoving frame is nearly sonic. From equation (4.11) with $u \sim v_{\text{th},i}$, we get $\Delta_B \sim (1/40)\lambda/L_u \sim 2 \times 10^{-3}$, where for cold fronts, the electron mean free path $\lambda \sim 20$ kpc ($T \sim 8$ keV), and the flow scale $L_u \sim 200$ kpc [of order the size of the subcluster, e.g., A3667 (Markevitch & Vikhlinin, 2007)]. The degree of polarization is a few times smaller than the anisotropy level, because the coherently anisotropic plasma occupies only a fraction of volume of the X-ray emitting ICM. Below, we investigate the

amount of electron anisotropy, the corresponding bremsstrahlung polarization, and their spatial patterns in cold fronts first by means of the simplest analytical model of magnetic-field-line draping (Section 4.3.2), and then by numerical MHD simulations of cold fronts with anisotropic thermal conduction (Section 4.3.3). We also estimate the ion anisotropy for the simulated cold fronts in Appendix 4.6.

4.3.2 Analytical model of magnetic-field-line draping

The problem of the stationary MHD flow of a plasma with a frozen-in magnetic field around a spherical body was first solved analytically by Bernikov & Semenov (1979). They disregarded the magnetic-field back-reaction and assumed a velocity field described by the potential flow of an incompressible irrotational fluid around a sphere. Here we briefly summarize their derivation and use the resulting magnetic field near the body to calculate the electron pressure anisotropy and thermal bremsstrahlung polarization.

In spherical coordinates with the origin at the center of the sphere of radius R and the z axis antiparallel to the fluid velocity v_0 at infinity, the potential flow around the sphere is

$$\mathbf{v} = \mathbf{e}_r \left(\frac{R^3}{r^3} - 1 \right) v_0 \cos \theta + \mathbf{e}_\theta \left(\frac{R^3}{2r^3} + 1 \right) v_0 \sin \theta. \quad (4.28)$$

The magnetic field is obtained by solving the stationary ideal MHD equations

$$\nabla \times (\mathbf{v} \times \mathbf{B}) = 0, \quad \nabla \cdot \mathbf{B} = 0, \quad (4.29)$$

with a homogeneous magnetic field B_0 along the y axis at infinity in the left-half space ($z < 0$) as the boundary condition. We are primarily interested in the approximate solution near the sphere ($r - R \ll R$), where stretching of the field lines is greatest. It reads

$$\begin{aligned} B_r &= \frac{2}{3} B_0 \sqrt{3(r/R - 1)} \frac{\sin \theta}{1 + \cos \theta} \sin \phi, \\ B_\theta &= B_0 \frac{\sin \phi}{\sqrt{3(r/R - 1)}}, \\ B_\phi &= B_0 \frac{\cos \phi}{\sqrt{3(r/R - 1)}}. \end{aligned} \quad (4.30)$$

The velocity and magnetic fields are shown in the left panel of Fig. 4.4.

We can now apply equation (4.10), where only the first term on the right-hand side has to be kept, to calculate the electron anisotropy Δ . The term Δ_n is zero because the flow is incompressible. The heat-flux contribution to electron anisotropy Δ_T is also zero because in our configuration, the cold cloud is completely isolated from the hot ambient plasma by the the draped field lines. We choose to ignore the temperature variations of the incompressible gas outside the sphere and assume homogeneous temperature, because these variations are clearly overstated due to the artificial assumption of constant density. Then,

$$\Delta = \Delta_B = \frac{\gamma}{\nu_e}. \quad (4.31)$$

From the induction equation, we obtain the rate of stretching of the field lines γ :

$$\gamma \equiv \frac{1}{B} \frac{dB}{dt} = \mathbf{b}\mathbf{b} : \nabla \mathbf{v}, \quad (4.32)$$

where $\mathbf{b} = \mathbf{B}/B$ is the unit vector in the direction of the magnetic field. The electron collision frequency (Spitzer, 1962) in a hydrogen plasma is

$$\nu_e \approx 3 \times 10^{-6} \text{ yr}^{-1} \left(\frac{T_e}{8 \text{ keV}} \right)^{3/2} \left(\frac{n_e}{10^{-3} \text{ cm}^{-3}} \right)^{-1}. \quad (4.33)$$

We take the radius of the sphere $R = 200 \text{ kpc}$, temperature $T_0 = 8 \text{ keV}$ and particle density $n_0 = 10^{-3} \text{ cm}^{-3}$ as fiducial parameters. Let us set the flow velocity at infinity v_0 to the speed of sound $c_{s0} = (\gamma_{\text{gas}} p_0 / \rho_0)^{1/2} \approx 1400 \text{ km s}^{-1}$. Combining equations (4.28)–(4.33), we can calculate the electron anisotropy Δ . It is shown in the middle panel of Fig. 4.4 in the central yz cross section. Its value agrees well with the previous qualitative estimate in Section 4.3.1.

The final step is to obtain the polarization of thermal bremsstrahlung from the linear approximation (4.27), which is, indeed, satisfied for our typical values of electron anisotropy $\Delta \sim (1-5) \times 10^{-3}$. We only consider the case of sufficiently energetic photons ($\epsilon \sim 2-3 T_e$) in the hard X-ray range to ignore the photon-energy/electron-temperature dependence and assume $G \sim 1$ in equation (4.27). To obtain the polarization map, we need to integrate equation (4.27) weighted with the thermal bremsstrahlung emissivity κ_{br} ,

$$\kappa_{\text{br}} \propto n_e^2 T_e^{-1/2} \exp(-\epsilon/T_e), \quad (4.34)$$

along the line of sight ², taking into account the rotation of the polarization vectors due to the changing orientation of the magnetic field. Here, and in what follows, we simply assume that the X-ray emitting volume is restricted to a cubic region of size $5R = 1 \text{ Mpc}$, ignoring the effects of the geometry of the host cluster and the location of the cold front inside the host cluster. This should not change our results qualitatively, only introducing a large-scale factor of order unity to the anisotropy and polarization degree. Because the plasma flow is incompressible in our toy model, and its temperature is taken to be homogeneous, the emissivity is a constant outside the sphere. We choose the x -axis as the direction of the line of sight, because in this direction, the polarization is greatest, and xy as the reference plane. We have to integrate both of the independent linear polarization types, P_1 and P_2 , where P_1 is the polarization measured in the vector basis $(\hat{\mathbf{e}}_y, \hat{\mathbf{e}}_z)$, and P_2 measured in the basis rotated by $\pi/4$ from $(\hat{\mathbf{e}}_y, \hat{\mathbf{e}}_z)$. The local polarizations $P_{1,\text{loc}}$ and $P_{2,\text{loc}}$ relative to the reference plane xy are expressed in terms of polarization $P_{B,\text{loc}}$ [equation (4.27)] relative to the plane spanned by the local magnetic-field direction and the line of sight (x -axis):

$$P_{1,\text{loc}} = P_{B,\text{loc}} \cos(2\zeta), \quad (4.35)$$

$$P_{2,\text{loc}} = P_{B,\text{loc}} \sin(2\zeta), \quad (4.36)$$

²The exact temperature dependence may be slightly different if the correct form of the gaunt factor is adopted, but it practically does not affect our results because of small temperature variations outside of the cold cloud.

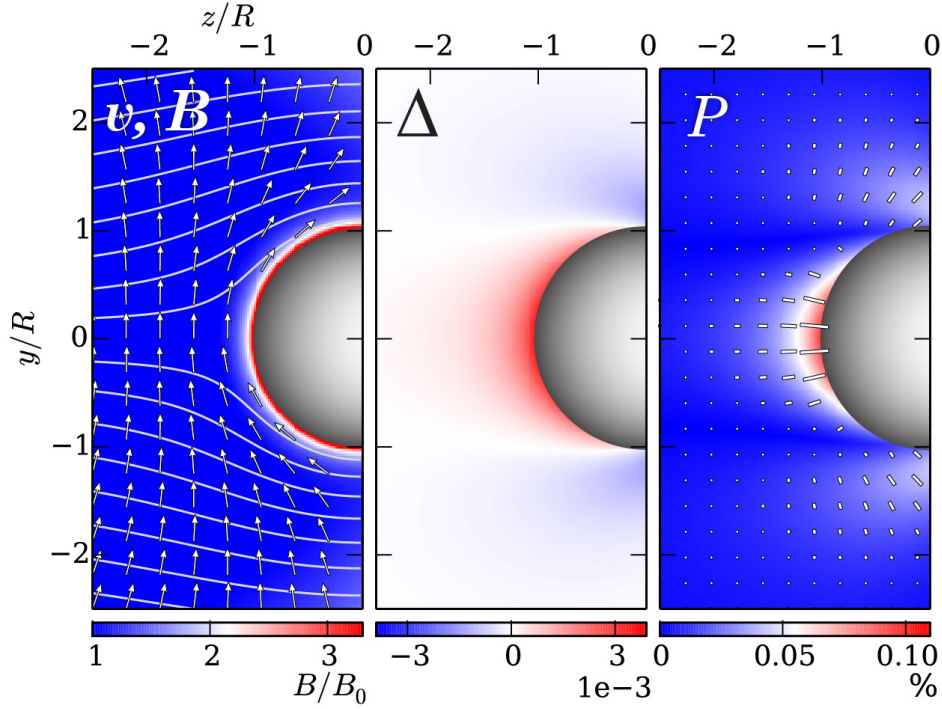


Figure 4.4: Generation of pressure anisotropy and thermal bremsstrahlung polarization during kinematic draping of magnetic-field lines around a spherical body. The velocity field is the potential flow of an incompressible fluid around a sphere [equation (4.28)]. The magnetic field is an approximate solution of the ideal kinematic MHD equations near the sphere [equations (4.30)]. The left and middle panels are the central yz cross sections. Left: the magnetic-field strength B (color) in the units of B at infinity, B_0 ; superimposed are the velocity field stream lines (contours) and the unit vectors in the direction of the magnetic field (arrows). Middle: the electron pressure anisotropy generated by stretching of the field lines by the flow. Right: the degree (color) and direction (line segments) of the polarization of thermal bremsstrahlung in the yz plane (as seen along the line of sight coincident with the x -axis).

where ζ the angle between the projection of the magnetic field onto the yz plane and the y axis. Using equation (4.27) for $P_{B,\text{loc}}$ and integrating the local polarization along the line of sight, we get

$$P_1 = \frac{\int \Delta \sin^2 \theta \cos(2\zeta) \kappa_{\text{br}} dx}{\int \kappa_{\text{br}} dx}, \quad (4.37)$$

$$P_2 = \frac{\int \Delta \sin^2 \theta \sin(2\zeta) \kappa_{\text{br}} dx}{\int \kappa_{\text{br}} dx}, \quad (4.38)$$

where θ is the angle between the local magnetic field and the line of sight [as in equation (4.27)]. The angles θ and ζ can be expressed in terms of the components of the unit vector in the direction of the field \mathbf{b} :

$$\cos 2\zeta = (b_y^2 - b_z^2)/(b_y^2 + b_z^2), \quad (4.39)$$

$$\sin^2 \theta = 1 - b_x^2. \quad (4.40)$$

The total linear polarization P is

$$P = (P_1^2 + P_2^2)^{1/2}. \quad (4.41)$$

The polarization position angle relative to $\hat{\mathbf{e}}_y$ is set by angle ψ ,

$$\psi = \frac{1}{2} \text{atan} \frac{P_2}{P_1}. \quad (4.42)$$

The resulting thermal bremsstrahlung polarization pattern is shown in the right panel of Fig. 4.4, where color indicates the degree of polarization, and line segments the position angles [calculated by equation (4.42)] in the yz plane. The characteristic degree of polarization is $\sim 0.1\%$. If we integrate the polarization along a line of sight at angle $\theta' \neq 0$ to the x -axis instead, the effect becomes a factor of $\cos^2 \theta'$ smaller from the form of equations (4.37) and (4.38).

4.3.3 MHD simulations of cold fronts

Description of the code and setup

To simulate cold fronts for the purpose of this work, we use an MHD code based on the van Leer integrator combined with the constrained transport (CT) approach (see Stone & Gardiner 2009 for a description of the numerical method). Anisotropic thermal conduction was implemented via a semi-implicit directionally split scheme with a monotized central (MC) limiter applied to the conductive fluxes to avoid negative temperatures (Sharma &

Hammett, 2011). The set of equations solved is

$$\frac{\partial \rho}{\partial t} + \nabla \cdot (\rho \mathbf{v}), \quad (4.43)$$

$$\frac{\partial \rho \mathbf{v}}{\partial t} + \nabla \cdot \left(\rho \mathbf{v} \mathbf{v} - \frac{\mathbf{B} \mathbf{B}}{4\pi} \right) + \nabla p = \rho \mathbf{g}, \quad (4.44)$$

$$\frac{\partial E}{\partial t} + \nabla \cdot \left[\mathbf{v}(E + p) - \frac{\mathbf{B}(\mathbf{v} \cdot \mathbf{B})}{4\pi} \right] = \rho \mathbf{g} \cdot \mathbf{v} - \nabla \cdot Q, \quad (4.45)$$

$$\frac{\partial \mathbf{B}}{\partial t} = \nabla \cdot (\mathbf{v} \mathbf{B} - \mathbf{B} \mathbf{v}), \quad (4.46)$$

where

$$p = p_{\text{th}} + \frac{B^2}{8\pi}, \quad (4.47)$$

$$E = \frac{\rho v^2}{2} + \varepsilon + \frac{B^2}{8\pi}, \quad (4.48)$$

$$Q = -\kappa_{\parallel} \mathbf{b} \mathbf{b} : \nabla T, \quad (4.49)$$

where p_{th} is the gas pressure, ε the internal energy of the plasma per unit volume, \mathbf{g} the gravitational acceleration, and Q the heat flux along the field lines with parallel thermal conductivity κ_{\parallel} . The plasma is described by an ideal equation of state with $\gamma_{\text{gas}} = 5/3$ and mean molecular weight $\mu = 0.6$. We take the fiducial value of $\kappa_{\parallel} = \kappa_{\text{Sp}}$, where κ_{Sp} is the Spitzer thermal conductivity for an unmagnetized plasma (Spitzer, 1962). We ignore any potential mechanisms whereby parallel thermal conduction might be suppressed (e.g., magnetic mirrors; Chandran & Cowley 1998; Komarov et al. 2016, or electron kinetic instabilities, Riquelme et al. 2016), as we are looking for an upper estimate of the polarization effect.

We initialize a 3D region of hot dilute plasma ($T_{\text{out}} = 8$ keV, $n_{\text{out}} = 10^{-3}$ cm $^{-3}$) of spatial extent $L = 1$ Mpc with a cold spherical subcluster ($T_{\text{in}} = 4$ keV) of radius $R = 200$ kpc embedded at the center. The distribution of density inside the cold cloud is described by a beta model,

$$n_{\text{in}} = n_c [1 + (r/r_c)^2]^{-3\beta'/2}, \quad (4.50)$$

with $\beta' = 2/3$, core radius $r_c = R/\sqrt{3} \approx 115$ kpc, and central density $n_c = 8n_{\text{out}}$. The gravitational acceleration, \mathbf{g} , models the effect of a static dark matter halo at the center of the computational domain, and is set to balance the initial pressure gradient inside the subcluster. The edge of the subcluster at $r = R$ is a contact discontinuity: the temperature experiences a factor of two jump in the direction of the hot ambient plasma, while the density decreases by a factor of 2 to keep the pressure continuous. The problem is solved in the frame comoving with the subcluster. Initially, the cold cloud is at rest, while the velocity of the surrounding gas v_0 is set to the sound speed in the hot ambient plasma, $c_{s0} = (\gamma_{\text{gas}} p_{\text{out}} / \rho_{\text{out}})^{1/2} = (\gamma_{\text{gas}} k T_{\text{out}} / \mu m_p)^{1/2} \approx 1400$ km s $^{-1}$. This setup is similar to the one used by Asai et al. (2007).

To make estimates of the bremsstrahlung polarization generated by electron pressure anisotropy due to stretching of the magnetic-field lines and to heat fluxes, we analyze the results of two runs with different structure of the magnetic field. In both runs, the initial plasma $\beta = 200$. The first run is initialized with a homogeneous magnetic field along the y -axis, perpendicular to the cold cloud velocity. The initial magnetic field in the second run is random with a Gaussian distribution and correlation length $l_B = L/10 \approx 100$ kpc. We note that the statistics of magnetic fields in galaxy clusters are unlikely to be Gaussian, and the reported values of the correlation length inferred from the Faraday rotation observations are about an order of magnitude smaller (e.g., Vogt & Enßlin, 2005). Therefore, this run is merely illustrative, and demonstrates only qualitative differences between cases with uniform and tangled magnetic field.

Results for the case of a homogeneous magnetic field

The central yz cross sections of the plasma temperature T , velocity field \mathbf{v} and magnetic field \mathbf{B} are shown in the top-left and middle-top panels of Fig. 4.5 at time $t \approx 0.3$ Gyr. The anisotropy pattern at the cold front interface is similar to the one in the analytical model of the field-line draping (top-right panel of Fig. 4.5), with the typical magnitude of the anisotropy $\Delta \sim 10^{-3}$. Using the continuity and induction equations, we can express the degree of anisotropy produced by the field-line stretching and compression of the gas as

$$\Delta_B + \Delta_n = \frac{1}{\nu_e} \left(\mathbf{b}\mathbf{b} : \nabla\mathbf{v} - \frac{1}{3}\nabla \cdot \mathbf{v} \right).$$

Compression contributes via the divergence of the velocity field $\nabla \cdot \mathbf{v}$. Because $\nabla \cdot \mathbf{v}$ is positive ahead of the subcluster, the electron anisotropy at the interface is reduced compared to the incompressible model. The sharp boundary of the anisotropy pattern ahead of the front is due to a discontinuity in the static gravitational acceleration, which is set to zero outside the sphere of radius R . This does not affect our estimate of the degree of polarization and of the size of the polarized region. Because the magnetic field points in the y -direction initially, the heat flux across the interface is fully suppressed, while in the regions where the orientation of the field lines is not perfectly perpendicular to the temperature gradients, the heat flux contribution is noticeable (see the bottom-left panel of Fig. 4.5).

The new features of the simulated cold front, compared to the simplistic analytical model studied in Section 4.3.2, are the presence of a weak bow shock in front of the subcluster and the formation of turbulent vortices that efficiently amplify the magnetic field behind the subcluster. Let us analyze them in more detail.

At the moment of taking the snapshot shown in Fig. 4.5 ($t \approx 0.3$ Gyr), the bow shock is slowly receding from the cold front at the speed $u_{\text{sh}} \approx 250$ km/s. Let us first discuss the contribution to the anisotropy at the shock brought in by the compression of the gas. The source of the anisotropy is the jump of the normal velocity and the tangential component of the magnetic field at the shock close to the z -axis. The passage of the shock amplifies the y -component of the magnetic field in the downstream flow. From equation (4.51), with

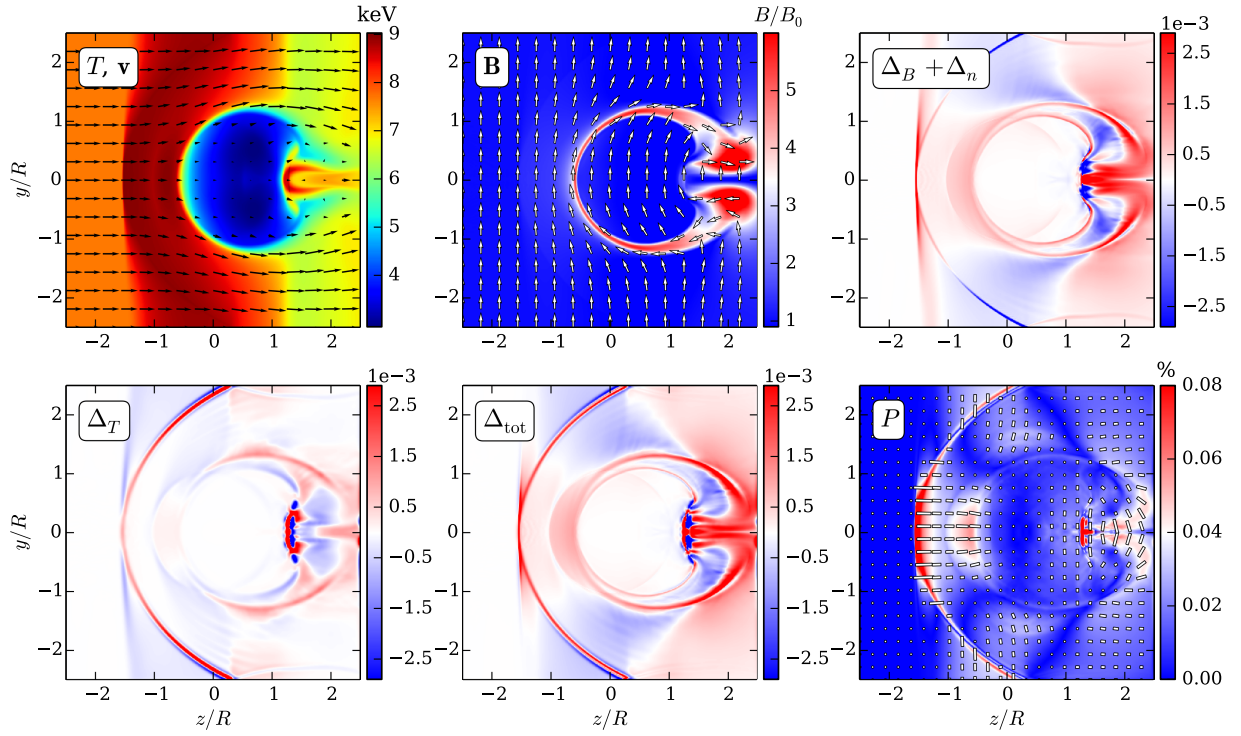


Figure 4.5: A simulation of a cold front with a homogeneous initial magnetic field along the y -direction. All the panels except for the bottom right are the central yz cross sections at time $t \approx 0.3$ Gyr. The top-left panel shows the temperature map (color) and the velocity field (arrows). The magnetic field \mathbf{B} is shown in the top-middle panel (color: field strength; arrows: unit vectors in the magnetic-field direction). The different components of the electron anisotropy and the total anisotropy are demonstrated in the top-right, bottom-left, and bottom-middle panels. The bottom-right panel shows the resulting polarization map integrated along the line of sight (the x -direction).

$\mathbf{bb} : \nabla \mathbf{v} = 0$ (close to the z -axis, the velocity only changes in the direction perpendicular to the field lines), we can estimate the anisotropy $\Delta_B + \Delta_n$ at the shock:

$$\Delta_{B,\text{sh}} + \Delta_{n,\text{sh}} \sim -10^{-2} \frac{v_{z,d} - v_{z,u}}{c_{s0}} \frac{\lambda}{\delta}, \quad (4.51)$$

where $v_{z,u}$ and $v_{z,d}$ are the up- and downstream normal velocities, δ the width of the shock, and λ the electron mean free path. The normal velocity discontinuity contributes to the electron anisotropy via the non-zero velocity divergence. The upstream velocity is the speed of sound, $v_{z,u} = v_0 = c_{s0}$, while the normal velocity jump in the frame of the shock from the Rankine-Hugoniot conditions (consider the magnetic field dynamically unimportant) is

$$\frac{v_{z,d} + u_{\text{sh}}}{v_{z,u} + u_{\text{sh}}} = \frac{(\gamma_{\text{gas}} + 1)M_1^2}{(\gamma_{\text{gas}} - 1)M_1^2 + 2} \approx 0.8, \quad (4.52)$$

where $M_1 = (v_{z,u} + u_{\text{sh}})/c_{s0} \approx 1.18$ is the Mach number of the upstream gas in the frame of the shock. Then, we can infer the velocity jump in laboratory frame $v_{z,d}/v_{z,u} \approx 0.8$. Taking the shock width $\delta \sim \lambda$, from equation (4.51), we estimate the typical value of anisotropy at the shock $\Delta_{B+n,\text{sh}} \approx 2 \times 10^{-3}$. Results of the numerical simulations agree well with this estimate (see the top-right panel of Fig. 4.5). At angles larger than $\pi/4$ from the z -axis, the term $\mathbf{bb} : \nabla \mathbf{v} \approx b_y^2 \partial_y v_y < 0$ starts to dominate at the shock, because there is a jump in the y -velocity parallel to the field lines, and the magnetic field is compressed along the y -direction producing negative electron anisotropy.

Close to the z -axis, the magnetic field is perpendicular to the temperature gradient, and there is no heat flux across the shock. However, away from the z -axis, the magnetic field only partly impedes thermal conduction. Although the strong parallel conductivity smears the temperature gradient, a small jump of the temperature and its gradient along the shock is still left behind. The jump $\delta T/T$ is of the order of 0.5 %, and the level of positive anisotropy it generates is of the same order, because, from equation (4.12), $\Delta_T \sim (\lambda/L_T)^2 \delta T/T$ (we took $L_u = L_T$ because the heat flux changes at the scale of the shock width, as well as the temperature). The scale of the gradient L_T is of the order of the shock width, which can be approximated by the mean free path λ . Then, the anisotropy is simply $\Delta_T \sim \delta T/T \sim 0.5$ %. This is seen in the bottom-left panel of Fig. 4.5.

Another notable feature of the simulated cold front is the amplification of the magnetic field behind the subcluster (middle-top panel of Fig. 4.5), previously reported by Asai et al. (2007). The amplification is caused by stretching of the field lines along the z -direction by the vortices generated by the flow of the ambient gas around the subcluster. The magnetic field is amplified more efficiently than at the cold front interface, because the vortices are smaller than the subcluster, and thus produce a velocity strain rate larger than that ahead of the subcluster by a factor of the ratio of the subcluster size to the size of the vortices. Therefore, they are expected to generate more electron anisotropy, which is clearly seen in the top-right panel of Fig. 4.5.

The total electron anisotropy is shown in the middle-bottom panel of Fig. 4.5. The corresponding polarization of thermal bremsstrahlung is calculated by equations (4.34)-

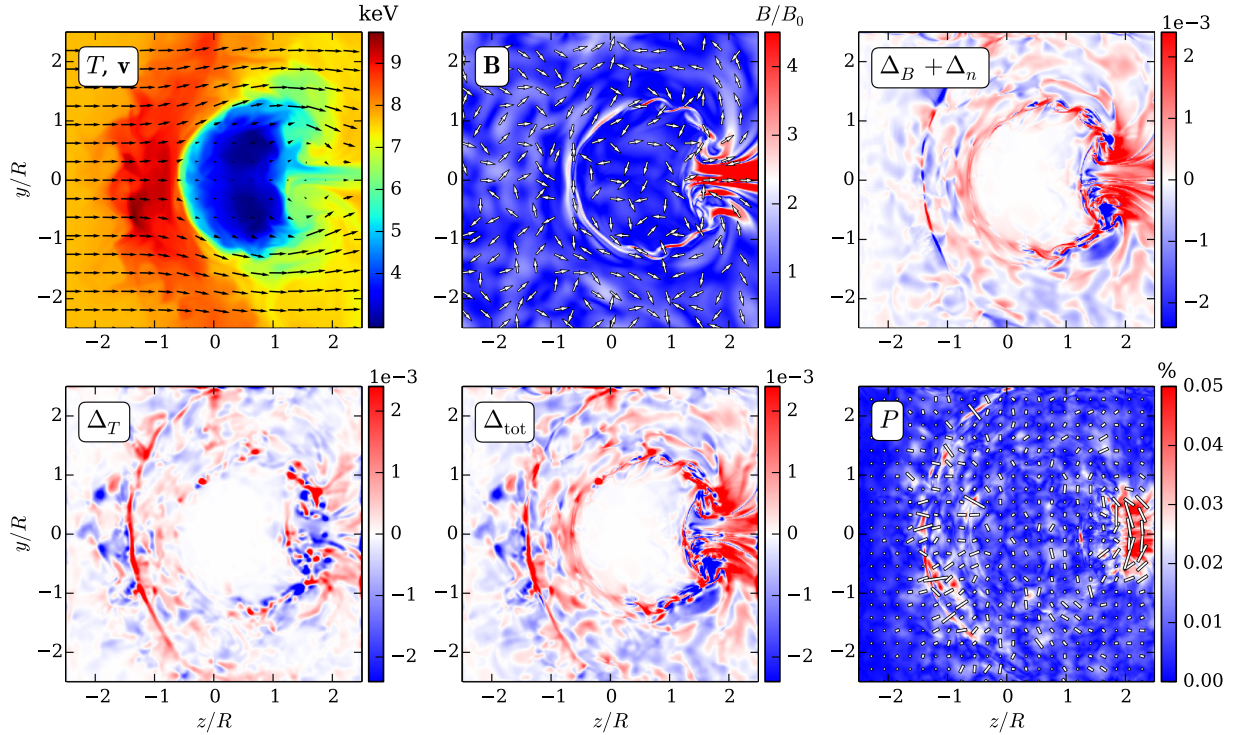


Figure 4.6: A simulation of a cold front with a random Gaussian initial magnetic field with correlation length $l_B \approx 100$ kpc. The panels show the same quantities as in Fig. 4.5.

(4.42), now taking account of the spatial variation of the bremsstrahlung emissivity [equation (4.34)], and demonstrated in the bottom-right panel of Fig. 4.5. The polarization is generally dominated by stretching of the field lines and the compressibility effects. There are three regions, where the degree of polarization is at $\sim 0.1\%$ level: (1) at the cold-front interface due to stretching of the field lines in the y direction; (2) at the bow shock close to the z axis due to the compressibility term in equation (4.51); and (3) behind the subcluster due to amplification of the magnetic field along the z direction by the turbulent vortices.

Results for the case of a random magnetic field

It is currently believed (based on numerical and indirect observational evidence) that the ICM is turbulent (see, e.g., Inogamov & Sunyaev 2003; Schuecker et al. 2004; Schekochihin & Cowley 2006; Subramanian et al. 2006; Zhuravleva et al. 2014), and therefore, the magnetic fields in the ICM are tangled by random motions of the plasma. Here, we model the effect of the random topology of the field lines by generating a random Gaussian magnetic field with correlation length $l_B = 100$ kpc. The mean plasma $\beta = 2p_{\text{out}}/\langle B^2 \rangle = 200$, where $\langle B^2 \rangle = B_0^2$. Analogously to the case of a homogeneous magnetic field, the results of our simulations are shown in Fig. 4.6. The random field topology diminishes the electron anisotropy produced by stretching of the field lines at the cold-front interface (top-right

panel of Fig. 4.6) and almost completely wipes out its contribution to the total polarization (see the bottom-right panel). We should remark that due to numerical diffusivity, during compression and stretching of the field-line loops by the convergence flow at the front, the opposite orientations of the field may reconnect, thus, modifying the field-line topology in the region where one expects to see electron anisotropy. Therefore, our numerical estimate in this region might be understated.

Because now the field-line orientation at the bow shock is random, in addition to the compression term [equation (4.51)], the heat fluxes also positively contribute to the total anisotropy everywhere across the shock (see the bottom-left panel of Fig. 4.6). The level of electron anisotropy generated by the turbulent vortices behind the shock is practically unchanged compared to the simulation with a homogeneous magnetic field. In a random magnetic field, this mechanism appears to be the most efficient.

The resulting polarization map (bottom-right panel) indicates as follows. (1) Polarization at the cold-front interface is practically indiscernible. (2) The degree of polarization at the shock is $\sim 0.05\%$. (3) The largest polarization, $\sim 0.1\%$, is achieved behind the cold cloud via the magnetic-field amplification by the turbulent backflow.

4.4 Discussion

At present, the only astrophysical object from which a polarized signal has been reliably detected in X-rays below 10 keV is the Crab nebula (Weisskopf et al., 1978), dating back to the 70s. The progress with the development of the new generation of X-ray polarimeters (e.g., Soffitta et al., 2013; Weisskopf et al., 2013; Jahoda et al., 2014) has led to a dramatic increase of the expected sensitivity that could open a new observational window into a variety of astrophysical objects. Magnetars, radio and accreting X-ray pulsars, reflected radiation in X-ray binaries or AGNs are all among the promising targets for missions like XIPE, IXPE and PRAXyS.

In the majority of those objects, polarization is either associated with non-thermal emission (e.g., synchrotron radiation of relativistic electrons) or with scattering in aspherical geometries. Here, we discuss the polarization of *thermal* emission from the hot gas in galaxy clusters. This is an interesting question for at least two reasons: (i) clusters of galaxies are considered as possible unpolarized targets for calibration purpose and (ii) weak polarization of thermal bremsstrahlung potentially could serve as a proxy for the plasma properties on extremely small scales, not directly resolvable with the current or future X-ray missions.

As we showed in the previous sections, the polarization of thermal bremsstrahlung naturally arises from the anisotropy of the electron distribution function driven by stretching of the magnetic-field lines and/or temperature gradients along the field. Pitch-angle scattering of the electrons controls the level of anisotropy, and even if it is set purely by Coulomb collisions, the anisotropy is always small. Further reduction of the observed polarization signal is expected if many uncorrelated regions with varying orientation of anisotropy are present along the line of sight, leading to effective averaging of the signal. From this point

of view, the most promising are the configurations with a large-scale flow that provides a coherence of structures and drives the anisotropy. Our qualitative estimates show that the expected degree of polarization is close to 0.1% for rather idealized configurations that exhibit shocks and cold fronts.

It is worth noting that aside from polarizing thermal bremsstrahlung electron pressure anisotropy is also capable of producing a small degree of polarization of the Sunyaev-Zeldovich (SZ) signal (Sunyaev & Zeldovich, 1980) and the emission in collisionally-excited X-ray lines (e.g., He-like triplets of silicon, sulphur and iron; see Pal'chikov & Shevelko 1995, and references therein). However, these two effects are both subjected to somewhat higher possible contamination, coming from the Thomson scattering of cluster central AGN radio emission and the contribution of the kinetic SZ effect in the first case (Sunyaev & Zeldovich, 1980; Sazonov & Sunyaev, 1999; Diego et al., 2003), and resonant-scattering-induced polarization in the latter case (Sazonov et al., 2002; Zhuravleva et al., 2010).

The small degree of polarization makes galaxy clusters a suitable (unpolarized) calibration target for the forthcoming generation of X-ray polarimeters. We note in passing that two other mechanisms could also contribute to the polarization of thermal emission of the hot gas in clusters. One is Thomson scattering of centrally concentrated X-ray emission by the electrons; another is resonant scattering of emission-line photons (Sazonov et al., 2002; Zhuravleva et al., 2010). Both effects have a clear signature of the polarization plane being perpendicular to the direction towards the cluster center and are expected to disappear if the integrated signal (over a circular region around the cluster center) of a relaxed cluster is used. Even if an offset region is considered, one can crudely estimate the expected level of polarization. Given that the Thomson optical depth in clusters is at the level of 10^{-3} , the scattered thermal emission should not be polarized by more than a fraction of this value. For resonant lines, the optical depth is larger, but the effect is confined to line photons and does not affect the continuum. On the whole, clusters are suitable calibration objects for IXPE, XIPE, or PRAXyS.

Nevertheless, if future polarimeters with capabilities well beyond currently developed instruments could detect polarization from carefully selected clusters with a large-scale substructure, it would imply that one has a way to constrain the effective collisionality of electrons. Of course, clusters of galaxies are not the only objects where polarization of thermal emission could be present. As an example one could consider hot radiatively inefficient flows around black holes or neutron stars that might have conditions suitable for generation of sufficient electron anisotropy. We defer this question to further studies.

4.5 Conclusions

We have studied the effect of polarization of thermal bremsstrahlung emission in a weakly collisional astrophysical plasma due to (small) electron pressure anisotropy. Stretching of the magnetic-field lines by a flow of plasma, compression, or the presence of heat fluxes all lead to generation of pressure anisotropy in a plasma, where the Larmor radii of the charged particles are much smaller than their mean free paths. In the case of ordered plasma

motions with a certain preferred direction, electron anisotropies may produce polarization of thermal bremsstrahlung emission. The degree of polarization is a few times lower than the anisotropy level (depending on the size of the region of coherently anisotropic electrons and on the bremsstrahlung photon energy).

We have estimated the upper bounds on the degree of polarization in cold fronts in the ICM as they represent a perfect example of converging flows and large temperature gradients. Cold fronts may also be associated with additional features (although not always observed), such as bow shocks, or turbulent vortices generated behind subclusters. We have found that a small polarization, at $\sim 0.1\%$ level, can be generated by either the converging flow, the weak bow shock, or the vortices behind the cold front. Although at the moment, such a small degree of bremsstrahlung polarization at energies of a few kT cannot be observed, future observations of this effect might provide a valuable insight into the generation of pressure anisotropies in astrophysical plasmas. The absence of polarization at the estimated level could also set lower limits on electron collisionality in the ICM, which may be enhanced by scattering off microscale magnetic fluctuations (Riquelme et al., 2016) or magnetic trapping by the mirror instability at the scale of the ion Larmor radius (Komarov et al., 2016).

4.6 Appendix A: ion anisotropy

Here, for illustrative purposes, we calculate the ion anisotropy Δ_i by equation (4.10) for the two simulated cold fronts with homogeneous and random magnetic fields. As it is seen in Fig. 4.7, the ion anisotropy is large enough to trigger the firehose and mirror instabilities all over the computational domain. The plasma is rendered unstable when $|\Delta_i| \gtrsim 1/\beta$. The instabilities maintain the plasma in the marginal state: $\Delta_i = 1/\beta$ for the mirror, $\Delta_i = -2/\beta$ for the firehose instabilities. In some regions, β becomes low and allows a rather high level of anisotropy, while keeping the plasma stable. In the case of a homogeneous magnetic field, this is clearly seen in the low- β layer around the cold front and behind the front, where the magnetic field is amplified by turbulent eddies. In the case of a random magnetic field, stable regions of high anisotropy form behind the front.

4.7 Appendix B: differential cross sections for relativistic bremsstrahlung

The expressions for the relativistic bremsstrahlung differential cross sections were first given by Gluckstern & Hull (1953). After being rearranged in a more convenient way (Bai & Ramaty, 1978) and corrected for typos, they read

$$d^2\sigma_{\perp} = A \left(B_{\perp} + \frac{L}{pp'} C_{\perp} + \frac{l_0}{p'Q} D_{\perp} - \frac{E}{p^2 \sin^2 \theta} \right), \quad (4.53)$$

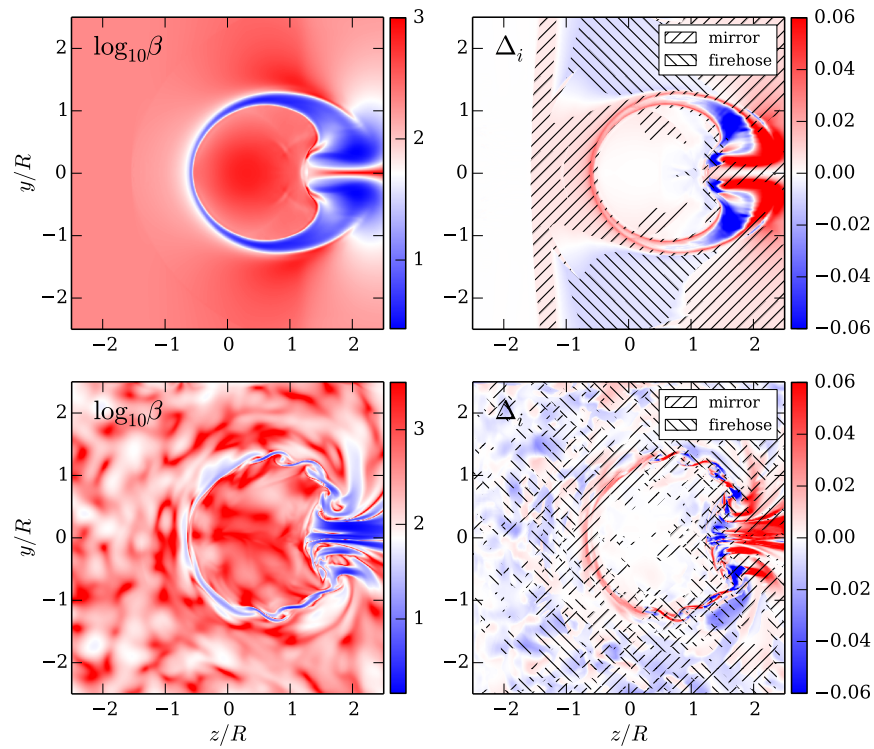


Figure 4.7: The ion anisotropy for the simulated cold fronts. Left panels: the plasma β . Right panels: the ion anisotropy Δ_i , unstable regions are hatched; in the unstable regions, the plasma is kept marginal: $\Delta_i = 1/\beta$ for the mirror, $\Delta_i = -2/\beta$ for the firehose instabilities.

$$d^2\sigma_{\parallel} = A \left(\tilde{B}_{\parallel}(\theta) + \frac{L}{pp'} \tilde{C}_{\parallel}(\theta) + \frac{l_0}{p'Q} D_{\parallel} + \frac{E}{p^2 \sin^2 \theta} \right), \quad (4.54)$$

$$A = \frac{Z^2 r_0^2 p' 1}{8\pi 137 p \epsilon}, \quad (4.55)$$

$$B_{\perp} = -\frac{5\gamma^2 + 2\gamma\gamma' + 1}{p^2\delta^2} - \frac{p^2 - k^2}{Q^2\delta^2} - \frac{2k}{p^2\delta}, \quad (4.56)$$

$$B_{\parallel} = -\frac{5\gamma^2 + 2\gamma\gamma' + 5}{p^2\delta^2} - \frac{p^2 - k^2}{Q^2\delta^2} + \frac{2(\gamma + \gamma')}{p^2\delta} - \frac{4l}{p'\delta}, \quad (4.57)$$

$$\tilde{B}_{\parallel}(\theta) = B_{\parallel} + \frac{8(2\gamma^2 + 1)}{p^2\delta^4} \sin^2 \theta, \quad (4.58)$$

$$C_{\perp} = \frac{2\gamma^2(\gamma^2 + \gamma'^2) - (5\gamma^2 - 2\gamma\gamma' + \gamma'^2)}{p^2\delta^2} + \frac{k(\gamma^2 + \gamma\gamma' - 2)}{p^2\delta}, \quad (4.59)$$

$$C_{\parallel} = \frac{2\gamma^2(\gamma^2 + \gamma'^2) - (9\gamma^2 - 4\gamma\gamma' + \gamma'^2) + 2}{p^2\delta^2} + \frac{k(\gamma^2 + \gamma\gamma')}{p^2\delta}, \quad (4.60)$$

$$\tilde{C}_{\parallel}(\theta) = C_{\parallel} + \frac{4\gamma(3k - p^2\gamma')}{p^2\delta^4} \sin^2 \theta, \quad (4.61)$$

$$D_{\perp} = \frac{k}{\delta} - \frac{k(p^2 - k^2)}{Q^2\delta} + 4, \quad (4.62)$$

$$D_{\parallel} = \frac{4}{\delta^2} - \frac{7k}{\delta} - \frac{k(p^2 - k^2)}{Q^2\delta} - 4, \quad (4.63)$$

$$E = \frac{2L}{pp'} \left(2\gamma^2 - \gamma\gamma' - 1 - \frac{k}{\delta} \right) - \frac{4l_0}{p'Q} (\delta - \gamma')^2 - \frac{2l(\delta - \gamma')}{p'}, \quad (4.64)$$

where

$$\gamma = E/m_e c^2 + 1; \quad \gamma' = \gamma - \epsilon/m_e c^2; \quad (4.65)$$

$$p = \sqrt{\gamma^2 - 1}; \quad p' = \sqrt{\gamma'^2 - 1}; \quad k = \epsilon/m_e c^2; \quad (4.66)$$

$$Q^2 = p^2 + k^2 - 2pk \cos \theta; \quad \delta = \gamma - p \cos \theta; \quad (4.67)$$

$$L = 2 \ln \left(\frac{\gamma\gamma' + pp' - 1}{\gamma\gamma' - pp' - 1} \right); \quad l = \ln \left(\frac{\gamma' + p'}{\gamma' - p'} \right); \quad l_0 = \ln \left(\frac{Q + p'}{Q - p'} \right); \quad (4.68)$$

$r_0 = e^2/(m_e c^2) \approx 2.82 \times 10^{-13}$ cm is the classical electron radius, the rest of the notations were introduced in Section 4.2.2.

Bibliography

- Asai N., Fukuda N., Matsumoto R., 2007, *ApJ*, 663, 816
- Axford W. I., Leer E., Skadron G., 1977 Vol. 11, Vol 11, The acceleration of cosmic rays by shock waves. in 15th Proc. Int. Cosm. Ray Conf., p. 132
- Bai T., Ramaty R., 1978, *ApJ*, 219, 705
- Bale S. D., Kasper J. C., Howes G. G., Quataert E., Salem C., Sundkvist D., 2009, *Phys. Rev. Lett.*, 103, 211101
- Bell A. R., 1978, *MNRAS*, 182, 147
- Bernikov L. V., Semenov V. S., 1979, *Geomagn. Aeronomy*, 19, 671
- Blandford R. D., Ostriker J. P., 1978, *ApJ*, 221, L29
- Chandran B. D. G., Cowley S. C., 1998, *Phys. Rev. Lett.*, 80, 3077
- Chandrasekhar S., Kaufman A. N., Watson K. M., 1958, *Proc. R. Soc. A*, 245, 435
- Chew G. F., Goldberger M. L., Low F. E., 1956, *Proc. R. Soc. A*, 236, 112
- Diego J. M., Mazzotta P., Silk J., 2003, *ApJ*, 597, L1
- Dursi L. J., Pfrommer C., 2008, *ApJ*, 677, 993
- Ettori S., Fabian A. C., 2000, *MNRAS*, 317, L57
- Gluckstern R. L., Hull M. H., 1953, *Phys. Rev.*, 90, 1030
- Hasegawa A., 1969, *Phys. Fluids*, 12, 2642
- Haug E., 1972, *Sol. Phys.*, 25, 425
- Hellinger P., Trávníček P., Kasper J. C., Lazarus A. J., 2006, *Geophys. Res. Lett.*, 33, 9101
- Inogamov N. A., Sunyaev R. A., 2003, *Astron. Lett.*, 29, 791

- Jahoda K. M., Black J. K., Hill J. E., Kallman T. R., Kaaret P. E., Markwardt C. B., Okajima T., Petre R., Soong Y., Strohmayer T. E., Tamagawa T., Tawara Y., 2014, in Space Telescopes and Instrumentation 2014: Ultraviolet to Gamma Ray Vol. 9144 of Proc. SPIE, X-ray polarization capabilities of a small explorer mission. p. 91440N
- Kasper J. C., Lazarus A. J., Gary S. P., 2002, *Geophys. Res. Lett.*, 29, 1839
- Komarov S. V., Churazov E. M., Kunz M. W., Schekochihin A. A., 2016, *MNRAS*, 460, 467
- Komarov S. V., Churazov E. M., Schekochihin A. A., ZuHone J. A., 2014, *MNRAS*, 440, 1153
- Krymskii G. F., 1977, *Akademiia Nauk SSSR Doklady*, 234, 1306
- Kulsrud R., 1964, in Rosenbluth M. N., ed., *Advanced Plasma Theory General stability theory in plasma physics*. Academic Press, p. 54
- Lyutikov M., 2006, *MNRAS*, 373, 73
- Markevitch M., Ponman T. J., Nulsen P. E. J., Bautz M. W., Burke D. J., David L. P., Davis 2000, *ApJ*, 541, 542
- Markevitch M., Vikhlinin A., 2007, *Phys. Rep.*, 443, 1
- Melville S., Schekochihin A. A., Kunz M. W., 2016, *MNRAS*, 459, 2701
- Pal'chikov V. G., Shevelko V. P., 1995, *Reference Data on Multicharged Ions*. Vol. 16, Springer-Verlag Berlin
- Parker E. N., 1958, *Phys. Rev.*, 109, 1874
- Riquelme M. A., Quataert E., Verscharen D., 2016, *ApJ*, 824, 123
- Sazonov S. Y., Churazov E. M., Sunyaev R. A., 2002, *MNRAS*, 333, 191
- Sazonov S. Y., Sunyaev R. A., 1999, *MNRAS*, 310, 765
- Schekochihin A. A., Cowley S. C., 2006, *Phys. Plasmas*, 13, 056501
- Schuecker P., Finoguenov A., Miniati F., Böhringer H., Briel U. G., 2004, *A&A*, 426, 387
- Sharma P., Hammett G. W., 2011, *J. Comp. Phys.*, 230, 4899
- Sharma P., Hammett G. W., Quataert E., Stone J. M., 2006, *ApJ*, 637, 952
- Soffitta P., Barcons X., Bellazzini R., Braga J., Costa E., Fraser G. W., Gburek S., Huovelin J., Matt G., Pearce M., Poutanen J., Reglero V., Santangelo A., Sunyaev R. A., Tagliaferri G., 2013, *Experimental Astronomy*, 36, 523

- Spitzer L., 1962, *Physics of Fully Ionized Gases*. Interscience, New York
- Stone J. M., Gardiner T., 2009, *New A*, 14, 139
- Subramanian K., Shukurov A., Haugen N. E. L., 2006, *MNRAS*, 366, 1437
- Sunyaev R. A., Zeldovich I. B., 1980, *MNRAS*, 190, 413
- Vikhlinin A., Markevitch M., Murray S. S., 2001, *ApJ*, 549, L47
- Vikhlinin A. A., Markevitch M. L., 2002, *Astron. Lett.*, 28, 495
- Vogt C., Enßlin T. A., 2005, *A&A*, 434, 67
- Weisskopf M. C., Baldini L., Bellazini R., Brez A., Costa E., Dissly R., Elsner R. F., Fabiani S., Matt G., Minuti M., Muleri F., O'Dell S., Pinchera M., Ramsey B., Rubini A., Sgro' C., Soffitta P., Spandre G., 2013, in *UV, X-Ray, and Gamma-Ray Space Instrumentation for Astronomy XVIII Vol. 8859 of Proc. SPIE*, A small mission featuring an imaging x-ray polarimeter with high sensitivity. p. 885908
- Weisskopf M. C., Silver E. H., Kestenbaum H. L., Long K. S., Novick R., 1978, *ApJ*, 220, L117
- Zhuravleva I., Churazov E., Schekochihin A. A., Allen S. W., Arévalo P., Fabian A. C., Forman W. R., Sanders J. S., Simionescu A., Sunyaev R., Vikhlinin A., Werner N., 2014, *Nature*, 515, 85
- Zhuravleva I. V., Churazov E. M., Sazonov S. Y., Sunyaev R. A., Forman W., Dolag K., 2010, *MNRAS*, 403, 129

Chapter 5

Conclusions

The intracluster medium (ICM) is a multiscale turbulent magnetized environment, which is subjected to a broad range of physical processes. A complete self-consistent description of the ICM is practically impossible because of an enormous scale separation of the effects involved. A magnetic field affects the properties of the ICM in several ways. First, it may alter the plasma dynamics via the Lorenz forces, because the magnetic-energy density in the ICM, estimated by Faraday rotation measurements, is comparable with the kinetic energy of turbulent motions, estimated by analyzing the X-ray surface brightness fluctuations in clusters. Second, magnetic fields dramatically modify transport processes: viscosity and thermal conduction. Because the charged particles gyrate in the cluster magnetic fields with the Larmor radii many orders of magnitude smaller than their mean free paths, heat and momentum transfer become highly anisotropic. Finally, and, perhaps, most importantly, the ICM is a weakly collisional plasma, in which adiabatic invariance drives pressure anisotropies. These anisotropies, even at a percent level, inevitably lead to development of kinetic microinstabilities. The instabilities further modify the ICM particle transport by particle scattering off Larmor-scale magnetic fluctuations and magnetic trapping. In this work, I have studied some of the effects of the intracluster magnetic fields on thermal conduction and also investigated how the ICM pressure anisotropies might manifest themselves observationally in the form of polarization of thermal bremsstrahlung.

Already in the MHD framework, thermal conduction becomes a non-trivial problem because of the tangled topology of the magnetic-field lines and temporal changes in the field as it evolves in the cluster turbulence. I have found that temperature fluctuations at the scale of turbulent eddies may survive over a dynamically long time despite the large value of the classical Spitzer conductivity in a hot plasma. It happens because the turbulent velocity field statistically tends to orient the frozen-in magnetic-field lines perpendicular to the temperature gradients, effectively suppressing the heat flux in the direction of the gradient, even though the gradients are amplified. I have demonstrated this analytically by applying the Kazantsev-Kraichnan model for the velocity field. Observationally, this process should manifest itself by a correlation between temperature maps obtained from X-ray data and the polarization of synchrotron emission (in regions where it is observed).

Next, I have investigated the effect of the mirror instability on the electron transport in

the ICM. The mirror instability is likely ubiquitous in galaxy clusters, because it is triggered anywhere the magnetic-field lines are stretched by the cluster turbulence. It is a resonant instability capable of generating fluctuations of magnetic-field strength $\delta B/B \sim 1$ at scales of the order of a hundred ion Larmor radii. These fluctuations act as magnetic mirrors for the heat-conducting electrons, suppressing their transport. Interestingly, the suppression effect can be broken down into an effective enhancement of the electron collisionality and a decrease in the number of freely propagating particles, because a fraction of them is trapped by the mirrors. The mirror fluctuations are limited in amplitude by the maximum and minimum values of the field strength, with no large deviations from the mean value, which leads to a finite suppression of thermal conduction at large scales. I have shown that the total suppression factor of thermal conductivity is $\sim 1/5$. This result should also be relevant for any magnetized weakly collisional turbulent plasmas, because it mostly does not depend on the large-scale properties of the plasma.

Finally, I have studied a possibility that electron pressure anisotropies in the ICM leave an observational imprint in the form of thermal bremsstrahlung polarization. These anisotropies are driven by plasma motions via adiabatic invariance and heat fluxes. In the case of coherent plasma flows, the small polarization signal produced by the anisotropic thermal electrons can potentially be observed. The predicted polarization degree is of order 0.1%, which is beyond the sensitivity of the planned X-ray polarimeters. This small polarization does not preclude the use of clusters as (unpolarized) calibration sources for X-ray polarimeters at this level of accuracy. Nevertheless, a future detection (or a non-detection) of this effect at the predicted level might put constraints on the collisionality of the ICM electrons.

For proper physical modelling of the ICM, the magnetic-field effects should be taken into account, e.g., by way of a highly sought-after subgrid model that would encapsulate all the intricacies of plasma kinetics. Currently, such model cannot be constructed because of the lack of understanding of the evolution of microinstabilities in a turbulent plasma. Conversely, increasingly detailed observations of galaxy clusters: of the ICM turbulence and magnetic fields, might improve our understanding of the physics of magnetized weakly collisional plasmas. Without doubt, with the advent of new observatories, clusters of galaxies become increasingly more exciting astrophysical objects, which advance our knowledge about the Universe as a whole, but also give insights into previously unexplored plasma processes.

Acknowledgements

It is a great pleasure to express my gratitude to all the people who immensely contributed to my scientific development.

First of all, I want to thank my supervisor, Dr. Eugene Churazov, who has patiently guided me through the years of my PhD. He has always been ready to answer my questions in a very clear and accessible manner. He would always correct my mistakes gently, even though I was often stubborn to accept them, and in a way that made me learn a lot.

I am indebted to Prof. Rashid Sunyaev, who gave me a remarkable opportunity to be part of the High Energy Astrophysics group at MPA. His generous support has been an essential constituent in completing this work.

I am much obliged to my collaborator, Prof. Alexander Schekochihin, who has an incredible talent to break down complicated concepts in theoretical physics into simple facts. He taught me to pose the right questions and then choose the most convenient ways to answer them. Notably, his influence on my scientific writing has been highly beneficial.

I am thankful to my other collaborators, Prof. Matthew Kunz and Ildar Khabibullin, for sharing scientific ideas, criticism, and many helpful discussions.

No less important for me was the support of my friends in Munich and in Moscow. Without them, at times, it was nearly impossible to get past the troubles and concentrate on doing my work.

I would also like to say thank you to my mother just for believing in me.

Curriculum Vitae

Sergey Komarov

Max Planck Institute for Astrophysics
Karl-Schwarzschild-Str. 1
85741 Garching, Germany

Born: August 2, 1990 in Khabarovsk,
USSR

Citizenship: Russian

E-mail: komarov@mpa-garching.mpg.de

Telephone: +49 89 30000 2245

Education

International Max Planck Research School
PhD student at Max Planck Institute for
Astrophysics

Munich, Germany
2012-2016

Dissertation: Thermal Conduction
in Hot Gas of Galaxy Clusters
Advisors: Dr. Eugene Churazov,
Prof. Dr. Rashid Sunyaev

Moscow Institute of Physics and Technology
Department of Problems of Physics and Energetics
Graduated in Applied Mathematics and Physics
Thesis: Thermal Conduction in Galaxy Clusters
Advisor: Dr. Eugene Churazov

Moscow, Russia
2007-2013

Lyceum of Information Technology
Math profound learning

Khabarovsk, Russia
2004-2007

Lyceum of Mathematics

Khabarovsk, Russia
1997-2004

Attended conferences, workshops and schools

8th Plasma Kinetics Working Group Meeting invited talk	Vienna, Austria 2016
High Energy Astrophysics Today and Tomorrow contributed talk	Moscow, Russia 2014
Cosmic Magnetic Fields contributed talk	Cracow, Poland 2014
Cosmology and Relativistic Astrophysics (Zeldovich-100) poster presentation	Moscow, Russia 2014
7th Plasma Kinetics Working Group Meeting invited talk	Vienna, Austria 2014
High Energy Astrophysics Today and Tomorrow contributed talk	Moscow, Russia 2013
8th Heidelberg Summer School on High Energy Astrophysics	Heidelberg, Germany 2013

Languages: *Russian* native, *English* fluent,
French learning

List of publications

Polarization of thermal bremsstrahlung due to electron pressure anisotropy

S. Komarov, I. Khabibullin, E. Churazov, A. Schekochihin, 2016, MNRAS, 461,
2162

Thermal conduction in a mirror-unstable plasma

S. Komarov, E. Churazov, M. Kunz, A. Schekochihin, 2016, MNRAS, 460, 467

Suppression of local heat flux in a turbulent magnetized intracluster medium

S. Komarov, E. Churazov, A. Schekochihin, J. ZuHone, 2014, MNRAS, 440, 1153